



THE HONG KONG  
POLYTECHNIC UNIVERSITY

香港理工大學

Pao Yue-kong Library

包玉剛圖書館

---

## Copyright Undertaking

This thesis is protected by copyright, with all rights reserved.

**By reading and using the thesis, the reader understands and agrees to the following terms:**

1. The reader will abide by the rules and legal ordinances governing copyright regarding the use of the thesis.
2. The reader will use the thesis for the purpose of research or private study only and not for distribution or further reproduction or any other purpose.
3. The reader agrees to indemnify and hold the University harmless from and against any loss, damage, cost, liability or expenses arising from copyright infringement or unauthorized usage.

### IMPORTANT

If you have reasons to believe that any materials in this thesis are deemed not suitable to be distributed in this form, or a copyright owner having difficulty with the material being included in our database, please contact [lbsys@polyu.edu.hk](mailto:lbsys@polyu.edu.hk) providing details. The Library will look into your claim and consider taking remedial action upon receipt of the written requests.

**PHOTOCATALYTIC NANOFIBERS COMPOSED  
OF OXIDES OF TITANIUM, ZINC, AND BISMUTH  
FOR THE DEGRADATION OF POLLUTANT DYE  
IN WATER, NITRIC OXIDE AND VOC**

**PEI CHUN**

**Ph.D**

**The Hong Kong Polytechnic University**

**2015**

**The Hong Kong Polytechnic University**

**Department of Mechanical Engineering**

**Photocatalytic Nanofibers Composed of Oxides of  
Titanium, Zinc, and Bismuth for the Degradation of  
Pollutant Dye in water, Nitric Oxide and VOC**

**PEI CHUN**

A Thesis Submitted in Partial Fulfillment of the Requirements for the  
Degree of Doctor of Philosophy

July 2014

# CERTIFICATE OF ORIGINALITY

I hereby declare that this thesis is my own work and that, to the best of my knowledge and belief, it reproduces no material previously published or written, nor material that has been accepted for the award of any other degree or diploma, except where due acknowledgement has been made in the text.

\_\_\_\_\_ (Signature)

PEI CHUN \_\_\_\_\_ (Name of Student)

# Abstract

Photocatalysis is a photoreaction of light-producing charge carriers on semiconductor surface with the reactants. Titanium dioxide ( $\text{TiO}_2$ ) is found to be the most efficient photocatalyst under ultraviolet (UV) irradiation and as such it has been most commonly used. However, given  $\text{TiO}_2$  can only be excited by UV which takes up 3-4% of the solar spectrum, considerable efforts have been made to increase the light activity of  $\text{TiO}_2$  by broadening the responsive solar spectrum.

In this study, various novel means have been investigated to improve the physicochemical properties of  $\text{TiO}_2$  to enhance the photocatalytic activity for environmental applications. Specifically, semiconductor heterojunctions of  $\text{TiO}_2$  coupled with other semiconductors to form composite nanostructure and  $\text{TiO}_2$  mixed crystal phases have been investigated. Besides, the composite semiconductors are fabricated into the polycrystalline nanofibers as their photocatalytic performances are far superior when compared to nanoparticles.

Composite photocatalysts have been developed using the synergistic effect of specific semiconductors with the goals of harvesting visible light energy and achieving higher photocatalytic performance by reducing both the band-gap energy and recombination rate of the photo-generated electron/hole pairs. Two cases,  $\text{TiO}_2/\text{ZnO}$  composite nanofibers and  $\text{TiO}_2/\text{ZnO}/\text{Bi}_2\text{O}_3$  (TZB) composite nanofibers, have been investigated to demonstrate the approach and benefits.

Pure  $\text{TiO}_2$  nanofibers and  $\text{TiO}_2/\text{ZnO}$  composite nanofibers are synthesized by electrospinning followed by calcination. The diameter of the nanofibers ranges from

70 to 130 nm for different concentrations of the precursor solutions. The photocatalytic activities of nanofibers are studied systematically by the degradation of Rhodamine B (RhB) under the 420 nm visible-light irradiation and the conversion of nitrogen monoxide (NO) gas under solar irradiation. Photocatalytic activity can be optimized by doping with an appropriate amount of Zn to achieve the highest surface oxygen vacancy.

Compared to pure phase of  $\text{TiO}_2$ , the mixed-phase  $\text{TiO}_2$  materials have unique charge transfer and recombination dynamics, and fast diffusion of charge carriers to the surface, all of which improve the photocatalytic activity. The photocatalytic characteristics are investigated using  $\text{TiO}_2/\text{ZnO}$  nanofibers synthesized by calcinating at different temperatures to modify the anatase-to-rutile ratio, thereby changing the  $\text{TiO}_2$  crystal structure. The trade-off effect between the electron/hole recombination rate and the surface area of the crystals can be balanced by optimizing the anatase-rutile ratio. Indeed, the anatase/rutile ratio (48:52) is optimized at calcination temperature of 650 °C, whereby the  $\text{TiO}_2/\text{ZnO}$  composite nanofibers have the highest photocatalytic efficiency both in the degradation of RhB in liquid and conversion of NO gas.

TZB composite nanofibers are synthesized to further improve the photocatalytic efficiency. The TZB nanofibers exhibit much higher photocatalytic activity for the oxidation of NO under simulated solar irradiation than commercial  $\text{TiO}_2$  nanoparticles and  $\text{TiO}_2/\text{ZnO}$  composite nanofibers. The TZB composite nanofibers have increased absorption in both UV and visible range when compared with  $\text{TiO}_2$  nanoparticles. The enhanced photocatalytic activity of TZB is attributed to the difference in the energy band positions of the semiconductors, resulting in both lower band-gap energy and

recombination rate. Moreover, the photocatalytic performances are more stable for TZB nanofibers than the TiO<sub>2</sub> nanoparticles. In addition, a new kinetic model, taken into account of flow retention and physiochemical kinetics, is used to interpret the kinetic behavior of the photocatalytic reaction. Faster kinetics (i.e. higher throughput in the reactor) and higher conversion of NO are realized by optimizing the bismuth concentration in the composite nanofibers. The degradation pathway of o-xylene by TZB and the intermediate byproducts have also been investigated. This study has demonstrated that modified nanofiber photocatalyst can improve surface oxygen vacancy, reduce band gap, and reduce recombination rate thereby improving the photocatalytic oxidation on both gas contaminants and organic dyes in aqueous phase. Tests on the degradation of dye in aqueous phase, conversion of NO and degradation of o-xylene have proven far superior performance for the composite nanofibers as compared to the TiO<sub>2</sub> nanoparticles benchmark despite their surface-area-to-volume ratio are similar.

# Publications

## Journals

1. Carina Chun Pei, Wallace Woon-Fong Leung. Photocatalytic degradation of Rhodamine B by TiO<sub>2</sub>/ZnO nanofibers under visible-light irradiation. *Separation and Purification Technology*, 114 (2013) 108–116
2. Carina Chun Pei, Wallace Woon-Fong Leung. Enhanced photocatalytic activity of electrospun TiO<sub>2</sub>/ZnO nanofibers with optimal anatase/rutile ratio. *Catalysis Communications*, 37 (2013) 100-104.
3. Carina Chun Pei, Wallace Woon-Fong Leung. Solar photocatalytic oxidation of NO by electrospun TiO<sub>2</sub>/ZnO composite nanofiber mat for enhancing indoor air quality, *Journal of Chemical Technology and Biotechnology*, 89 (2014) 1646-1652.
4. Carina Chun Pei, Wallace Woon-Fong Leung. Photocatalytic oxidation of nitrogen monoxide by TiO<sub>2</sub>/ZnO/Bi<sub>2</sub>O<sub>3</sub> nanofibers: optimization and kinetic modelling, *Applied Catalysis B: Environmental*, [dx.doi.org/10.1016/j.apcatb.2015.03.021](https://doi.org/10.1016/j.apcatb.2015.03.021).

## US Patent Applications

Wallace Woon Fong Leung and Carina Chun Pei, Novel composite nanofibers as photocatalyst, Application No. 6169260, March 24, 2014.

## **Conference**

1. Carina Chun Pei, Wallace Woon-Fong Leung, Lijun Yang and Chi-ho Hung. Photocatalytic degradation of Rhodamine B by TiO<sub>2</sub>/ZnO nanofibers under visible light irradiation. ASME 2011 International Mechanical Engineering Congress and Exposition, November 11-17, 2011, Denver, Colorado, USA
2. Carina Chun Pei, Wallace Woon-Fong Leung. Photocatalytic degradation of Rhodamine B by nanofiber photocatalysts under visible light irradiation. The 32nd Israeli Conference on Mechanical Engineering (ICME 2012), October 17-18, 2012, University of Tel Aviv, Israel
3. Carina Chun Pei, Wallace Woon-Fong Leung. Enhanced photocatalytic activity on the removal of NO by electrospun TiO<sub>2</sub>/ZnO nanofibers with optimal anatase/rutile ratio. The 19th International Conference on Advanced Oxidation Technologies for Treatment of Water, Air and Soil, November 17-21, 2013, San Diego, California, USA
4. Carina Chun Pei, Wallace Woon-Fong Leung. Visible-light induced photocatalytic degradation of Rhodamine B by TiO<sub>2</sub>/ZnO composite nanofibers. The 19th International Conference on Advanced Oxidation Technologies for Treatment of Water, Air and Soil, November 17-21, 2013, San Diego, California, USA
5. Carina Chun Pei, Wallace Woon-Fong Leung. Solar photocatalytic degradation of NO by electronspun TiO<sub>2</sub>/ZnO nanofiber mats for enhancement of indoor air quality, The 19th International Conference on Advanced Oxidation Technologies for Treatment of Water, Air and Soil, November 17-21, 2013, San Diego, California, USA
6. Carina Chun Pei, Wallace Woon-Fong Leung. Solar Photocatalytic Oxidation of

NO By Electrospon TiO<sub>2</sub>/ZnO Composite Nanofiber Mat for Enhancing Indoor Air  
Quality.14 AIChE Annual Meeting, November 16-21,2014, Atlanta, GA, USA

# Acknowledgements

Foremost, I would like to express my sincere gratitude to my supervisor, Prof. Wallace Woon-Fong Leung, for his continuous support and encouragement during my Ph.D. study. His character and moral standard are most respectful that I have learned from and appreciated. His critical instructions and invaluable guidance facilitated my success in my Ph.D. research.

Besides, I would like to thank the technicians in the Mechanical Engineering Laboratory, Water and Wastewater Laboratory, Air Laboratory, and Materials Research Centre, especially Mr. Lam and Mr. Tam for their technical support and assistance during the past few years.

My genuine thanks also go to my optimistic and passionate colleagues, Dr. Lijun Yang, Dr. Jingchuan Wang, Ms. Eva Mak, Mr. Kenneth Lo, Mr. Kent Choy, Ms. Curie Hau, Ms. Lijie Xu and Mr. Mingzhi Guo for their advices, inspirations, and moral encouragements throughout my study especially during difficult time. Our friendship is one of the long-lasting treasures that I have gained during my years at PolyU.

Moreover, I would like to thank my friend Ms. Angel Wong for sharing with me so many sweets, my roommate Ms. Rita Tan for waking me up with the pleasant smell of delicious breakfast in the morning, and my friend Tania Tang for accompanying me through all the ups-and-downs.

Last but not least, I would like to deliver my deepest gratitude to my beloved family. They offer me the opportunity for me to live in my own way and always support me unconditionally no matter what choices I have made.

# Table of Contents

<b>CERTIFICATE OF ORIGINALITY .....</b>	<b>II</b>
<b>Abstract.....</b>	<b>III</b>
<b>Publications .....</b>	<b>VI</b>
<b>Acknowledgements .....</b>	<b>IX</b>
<b>Table of Contents .....</b>	<b>1</b>
<b>List of Figures.....</b>	<b>5</b>
<b>List of Tables .....</b>	<b>13</b>
<b>List of Abbreviations .....</b>	<b>14</b>
<b>Chapter 1 Introduction.....</b>	<b>16</b>
<b>1.1 Background .....</b>	<b>16</b>
<b>1.2 Objectives of study.....</b>	<b>19</b>
<b>1.3 Scope of study.....</b>	<b>20</b>
<b>Chapter 2 Literature Review .....</b>	<b>22</b>
<b>2.1 Metal ion doped titanium dioxide.....</b>	<b>22</b>
<b>2.1.1 Advantages of metal doping .....</b>	<b>22</b>
<b>2.1.2 Drawbacks of metal doping.....</b>	<b>32</b>
<b>2.2 Nonmetal ion doped titanium dioxide.....</b>	<b>33</b>
<b>2.2.1 Carbon doping .....</b>	<b>33</b>
<b>2.2.2 Nitrogen doping .....</b>	<b>34</b>
<b>2.2.3 Co-doping .....</b>	<b>35</b>
<b>2.2.4 Sulfur and fluorine doping .....</b>	<b>37</b>
<b>2.2.5 Drawbacks of nonmetal doping.....</b>	<b>38</b>
<b>2.3 Sensitization of Titanium dioxide with organic compounds/inorganic</b>	

metal complexes .....	38
2.4 Titanium dioxide coupled with other semiconductor .....	41
2.5 Mixed phase Titanium dioxide .....	46
<b>Chapter 3 Methodology .....</b>	<b>49</b>
3.1 Introduction.....	49
3.2 Materials and Reagents .....	49
3.3 Preparation of composite nanofibers .....	51
3.4 Characterization of the prepared composite nanofibers.....	55
3.4.1 Thermal behavior .....	55
3.4.2 Morphology characterizations .....	55
3.4.3 Crystal structure characterization.....	56
3.4.4 BET test.....	56
3.4.5 Spectroscopic Measurement.....	56
3.4.5.1 UV-Visible absorption and reflectance spectra .....	56
3.4.5.2 Photoluminescence spectrum.....	57
3.4.6 X-ray photoelectron spectroscopy.....	58
3.4.7 Electrochemical impedance spectroscopy.....	60
3.5 Photocatalytic performance test .....	61
3.5.1 Photocatalytic test in water.....	61
3.5.2 Photocatalytic test in air.....	63
3.5.2.1 Photocatalytic conversion of NO .....	63
3.5.2.2 Photocatalytic degradation of o-xylene.....	65
<b>Chapter 4 Fabrication and Photocatalytic Activity of TiO<sub>2</sub>/ZnO Nanofibers .....</b>	<b>67</b>
4.1 Overview .....	67
4.2 Characterizations of TiO <sub>2</sub> /ZnO composite nanofibers.....	70

4.2.1 Thermal behavior of precursor nanofibers.....	70
4.2.2 XRD analysis of composite nanofibers.....	71
4.2.3 Morphology and crystal structure of composite nanofibers.....	72
4.2.4DRS test of composite nanofibers.....	79
4.2.5 XPS analysis of composite nanofibers.....	81
4.3 Photocatalytic efficiency.....	85
4.3.1 Photocatalytic test on RhB in water.....	85
4.3.2 Modeling of reaction kinetics of RhB degradation.....	92
4.3.3 Photocatalytic test onNO.....	94
4.4 Summary.....	102
<b>Chapter 5 Enhanced Photocatalytic Activity of Electrospun TiO<sub>2</sub>/ZnO Nanofibers with Optimal Anatase/Rutile Ratio .....</b>	<b>104</b>
5.1 Overview.....	104
5.2 Characterizations.....	106
5.2.1 XRD analysis.....	106
5.2.2 TEM images.....	107
5.2.3 UV-Vis diffuse reflectance spectra.....	109
5.2.4 Photoluminescence spectra.....	112
5.3 The photocatalytic activity of TiO <sub>2</sub> /ZnO nanofibers.....	114
5.3.1 Photocatalytic degradation of RhB in water.....	114
5.3.2 Photocatalytic oxidation of NO.....	115
5.4 Summary.....	119
<b>Chapter 6 Fabrication and Photocatalytic Activity of TiO<sub>2</sub>/ZnO/Bi<sub>2</sub>O<sub>3</sub> Nanofibers: .....</b>	<b>120</b>
6.1 Overview.....	120

<b>6.2 Characterization of TiO<sub>2</sub>/ZnO/Bi<sub>2</sub>O<sub>3</sub> composite nanofibers</b> .....	122
<b>6.2.1 Thermal Behavior of the as-spun fibers</b> .....	122
<b>6.2.2 Morphology of the fibers</b> .....	123
<b>6.2.3 Crystal structure of the nanofibers</b> .....	126
<b>6.2.4 UV-visible absorption and reflectance spectra</b> .....	127
<b>6.2.5 Electrochemical impedance spectra</b> .....	129
<b>6.3 Photocatalytic efficiency on the conversion of nitrogen monoxide</b> .....	131
<b>6.4 Kinetic model</b> .....	133
<b>6.5 Photocatalytic oxidation on the degradation of o-xylene</b> .....	139
<b>6.6 Summary</b> .....	144
<b>Chapter 7 Conclusions and Recommendations for Future Research</b> .....	145
<b>7.1 Conclusions</b> .....	145
<b>7.2 Recommendations for future research</b> .....	148
<b>7.2.1 p-n semiconductors composite nanofibers</b> .....	148
<b>7.2.2 Carbon nanotube (CNT)/ TiO<sub>2</sub> composite nanofibers</b> .....	150
<b>7.2.2.1 Overview</b> .....	150
<b>7.2.2.2 Preliminary results</b> .....	150
<b>Appendix</b> .....	156
<b>References</b> .....	159

# List of Figures

Figure 1.1	Primary steps in the photocatalytic mechanism ( $\text{TiO}_2$ ): (I) formation of electron ( $e^-$ )/hole ( $h^+$ ) pairs by photoexcitation; (II) photoinduced charge recombination; (III) photoinduced charge transportation; (IV) oxidation caused by a valence band hole; (V) reduction caused by a conduction band electron.	17
Figure 2.1	Schematic representation of the mechanism of photocatalytic titanium dioxide particles ( $\text{TiO}_2$ : $h\nu_1$ , Fe- $\text{TiO}_2$ : $h\nu_2$ , N- $\text{TiO}_2$ : $h\nu_3$ , Fe-N- $\text{TiO}_2$ : $h\nu_4$ )	25
Figure 2.2	Schematic illustration of the expected energy bands for N-doped $\text{TiO}_2$ (anatase) together with some photoinduced electronic processes.	34
Figure 2.3	Tentative mechanisms for the degradation of methylene blue on the C-N- $\text{TiO}_2$ nanoparticles. (MB, P, IB, and FB represent the methylene blue, carbonaceous species, intra-band-gap state, and flat-band state, respectively.)	35
Figure 2.4	Comparison of the photocatalytic mechanism: (A) for UV irradiation of $\text{TiO}_2$ with the self-photosensitized pathway and (B) under visible light illumination.	37
Figure 2.5	Schematic energy band diagrams of three types of semiconductor heterojunctions.	40
Figure 2.6	Energy diagram for the heterogeneous anatase/rutile $\text{TiO}_2$ films.	45
Figure 3.1	Schematic setup for a traditional electrospinning setup.	50
Figure 3.2	Schematic setup for nozzle -less electrospinning setup.	52

Figure 3.3	Fabrication procedure for EIS test samples.	59
Figure 3.4	Full UV–Vis spectrum of RhB solution.	60
Figure 3.5	Sketch of the Rayonet™ photochemical reactor.	61
Figure 3.6	Experiment setup of photocatalytical reaction of NO <sub>x</sub> .	62
Figure 3.7	Schematic diagram of the experimental setup.	64
Figure 4.1	TG- DSC curves of the as-spun precursor TiO <sub>2</sub> /ZnAc/PVP nanofibers.	68
Figure 4.2	XRD patterns of TiO <sub>2</sub> nanofibers and TiO <sub>2</sub> /ZnO (6.0 % TIP, 0.30 % ZnAc) composite nanofibers calcined at different temperatures.	70
Figure 4.3	SEM pictures of TiO <sub>2</sub> /ZnAc/PVP composite nanofibers calcined at different temperatures. a) Before calcination, b) 450 °C, c) 500 °C, d) 650 °C	72
Figure 4.4	SEM images of the TiO <sub>2</sub> /ZnO composite nanofibers with different zinc acetate contents in precursor solutions calcined at 500°C. a) 0.15 wt. %, b) 0.30 wt. %, c) 0.45wt. %, d) 0.60 wt. %.	73
Figure 4.5	Mean diameter of fiber is calculated from high resolution SEM picture. The figure below shows the diameter distribution of this SEM picture.	74
Figure 4.6	The specific surface areas (SSA) of nanofibers with different diameters, insert shows the TiO <sub>2</sub> /ZnO nanofibers with different diameters obtained in the presence of different zinc acetate contents in precursor solutions.	75
Figure 4.7	TEM image of TiO <sub>2</sub> /ZnO nanofibers and benchmark TiO <sub>2</sub> nanopartiles.	76

Figure 4.8	HRTEM picture of TiO <sub>2</sub> /ZnO nanofibers	76
Figure 4.9	DRS of TiO <sub>2</sub> /ZnO nanofibers and P25 nanoparticles. Data are plotted as transformed Kubelka-Munk function versus the energy of light. Insert shows the absorption spectra between 200 and 800 nm.	78
Figure 4.10	Schematic diagrams for the principle of synergistic effect between TiO <sub>2</sub> and ZnO.	79
Figure 4.11	XPS spectra of TiO <sub>2</sub> nanofibers and TiO <sub>2</sub> /ZnO nanofibers. Insert shows the Zn spectrum of TiO <sub>2</sub> /ZnO nanofibers. It shows a peak at 1021.8 eV (Zn 2p <sup>3/2</sup> ) indicating the presence of ZnO.	81
Figure 4.12	XPS spectra of O 1s curve fitting results of TiO <sub>2</sub> /ZnO composite nanofibers with zinc acetate content of 0.30 % (6.0 % TIP), insert shows the surface oxygen vacancy (SOV) contents of nanofibers obtained in the presence of different zinc acetate concentrations in the precursor solution.	82
Figure 4.13	Adsorption and photodegradation of RhB (10 <sup>-6</sup> M) with various ZnAc dopant TiO <sub>2</sub> nanofibers in suspension (0.5g L <sup>-1</sup> ).	84
Figure 4.14	Rate constants of the adsorption of RhB of different diameter of fibers.	85
Figure 4.15	Rate constants of photocatalytic degradation of RhB of different zinc acetate contents in the precursor solution with the catalyst loading of 0.5 g L <sup>-1</sup> under light irradiation intensity of 750 lux.	85
Figure 4.16	Rate constants of photocatalytic degradation of RhB of different catalyst loading with 0.30 wt. % zinc acetate in the precursor solution under the light intensity of 450 lux.	87

Figure 4.17	Light intensity effect on the photocatalytic reaction of RhB at a constant catalyst loading of $2 \text{ g L}^{-1}$ with 0.30 wt. % zinc acetate in the precursor solution.	87
Figure 4.18	Benchmark tests among $\text{TiO}_2$ nanoparticles, $\text{TiO}_2$ nanofibers and $\text{TiO}_2/\text{ZnO}$ nanofibers with same catalyst loading of $1 \text{ g/L}$ under the irradiation of 365 nm UV light.	89
Figure 4.19	Comparison of model and experimental data at (a) different light intensities (catalyst loading of $2 \text{ g L}^{-1}$ ) and (b) different catalyst loadings (light intensity of 450 lux). (Note: dot lines were calculated from model and marked data were experimental measurements.)	91
Figure 4.20	Benchmark test of nitrogen oxide removal by three different samples: $\text{TiO}_2$ nanoparticles (Diameter of 100 nm) and $\text{TiO}_2$ nanofibers (Diameter of 100 nm and 70 nm) under UV irradiation.	93
Figure 4.21	Nitrogen oxide removals by nanofibers obtained in the presence of different zinc acetate concentrations in the precursor solution (weight of nanofibers 0.150g, irradiation area $5.08 \times 1.27 \text{ cm}^2$ , and relative humidity 20%).	94
Figure 4.22	Nitrogen oxide removal by nanofiber catalyst with different irradiation area (1 unit of irradiation area is $5.08 \times 1.27 \text{ cm}^2$ ) (weight of nanofibers 0.150g, relative humidity 20%).	96
Figure 4.23	Nitrogen oxide removal by nanofiber catalyst under different humidity conditions ( $25^\circ\text{C}$ , 1 atm, $\rho_{\text{O}_2, \text{max}} = 23.01 \text{ g/m}^3$ ) (weight of nanofibers 0.150g, irradiation area $5.08 \times 1.27 \text{ cm}^2$ ).	97

Figure 4.24	Nitrogen oxide removal by nanofiber catalyst for different residence times (weight of nanofibers 0.150g, irradiation area $5.08 \times 1.27 \text{ cm}^2$ , and relative humidity 20%).	99
Figure 5.1	XRD patterns of $\text{TiO}_2/\text{ZnO}$ composite nanofibers calcined at 550, 650, 750 and 850 °C, respectively.	105
Figure 5.2	TEM images of $\text{TiO}_2/\text{ZnO}$ nanofibers. (a-d) TEM of $\text{TiO}_2/\text{ZnO}$ nanofibers calcined at 550 °C, 650 °C, 750 °C and 850 °C, respectively; (e) HRTEM of $\text{TiO}_2/\text{ZnO}$ nanofibers treated at 550 °C; (f) HRTEM of $\text{TiO}_2/\text{ZnO}$ nanofibers treated at 650 °C.	106
Figure 5.3	The UV-Vis diffuse reflectance spectra of $\text{TiO}_2/\text{ZnO}$ nanofibers and $\text{TiO}_2$ nanofibers. The inset shows the absorption spectra between 200 and 800 nm from the transformed Kubelka-Munk function versus the energy of light. (TN: $\text{TiO}_2$ nanofibers, TZN: $\text{TiO}_2/\text{ZnO}$ nanofibers).	108
Figure 5.4	The room temperature PL spectra of $\text{TiO}_2$ nanofibers and $\text{TiO}_2/\text{ZnO}$ nanofibers under excitation wavelength 260 nm. (TN: $\text{TiO}_2$ nanofibers, TZN: $\text{TiO}_2/\text{ZnO}$ nanofibers) (Peaks around 475 nm are generated by the machine noise.)	110
Figure 5.5	The evolution of the concentration of RhB photocatalytic degraded by $\text{TiO}_2/\text{ZnO}$ nanofibers and P25 nanoparticles under visible light irradiation (420 nm) as a function of time. The insert shows the relationship between the reaction rate constants of photocatalytic degradation of RhB at different calcination temperatures.	112
Figure 5.6	The relative variations of the NO removal against irradiation time	114

in the presence of TiO<sub>2</sub>/ZnO nanofibers calcined at different temperatures together with P25 nanoparticles. Inset shows the relationship between the reaction rate constants of photocatalytic oxidation of NO and the calcination temperatures.

Figure 5.7	Proposed schematic illustration of the photocatalytic mechanism of TiO <sub>2</sub> /ZnO nanofibers.	115
Figure 6.1	TGA-DSC curve of the as spun fibers.	119
Figure 6.2	SEM images of TZB nanofibers after calcination with different bismuth (III) nitrate pentahydrate concentrations in precursor solutions: a. 0.1%; b. 0.2%; c. 0.3%; d. 0.4%.	121
Figure 6.3	a SEM picture of the fibers after calcination; b EDS test result of the location shown in a; c TEM image of the prepared nanofibers; d HRTEM image of the fibers.	122
Figure 6.4	XRD patterns of the calcinated nanofibers and commercial TiO <sub>2</sub> nanoparticles.	123
Figure 6.5	The UV-Vis absorption spectra of TZB and commercial TiO <sub>2</sub> nanoparticles between 200 and 800 nm. The insert shows the UV-Vis diffuse reflectance spectra of from the Kubelka-Munk function versus the energy of light.	125
Figure 6.6	Energy diagram of the composite TZB photocatalyst.	126
Figure 6.7	EIS changes of TZB nanofibers films with different bismuth (III) nitrate pentahydrate concentrations in dark/light conditions.	127
Figure 6.8	The relative variations of the NO removal against irradiation time in the presence of TZB nanofibers prepared with different Bi concentrations together with P25 nanoparticles.	129

Figure 6.9	Box model with physical/chemical process controlling the kinetics.	131
Figure 6.10	Kinetic model for the performance of TZB photocatalysts.	135
Figure 6.11	Plot of NO removal and kinetic time constants with different bismuth (III) nitrate pentahydrate concentrations.	135
Figure 6.12	The relative variations of the o-xylene concentration against irradiation time in the presence of TZB nanofibers. Inset shows the benchmark test between TZB nanofibers and P25 nanoparticles with 10 min illumination.	136
Figure 6.13	The evolution profiles of o-xylene intermediates in the photocatalytic degradation process of TZB nanofibers.	137
Figure 6.14	Proposed photocatalytic degradation pathway of o-xylene in the present system.	140
Figure 7.1	Energy cascade of TZB-P1-P2 photocatalyst.	146
Figure 7.2	The SEM picture of CNT/TiO <sub>2</sub> nanofibers before (a) and after (b) calcination.	148
Figure7.3	The TEM picture of MWCNT (a) and CNT/TiO <sub>2</sub> nanotubes (b).	148
Figure7.4	The NO removal rate against irradiation time in the present of different CNT/TiO <sub>2</sub> nanotubes and P25 TiO <sub>2</sub> nanoparticles under simulated solar-light irradiation with single-pass flow through the reactor.	149
Figure7.5	The SEM picture of CNT/TZB nanofibers before and after calcination (a and b), and the TEM images in different magnifications (c and d).	150
Figure7.6	The NO removal rate against irradiation time in the present of	151

TZB nanofibers, CNT/TZB nanofibers, and P25 TiO<sub>2</sub> nanoparticles under simulated solar-light irradiation with single-pass flow through the reactor.

Figure7.7 The plot of test data and box model data of CNT/TZB nanofibers and TZB nanofibers. 152

## List of Tables

Table 2.1	Selected metal dopants and performance of TiO <sub>2</sub>	26
Table 3.1	Experimental chemicals	48
Table 6.1	Identified degradation products and their main fragments determined by GC-MS	138

# List of Abbreviations

AOP	Advanced oxidation process
BET test	Brunauer,Emmett,Teller's test
CB	Conduction band
DR 23	Direct red 23
DRS	UV-Visible absorption and reflectance spectra
DSC	Differential scanning calorimeter
EDS	Energy dispersive X-ray spectroscopy
EIS	Electrochemical impedance spectroscopy
FB	Flat band
GC/MS	Gas chromatograph and mass selective detector
HAc	Acetic acid
IB	Intra band
MB	Methylene blue
NHE	Normal hydrogen electrode
PL	Photoluminescence
PVP	Polyvinyl pyrrolidone
RhB	Rhodamine B
SEM	Scanning electron microscopy
TEM	Transmission electron microscopy
TGA	Thermo gravimetric analyzer
TIP	Titanium isopropoxide
TZB	TiO <sub>2</sub> /ZnO/Bi <sub>2</sub> O <sub>3</sub>

UV	Ultraviolet
VB	Valence band
VOCs	Volatile organic compounds
XPS	X-ray photoelectron spectroscopy
XRD	X-Ray diffraction

# Chapter 1

## Introduction

### 1.1 Background

Semiconductor nanostructure materials with superior physicochemical and optical properties can be potentially employed in various diverse applications. The semiconductors act as photocatalysts for the light-induced photochemical reactions because of their unique electronic structure characterized by a filled valence band (VB) and a vacant conduction band (CB). Photocatalyst can be used for water splitting and oxidation of harmful molecules in air and aqueous phase. The prerequisite for an efficient photocatalyst is that the redox potential for the evolution of hydrogen and oxygen from water for the former case and for the formation of reactive oxygenated species (hydrogen peroxide, hydroxyl, and superoxide radicals) in the latter case should be located within the band gap of the semiconductor. Given the photocatalytic reaction proceeds in either an air-saturated or water-rich environment, the stability of the chosen photocatalyst under these conditions is also important.

In 1972, Fujishima and Honda (Fujishima and Honda 1972) achieved ultraviolet (UV) light induced water cleavage using a  $\text{TiO}_2$  photoanode in combination with a Pt counter electrode immersed in an aqueous electrolytic solution. Since then,  $\text{TiO}_2$  photocatalysis has attracted significant attention because of its promising applications in environmental remediation as well as solar energy conversion. The basic mechanism of photocatalysis have been established and reported in the literature.

Taking  $\text{TiO}_2$  as an example, the mechanism of the photocatalytic process is shown in

Figure 1.1.

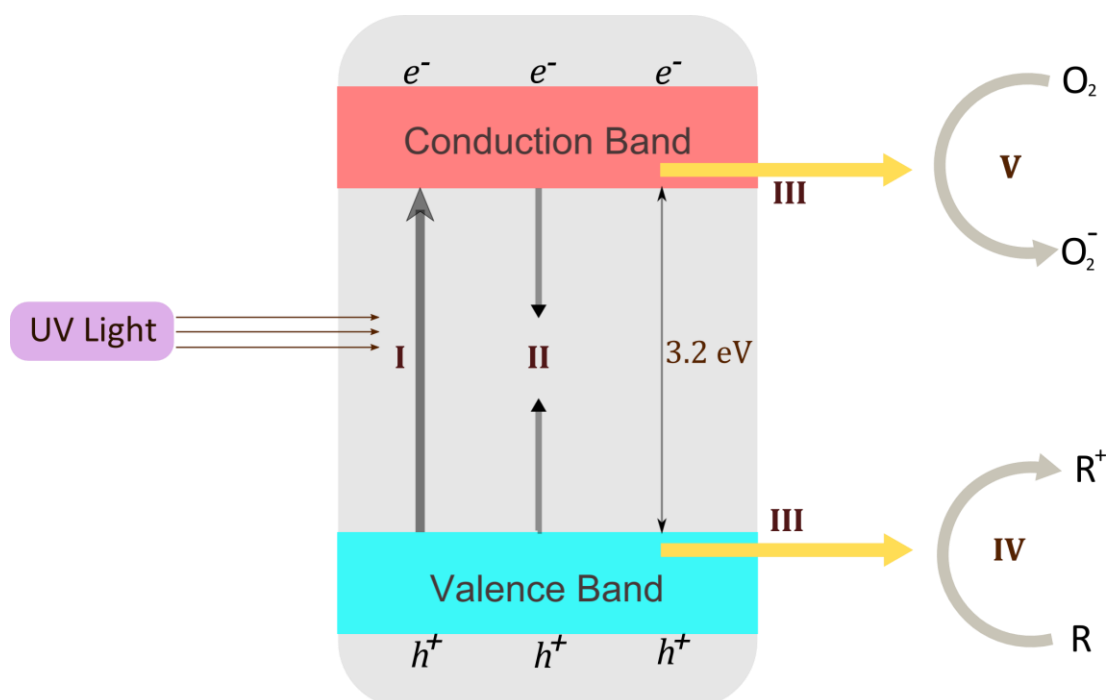


Figure 1.1 Primary steps in the photocatalytic mechanism (TiO<sub>2</sub>): (I) formation of electron (e<sup>-</sup>)/hole (h<sup>+</sup>) pairs by photoexcitation; (II) photoinduced charge recombination; (III) photoinduced charge transportation; (IV) oxidation caused by a valence band hole; (V) reduction caused by a conduction band electron.

When the absorbed photon has an energy equal or exceed the band gap energy ( $E_g$ ) of TiO<sub>2</sub>, an electron in the filled valence band (VB) is excited into the empty conduction band (CB), leaving behind a hole in the VB (stage I). Stage II and stage III occur in parallel, but the recombination process (stage II) is much faster than the transportation process (stage III) as shown in Figure 1.1. In other words, the characteristic time for recombination  $\tau_{rec}$  (say 30 ns) is much faster than the characteristic time for transport  $\tau_{transp}$  (say 250 ns) (Ozawa et al. 2014, Rothenberger et al. 1985). After the electrons and holes are transferred to the active sites on the surface of TiO<sub>2</sub>, they act

respectively as oxidizing and reducing agents to drive oxidation and reduction on the catalyst surface (stage IV and V). In stage IV and V, for photocatalytic degradation of pollutants, holes of the VB can react with surface adsorbed H<sub>2</sub>O to produce hydroxyl radicals. The hydroxyl radicals are strong oxidizing agents, which can oxidize almost all organic pollutants with no selectivity. Moreover, the holes can also directly oxidize the organic pollutants atom forming R<sup>+</sup>.

The excitation of TiO<sub>2</sub> by photons with light energy greater than the band gap is the primary process underlying its vast knowledge domain in photochemistry and photoelectrochemistry. TiO<sub>2</sub> is used mainly due to its advantages: nontoxicity, water insolubility, hydrophilicity, availability (i.e. inexpensive), stability, anti-photocorrosion, and for its suitable flat band potential ( $V_{fb}$ ) that can induce the desired redox reactions without biased potential. Furthermore, TiO<sub>2</sub> can be supported on various substrates such as glass, fibers, stainless steel, inorganic materials, sand, and activated carbon which facilitate its continuous reuse. However, the large band gap of TiO<sub>2</sub> (3.2 eV for anatase and brookite, 3.0 eV for rutile) requires an excitation wavelength that falls in the UV region.

Given that less than about 5% of the solar flux incident at the earth's surface lies in this spectral regime (solar light consists of 5% UV, 43% visible, and 52% harvesting infrared), utilization of natural solar light for a photocatalytic or photoelectrochemical process can thus be enhanced by tuning the band gap response of titanium dioxide to the visible region. Thus, designing, fabricating, and tailoring the physicochemical and optical properties of titanium dioxide to utilize a large fraction of the solar spectrum, or room light for the indoor applications, are indispensable.

A packed bed of nanoparticles have numerous grain boundaries for which separated

electron-hole pairs can be easily recombine at these boundaries. On the other hand, one-dimensional (1D) nanofibers have much reduced boundaries for which separated electron-hole pairs may remain separated and easily transported along the nanofibers and to the surface of the nanofibers to react with the adsorbed molecules on the catalyst surface. The nanofibers surface morphology may contain crystalline and inter-crystalline pores which favor adsorption which is advantageous as this is a prelude to photocatalytic activity.

TiO<sub>2</sub> nanofibers will suffer the same drawback as TiO<sub>2</sub> nanoparticles in that the photo-excitation is confined in the UV range, as such it would be of great interest to explore whether composite nanofibers made from TiO<sub>2</sub> and other appropriate semi-conductor(s) can utilize also the visible solar light spectrum. It is also of interest to investigate the morphology and the various properties of the resulting composite nanofibers.

Finally, the photocatalytic oxidation using both pure TiO<sub>2</sub> and composite nanofibers on degradation and conversion of contaminant gases and organics in solution are investigated.

## **1.2 Objectives of study**

In this study, semiconductor composite nanofibers with high solar light response photocatalytic efficiency are fabricated and characterized, and their potential to degrade and mineralize both gas contaminants and organic dyes in aqueous phase are evaluated.

The specific objectives of this study are as following,

- Fabricate composite nanofibers and study the characteristics of different composite nanofibers.
- Determine the optimal anatase/rutile ratio of the composite nanofibers.
- Investigate the degradation performance (including kinetics) of the composite nanofibers on Rhodamine B (RhB).
- Investigate the photocatalytic oxidation performance of the composite nanofibers on NO including parametric effects and kinetics for air purification.
- Investigate the photocatalytic degradation performance of the composite nanofibers on o-xylene and the degradation pathway for air purification.

### **1.3 Scope of study**

This thesis consists of eight chapters. The present chapter covers the background, objectives and organization of this thesis.

Literature review is presented in Chapter 2 where background information concerning the modification of TiO<sub>2</sub> is described in details.

Chapter 3 provides the detailed description of the experimental techniques and measurement methodology.

Chapter 4 illustrates the fabrication of TiO<sub>2</sub>/ZnO composite nanofibers and the characteristics of the composite nanofibers. The photocatalytic degradation performance of the TiO<sub>2</sub>/ZnO nanofibers on Rhodamine B (RhB) for wastewater treatment is investigated. Kinetic model of the degradation of RhB is also studied.

Chapter 5 presents the performance and optimization of the TiO<sub>2</sub>/ZnO nanofibers in photocatalytic oxidation of NO for air purification. The effects of different parameters oxidation of NO, such as relative humidity, illumination area, and residence time, are deliberated.

Chapter 6 discusses the determination of the optimal anatase/rutile ratio of the TiO<sub>2</sub>/ZnO nanofibers and the evaluation of the photocatalytic performance on the degradation of RhB and NO.

Chapter 7 presents the fabrication and characterization of TiO<sub>2</sub>/ZnO/Bi<sub>2</sub>O<sub>3</sub> composite nanofibers and the photocatalytic degradation on NO and o-xylene. A novel kinetic model of the NO oxidation is proposed and the degradation pathway of o-xylene is also discussed.

In Chapter 8, provides the conclusion of this study, discusses the limitation of this work, and recommends future direction.

# Chapter 2

## Literature Review

In order to have better utilization of solar energy, TiO<sub>2</sub> is modified by various strategies such as coupling with a narrow band gap semiconductor, metal ion/nonmetal ion doping; co-doping with two or more foreign ions; surface sensitization by organic dyes or metal complexes; surface fluorination; and noble metal deposition. The foregoing suggested changes exert a substantial influence in modifying the electronic band structure and construction of favorable surface structure resulting in higher quantum efficiency and reaction rates for the degradation of organic pollutants under UV/solar light illumination. Although the physics behind the separation of space charge carriers varies with different pollutants and also on the surface-electronic structure of the TiO<sub>2</sub>, it is unambiguously accepted that the primary reactions responsible for positive photocatalytic effect are interfacial redox reactions of electrons and holes that are generated from band gap excitation.

### 2.1 Metal ion doped titanium dioxide

#### 2.1.1 Advantages of metal doping

Selective doping of metal ions into the crystalline titanium dioxide matrix has been proven to be an efficient route for improving visible light photocatalytic activity with reduced charge carrier recombination. Doping with a transition metal ion increases the formation of Ti<sup>3+</sup> ions, leading to the enhancement in the photocatalytic activity, as

more  $\text{Ti}^{3+}$  states may cause more oxygen defects which facilitate the efficient adsorption of oxygen on the titanium dioxide surface. The formation of  $\text{O}_2$  upon chemisorptions of oxygen requires the presence of a surface defect site, which can be enhanced by doping using transition metal ion. Since the redox energy states of many transition metal ions lie within the band gap states of  $\text{TiO}_2$ , the substitution of metal ions into the  $\text{TiO}_2$  introduces an intra band state close to the CB or VB edge, inducing visible light absorption at sub-band gap energies. The red shift in the band gap absorption is attributed to the charge transfer transition between the d electrons of the dopant and the CB (or VB) of  $\text{TiO}_2$ .

Titanium dioxide doped with metals such as rare earth metals, noble metals, poor metals, and transition metals have been widely investigated. According to previous research, the metallic ions doped  $\text{TiO}_2$  widen the light absorption range, increase the redox potential of the photogenerated radicals, and enhance the quantum efficiency by inhibiting the recombination of the electrons and holes photogenerated in the conduction and valence bands, respectively. However, the nature and the concentration of dopant, the length of the induced space charge layer, as well as photocorrosion process change the properties at the surface of the materials and consequently influence the photocatalytic activity. This phenomenon has been demonstrated for example by Karakitsou and Verykios (Karakitsou and Verykios 1995). The concentration and the valence of the doping metal ions ( $\text{In}^{3+}$ ,  $\text{Zn}^{2+}$ ,  $\text{W}^{6+}$ ,  $\text{Nb}^{5+}$ ,  $\text{Li}^+$ , etc.) influenced the enhancement or the reduction of the photocatalytic activity. Although there is a large amount of research (Kisch et al. 1998, Wang et al. 1999, Park et al. 2002, Wang et al. 2003a, Wang et al. 2003b, Yu et al. 2009, Singh et al. 2011, Sakai et al. 2013) that demonstrates how metal ion doping of  $\text{TiO}_2$  improves the visible light absorption properties of the material, however, the increase of the

visible light absorption is not a sufficient condition to promote the photoactivity of doped TiO<sub>2</sub> (Štengl et al. 2009, Wang et al. 2014, Zhu et al. 2013, Zhang et al. 2009). Indeed, during the implantation of metal ions, a certain amount of defects can be created and act as recombination centers that decrease the photocatalytic activity. This adverse effect can be avoided by re-annealing the doped TiO<sub>2</sub> (Zhang et al. 2009).

Besides, another feature of TiO<sub>2</sub> doped with metals has been discussed by Dunnill (Dunnill et al. 2012). Doping TiO<sub>2</sub> with metals having either higher or lower oxidation state promotes higher electrical conductivity. For instance, in the case of doping TiO<sub>2</sub> with metallic ions having lower oxidation state (Fe<sup>3+</sup> in low concentration), the electronic neutrality is achieved by removing electrons from the valence band (Wang et al. 2003b, Yu et al. 2009). The hopping of the electrons creates holes in the valence band of the system and increases the electrical conductivity (conduction p-type). By comparison, in the case of doping TiO<sub>2</sub> with metallic ions having higher oxidation rate such as Nb<sup>5+</sup>, electronic neutrality in the system is achieved by injection of the electrons into the empty conduction band (Hu et al. 2014, M Ferroni 2000). These electrons that have injected into the conduction band increase the electrical conductivity (conduction n-type).

Figure 2.1 represents a sketch of the mechanism of photocatalytic doped titanium dioxide. The photocatalytic mechanisms of Fe-N-TiO<sub>2</sub> nanocomposites are initiated by the absorption of the photon  $h\nu_4$  with energy lower than the band gap of TiO<sub>2</sub> (3.2 eV for the anatase phase), and photoinduced electrons and holes can be produced on the surface of TiO<sub>2</sub>. An electron is promoted to the conduction band (CB) while a positive hole is formed in the valence band (VB). Excited-state electrons can reduce the dissolved O<sub>2</sub> to produce the superoxide anion O<sub>2</sub><sup>-</sup>. Meanwhile, the

photo-generated holes in the valence band can further react with water to generate powerful hydroxyl radicals ( $\text{OH}\cdot$ ) and other oxidative radicals. Additional benefit of the dispersion of Fe-N is the improved trapping of electrons via inhibiting electron/hole recombination during irradiation. Decrease of charge carriers recombination results in significantly enhanced photocatalytic activity of  $\text{TiO}_2$  nanoparticles.

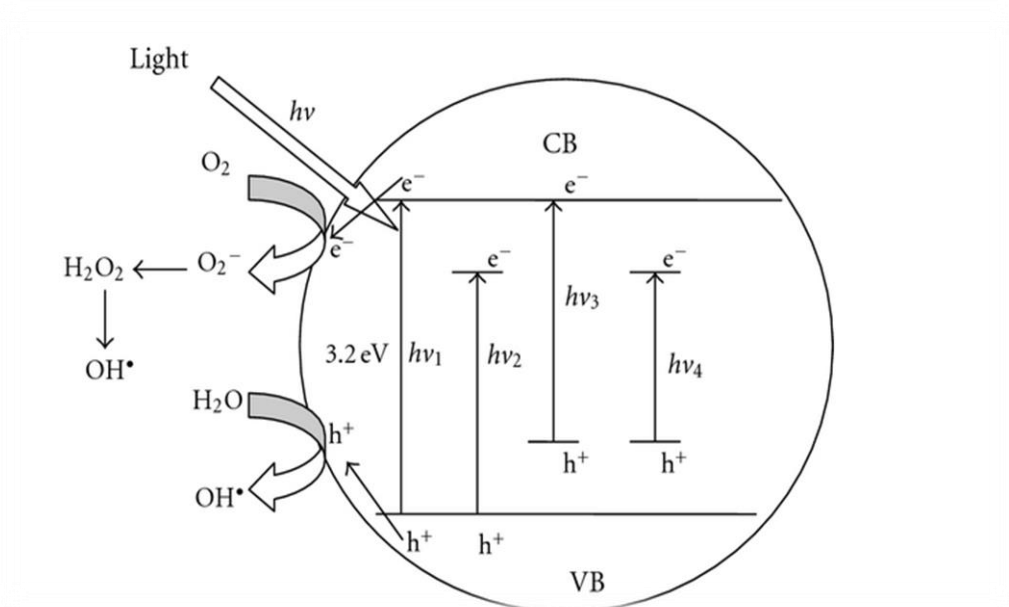


Figure 2.1 Schematic representation of the mechanism of photocatalytic titanium dioxide particles ( $\text{TiO}_2$ :  $h\nu_1$ ,  $\text{Fe-TiO}_2$ :  $h\nu_2$ ,  $\text{N-TiO}_2$ :  $h\nu_3$ ,  $\text{Fe-N-TiO}_2$ :  $h\nu_4$ ) (Huang et al. 2012).

A comprehensive list of metals for doping  $\text{TiO}_2$  and the performance of the doped  $\text{TiO}_2$  is shown in Table 2.1. Noble metal dopants, such as Pt, Pd, Ag, and Au; rare metal dopants, such as Ce, Gd, Nd and Ho; transition metal dopants, such as Fe; post-transition metal dopants, such as Al, Bi, and Sn; have been widely studied. The metal dopants can extend the light absorption of  $\text{TiO}_2$  to the visible range, enhance the separation of photogenerated charge carriers, retard the recombination rate of

electron-hole pairs, as well as increase the specific surface areas, all of which increase the photocatalytic efficiency.

Table 2.1 Selected metal dopants and performance of TiO<sub>2</sub>.

Category of Dopant	Doped Elements	Test Method	Conclusions	References
Noble Metals	Pt, Pd, Ag, Au	Phenol under UV, Visible ( $\lambda > 400$ nm) irradiation	Extend the light absorption of TiO <sub>2</sub> to the visible light range	(Teh and Mohamed 2011)
	Pt	4-chlorophenol under visible irradiation	Increase the separation of photogenerated charge carriers, improve the photocatalytic performances on the surface and bulk modified photocatalyst systems	(Kisch et al. 1998)
	Pt, Au	Photoelectrode properties	The surface of noble metal serves as visible light absorbing sensitizers and centers of charge separation	(Yoon et al. 2005)
	Ag	Phenolic compounds and dyes	Increase of specific surface area, which promotes more reactive sites available to take part in photoreactions.	(Teh and Mohamed 2011)

	Ag	Rhodamine 6G under a Q-Sun solar simulator (visible light) and in Dublin summer sunlight (latitude 54 °N)	Retard the recombination rate of electron-hole pair by enhancing the charge carrier separation	(Seery et al. 2007)
	Ag	Direct red 23 (DR 23) and Direct blue 53 (DB 53) under UV-A light irradiation	Ag nanoparticles deposited on TiO <sub>2</sub> act as electron traps, enhance the electron-hole separation, and ensure the subsequent transfer of the trapped electrons to the adsorbed O <sub>2</sub> acting as an electron acceptor.	(Sobana et al. 2006)
	Pd	Gas Sensor	When the photogenerated electrons migrate to Pd <sup>4+</sup> , electrons and holes are spatially separated, leading to the improvement in photocatalytic activity.	(Moon et al. 2010)

Category of Dopant	Doped Elements	Test Method	Conclusions	References
Rare Earth Metals	Ce	Phenolic compounds and dyes in aqueous solutions	<ol style="list-style-type: none"> <li>Retard the growth of the grain size of TiO<sub>2</sub> thereby decreasing its crystallite size (increase the specific surface area)</li> <li>The redox pair of Ce (Ce<sup>3+</sup>/Ce<sup>4+</sup>) can act as an electron scavenger that traps the bulk electrons into TiO<sub>2</sub> and leads to increase in photocatalytic activity</li> </ol>	(Teh and Mohamed 2011)
	Gd	Direct Blue	Lowest band gap and particle size, and highest surface area and pore volume	(El-Bahy et al. 2009)
	Nd, Ho	Orange II dye in an aq. slurry under irradiation of 254, 365 and 400 nm wavelength	The transition of 4f electrons leads to decrease in the energy band gap by transfer of charge between the TiO <sub>2</sub> valence/conduction band and the 4f level in rare earth ions	(Štengl et al. 2009, Xu et al. 2009, Shi et al. 2009)

Category of Dopant	Doped Elements	Test Method	Conclusions	References
Transition Metals	Fe	Photoelectrochemical behaviors	Fe <sup>3+</sup> doping TiO <sub>2</sub> prevents the agglomeration of the particles and forms well nanocrystalline particles with high surface area, ensuring high photocatalytic efficiency.	(Wang et al. 2014)
	Fe	Acetone, Carbon dioxide	The one-dimensional nanostructure can enhance the transfer and transport of charge carrier. The Fe-doping induces the shift of the absorption edge into the visible-light range narrowing the band gap and reduces the recombination of photo-generated electrons and holes	(Wang et al. 2003a)

Category of Dopant	Doped Elements	Test Method	Conclusions	References
<b>Post-transition Metals</b>	Al	For gas sensor	Retard TiO <sub>2</sub> phase transformation from anatase to rutile by stabilizing the surface state of TiO <sub>2</sub> particles and inhibit grain growth	(Choi et al. 2007)
	Al	Congo Red	The medium UV-Vis absorption peak of mesoporous aluminum-doped TiO <sub>2</sub> in the range 210-370 nm is the absorption peak of aluminum oxide nanoparticles inside the crystalline of TiO <sub>2</sub>	(Liu et al. 2010)
	Bi	Degradation of methylene blue under visible light	Enlarge the wavelength response range and intrinsically narrow the band gap transition of the catalyst	(Ji et al. 2009)
	Sn	Degradation of Rhodamine B dye	Inhibit the phase transformation of TiO <sub>2</sub> from anatase to rutile and decrease the diameter of TiO <sub>2</sub> photocatalyst	(Tu et al. 2009, Sui et al. 2010)

## 2.1.2 Drawbacks of metal doping

As discussed above, doping TiO<sub>2</sub> with metallic dopants has shown positive effects on photocatalysis. However, several authors (Nah et al. 2010, Qiu and Burda 2007) have reported that metal doping TiO<sub>2</sub> have also considerable drawbacks. The photocatalytic activities of a metal doped TiO<sub>2</sub> decrease even under UV irradiation. The metal doped materials have been shown to suffer from thermal instability, and the metals centers act as an electron traps, which encourage the recombination of the photogenerated electrons/holes pairs (Paola et al. 2001). It has been reported that the metallic dopant can serve as carriers recombination centers resulting in decrease in the photocatalytic activity (Lu et al. 2007). For instance, gallium (Ga<sup>3+</sup>), chromium (Cr<sup>3+</sup>), and aluminum (Al<sup>3+</sup>), known as acceptor centers (p-type doping agents), act as a trap for photogenerated electrons and promote the easy recombination with the positive holes. On the contrary, n-type doping agents such as niobium (Nb<sup>5+</sup>), antimony (Sb<sup>5+</sup>), and tantalum (Ta<sup>5+</sup>), known as donor centers, act as traps for photogenerated holes, ensuring the attraction of the electrons and thus promoting the recombination of e<sup>-</sup>/h<sup>+</sup> (Matos et al. 2007). In noble metals, the difference between the Fermi level of noble metals and that of titanium dioxide is ascribed to the electron/hole pair separation. Yet, once the metal centers become negatively charged, holes are attracted to the metal centers especially for highly loaded samples (more than 5%) and the recombination is favored. Current research supports the conclusion that the desired TiO<sub>2</sub> band gap narrowing of TiO<sub>2</sub> can be better achieved using nonmetallic instead of metallic dopants. (Yu et al. 2002, Li et al. 2005a, Umebayashi et al. 2002, Park et al. 2005)

## **2.2 Nonmetal ion doped titanium dioxide**

Various approaches have been made to retard the recombination of the photogenerated electron–hole pairs. Doping TiO<sub>2</sub> with nonmetals such as carbon (C) (Park et al. 2005, Huang et al. 2008, Chen and Burda 2008, Chen et al. 2007), nitrogen (N) (Chen and Burda 2008, Chen et al. 2007, Cong et al. 2007, Sathish et al. 2005, Nakamura et al. 2004), sulfur (S) (Umebayashi et al. 2002, Chen and Burda 2008), and iodine (I) (Long et al. 2006, Tojo et al. 2008) have been a popular approach. Compared to metal dopant, non-metal dopant as recombination centers is minimized. Nonmetal dopants have the ability to improve the morphology and the photocatalytic performance of TiO<sub>2</sub>, further nonmetal dopants can lower the band gap of TiO<sub>2</sub> and shift its optical response to the visible light spectrum (huo et al. 2009, Livraghi et al. 2009). Over the last several years, it has been demonstrated by many researchers that TiO<sub>2</sub> doped with nonmetal elements (carbon, sulfur, fluorine, nitrogen, etc.) show favorable performance in the visible region and higher photocatalytic activity. The impurity states are close to the valence band edge but they do not play the role as charge carriers (Park et al. 2005, Cong et al. 2007, Huang et al. 2006, Xie and Zhao 2008, Li et al. 2005b, Huang et al. 2009). Among all the nonmetals, doping TiO<sub>2</sub> with carbon or nitrogen has been found to have higher photocatalytic activity under visible light irradiation (Huang et al. 2008, Chen and Burda 2008).

### **2.2.1 Carbon doping**

Significant effort has been directed toward carbon doping of TiO<sub>2</sub>. The substitution of

carbon atoms in the TiO<sub>2</sub> photocatalyst introduces new states (C 2p) close to the valence band edge of TiO<sub>2</sub> (O 2p). Accordingly, the conduction band edge shifts downward narrowing the band gap. The incorporation of carbon into TiO<sub>2</sub> may form carbonaceous species at the surface of the photocatalyst, which are reported to facilitate absorption of the visible light. Furthermore, the high surface area of the doped sample is another factor that increases the photocatalytic activity of the C-doped TiO<sub>2</sub>. The higher surface area provides more reactive sites and promotes the adsorption of more target pollutants. It is also reported that C-doped TiO<sub>2</sub> appears to be much efficient to degrade trichloroacetic acid under visible light irradiation than pure TiO<sub>2</sub> (Yang et al. 2009, Wong et al. 2008). The electron excited from these surface states (C-doped TiO<sub>2</sub>) can form sufficient O<sub>2</sub><sup>•-</sup> and OH<sup>•</sup> radicals under visible irradiation resulting in higher degradation and mineralization of pollutants.

### **2.2.2 Nitrogen doping**

Doping TiO<sub>2</sub> with nonmetals, such as nitrogen, has received equal attention (Chen et al. 2007, Cong et al. 2007, Sathish et al. 2005, Nakamura et al. 2004). The photocatalytic properties of N-doped TiO<sub>2</sub> under visible light are extremely favorable for environmental applications, for which the conventional TiO<sub>2</sub> is not used (Nakamura et al. 2004). Doping nitrogen into titanium dioxide changes the refraction index, hardness, electrical conductivity, elastic modulus, and the photocatalytic activity toward visible light absorption. The nitrogen species resulting from the TiO<sub>2</sub> doping can be either a substitutional or an interstitial N atom in the TiO<sub>2</sub> matrix. The substitutional species are mostly localized above the valence band, whereas the interstitial form is present at 0.73 eV above the valence band (Asahi and Morikawa 2007). Thus, to maintain the electronic neutrality and to form an oxygen vacancy,

three oxygen atoms should be replaced by two nitrogen atoms. The schematic illustration of the expected energy bands for N-doped TiO<sub>2</sub> (anatase) together with some photoinduced electronic processes is shown in Figure 2.2.

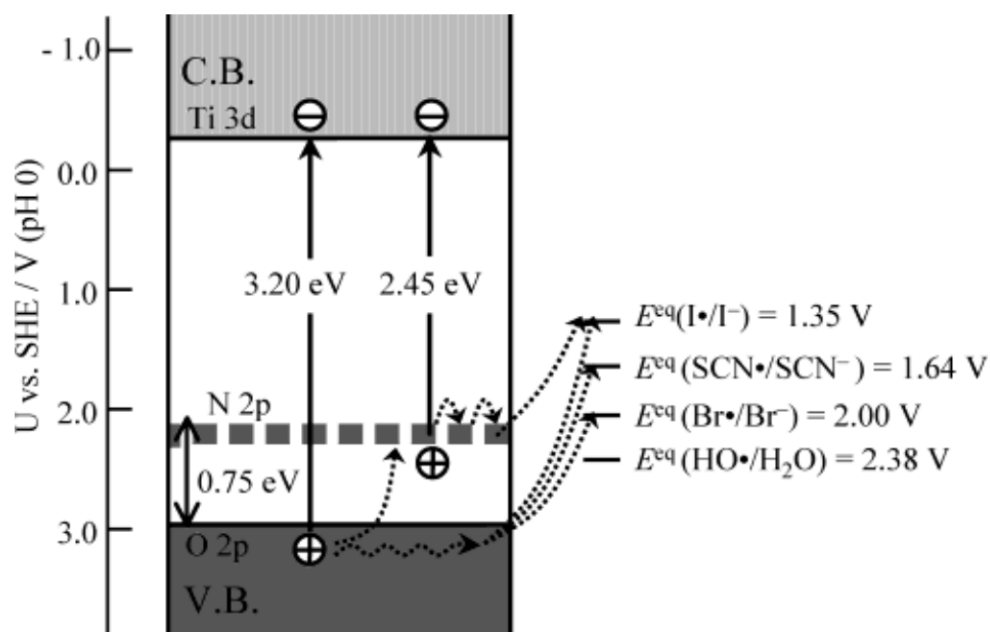


Figure 2.2 Schematic illustration of the expected energy bands for N-doped TiO<sub>2</sub> (anatase) together with some photoinduced electronic processes. (Cong et al. 2007)

### 2.2.3 Co-doping

Furthermore, it has been also observed that the techniques or the preparation methods employed for co-doping two or more nonmetal elements into TiO<sub>2</sub> (Chen et al. 2007, Li et al. 2005b). As illustrated in Figure 2.3(Chen et al. 2007), there are several possible mechanisms for the photocatalytic activity enhancement of C-N-TiO<sub>2</sub> materials. One of these possible mechanisms is that the reactive electrons (e<sup>-</sup>) from the conduction band reduce O<sub>2</sub> to its radical anion, which can further transform to H<sub>2</sub>O<sub>2</sub>

and  $\text{OH}\cdot$ , resulting ultimately in the oxidation of methylene blue (MB) at last. Another possible mechanism is that the reactive holes ( $\text{h}^+$ ) oxidize MB to its radical cation either directly, or through  $\text{OH}\cdot$  radical produced by the oxidation of ubiquitous water. In the first process of interfacial electron transfer, the carbonaceous species (P) formed by doped C atoms play the role of photosensitizer similar to organic dyes, which can be excited injecting electrons into the conduction band of  $\text{TiO}_2$ ; this increases the rate of electron transfer to oxygen absorbed on the  $\text{TiO}_2$  surface increases. On the other hand, the N atoms doped in  $\text{TiO}_2$  can also promote this electron transfer. It is reported that nitrogen doping not only can create intra-band-gap states (IB) close to the valence band edges, which induces visible light absorption at the sub-band-gap energies  $h\nu_2$ , but also shift the position of flat-band (FB) potential (dashed line shown in Figure 2.3) to a higher level than that of the un-doped  $\text{TiO}_2$ . This concurrently increases the driving force of electron injected from carbonaceous species and accelerates the reductive process of interfacial electron transfer.

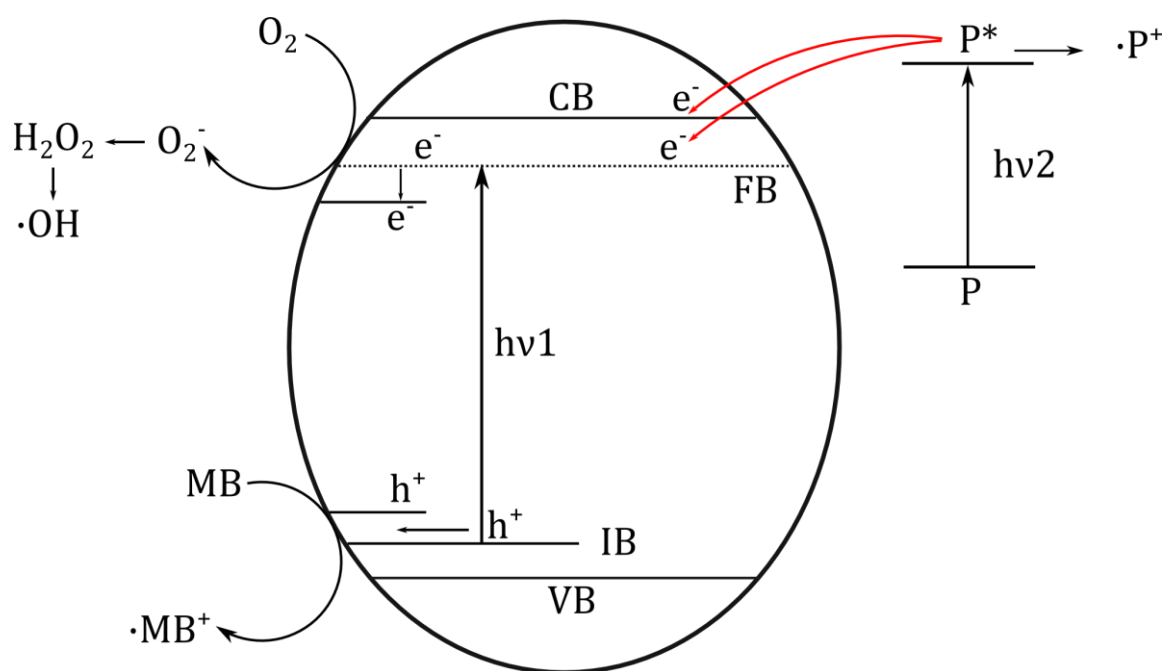


Figure 2.3 Tentative mechanisms for the degradation of methylene blue on the

C-N-TiO<sub>2</sub> nanoparticles. (MB, P, IB, and FB represent the methylene blue, carbonaceous species, intra-band-gap state, and flat-band state, respectively) (Chen et al. 2007).

#### **2.2.4 Sulfur and fluorine doping**

In addition to nitrogen and carbon doping, sulfur and fluorine have been successfully used for TiO<sub>2</sub> doping (Yu et al. 2002, Nanayakkara et al. 2012, Wu et al. 2011). Fluorine atoms (1.33 Å for F<sup>-</sup>) can easily substitute for O atoms (1.4 Å for O<sup>2-</sup>) owing to their similar ionic radii. Fluoride ions have been detected not only at substitutional sites in the lattice but also physically adsorbed on the surface of doped TiO<sub>2</sub> nanoparticles (Yu et al. 2002, Xie and Zhao 2008).

By comparison, sulfur can be used as anion for doping TiO<sub>2</sub> by substituting O sites and also as cation by replacing Ti<sup>4+</sup> in the bulk or at the surface (Umebayashi et al. 2002, Chen and Burda 2008). The substitutional doping of S into the TiO<sub>2</sub> distorts the crystal lattice because the ionic radius of S (1.8 Å) is so much greater compared to that of O (1.4 Å). The incorporation of an S3p band above the valence band edge shifts the band gap and ensures higher photocatalytic efficiency. Furthermore, S-doped TiO<sub>2</sub> has been formed to extend the photocatalytic activity to the visible region and to ensure excellent photocatalytic degradation of organic pollutant under visible irradiation. For example, higher degradation of trichloroethylene (80%) and methyl-tertiary butyl ether (75%) have been reported when S-doped TiO<sub>2</sub> (weight of S = 2.6 mg cm<sup>-2</sup>) has been used under daylight irradiation (1.8 mW cm<sup>-2</sup>) (Hamadianian et al. 2009). By incorporating sulfur into TiO<sub>2</sub>, the ratio of anatase and rutile can be modified to improve the photocatalyst efficiency of doped TiO<sub>2</sub> under visible

irradiation.

### **2.2.5 Drawbacks of nonmetal doping**

Despite the several advantages achieved by doping TiO<sub>2</sub> with nonmetals, the content of dopant decreases during the annealing process, thus reducing the photoactivity under visible irradiation (Park et al. 2002, Teh and Mohamed 2011, Linsebigler et al. 1995). This major drawback limits the incorporation of nonmetallic elements for doping TiO<sub>2</sub>. Other research focuses on the coupling of two semiconductors as a means to compensate the drawbacks of doped TiO<sub>2</sub>. This approach will be discussed in a later section.

## **2.3 Sensitization of Titanium dioxide with organic compounds/inorganic metal complexes**

The mechanism of photoassisted degradation of organic dyes in aqueous TiO<sub>2</sub> dispersions under visible light irradiation (Figure 2.4B) is different from the pathway implicated under UV light illumination (Figure 2.4A). Despite the fate of the injected electron under visible irradiation is no different from that of CB electrons photogenerated under UV illumination. For UV irradiation of TiO<sub>2</sub>, holes are also generated which can produce hydroxyl and other radicals (see Figure 2.4A).

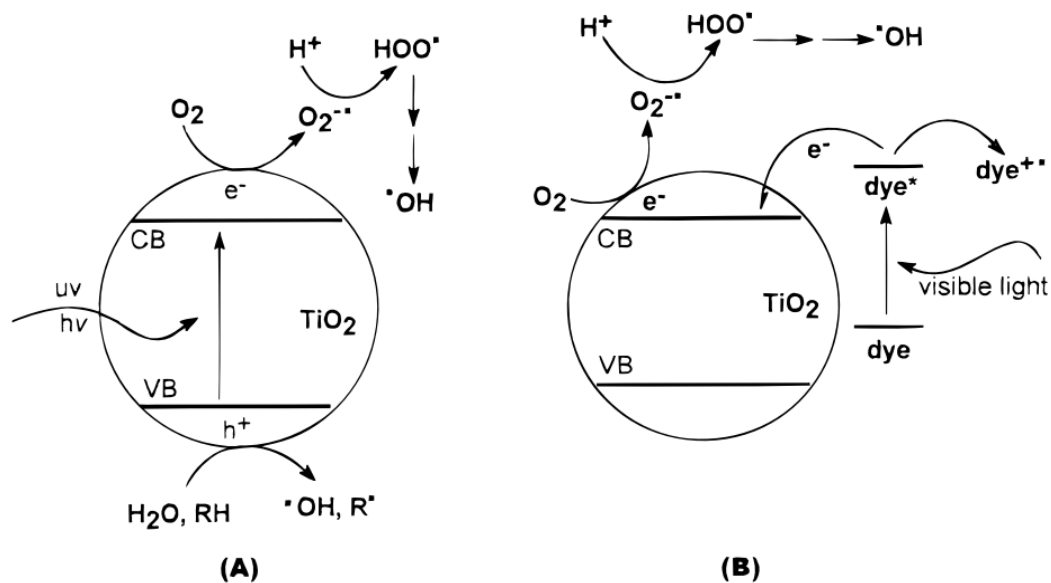
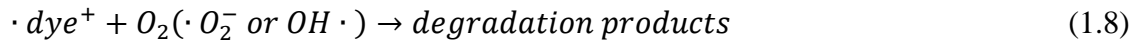


Figure 2.4 Comparison of the photocatalytic mechanism: (A) for UV irradiation of  $\text{TiO}_2$  with the self-photosensitized pathway and (B) under visible light illumination (Wu et al. 1998).

The dye sensitization process (Figure 2.4B) is usually referred to as indirect electron injection, which involves multi exponential kinetics with fast components of tens of femtoseconds (from the singlet excited state of the dye to the  $\text{TiO}_2$  CB) and slow components of several picoseconds (from the triplet excited state of the dye to the  $\text{TiO}_2$  CB). In the sensitization process, dye gets excited rather than the  $\text{TiO}_2$  particles to appropriate singlet and triplet states, and the dyes are subsequently converted to cationic dye radical with concurrent release of electron. The electrons are subsequently injected to the  $\text{TiO}_2$  CB and react with the pre-adsorbed  $\text{O}_2$  to form oxidizing species (superoxide, hydroperoxyl, and hydroxyl radicals) resulting in photooxidation reactions (Figure 2.4). Thus,  $\text{TiO}_2$  plays an important role in electron-transfer mediation, even though  $\text{TiO}_2$  itself is not excited. The photodegradation mechanism of dyes under visible irradiation is proposed as follows:



Another mechanism of sensitizing TiO<sub>2</sub> by visible light is the direct charge transfer between surface adsorbate and TiO<sub>2</sub> (Park et al. 2013). In the charge transfer sensitization, the electron is photoexcited directly from the ground state adsorbate to the conduction band of TiO<sub>2</sub>. The formation of the charge transfer complex on the surface of TiO<sub>2</sub> usually accompanies the appearance of a visible light absorption band, which is not seen in either adsorbate or TiO<sub>2</sub> alone. Surface adsorbate such as aromatic compounds having hydroxyl or carboxyl anchoring group are the common examples of formation of charge transfer complex on TiO<sub>2</sub> surface. The TiO<sub>2</sub>-catechol complex is a classical example of charge transfer complex (Park et al. 2013). According to Wang et al. (Wang et al. 2003c) the formation of a complex between catechol and TiO<sub>2</sub> creates a broad new band centered at 390 nm, which is extended into the visible region at 600 nm. The excitation of visible light induces the direct transfer of electron from the organic substrates into the conduction band of TiO<sub>2</sub>. The

application of such mechanism can be a promising alternative for the development of visible light active photocatalysts.

## 2.4 Titanium dioxide coupled with other semiconductor

To overcome the thermal instability and the high recombination rate arising from the metal and nonmetal doping, the fabrication, design, and tailoring of the semiconductor heterojunction, instead of introducing ions into the lattice of  $\text{TiO}_2$ , for achieving better charge separation in a photo energy conversion system has received significant research interest. The vectorial charge transfer from one semiconductor to another with suitable band edge positions that is thermodynamically favorable can increase the lifetime of the charge carriers thus promoting the interfacial charge transfer and catalytic efficiency. Among these approaches, formation of semiconductor heterostructures is an effective way to enhance the photoinduced charges separation efficiency and the photocatalytic performance, and has been extensively studied for the last decades. Depending on the band gaps and the electronic affinity of semiconductors, semiconductor heterostructures can be divided into three different cases: type-I, type-II and type-III band alignment as shown in Figure 2.5.

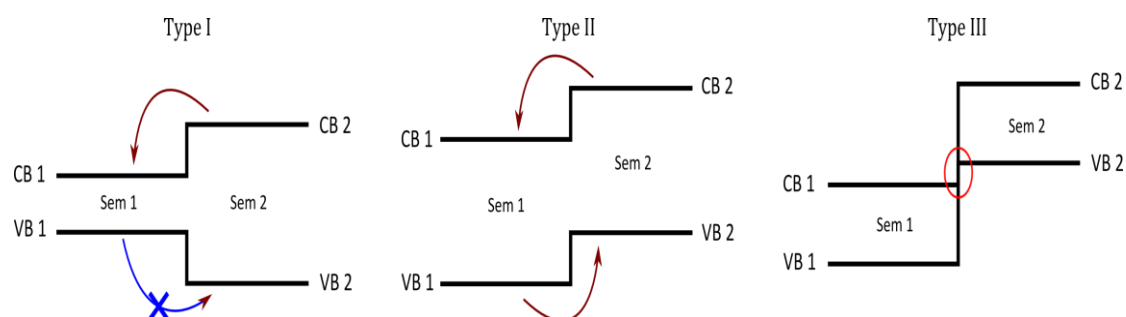


Figure 2.5 Schematic energy band diagrams of three types of semiconductor heterojunctions.

In type I, the semiconductor 2 has a higher conduction band and a lower valance band, electrons can transfer from the conduction band (CB) of semiconductor 2 to semiconductor 1; while the holes cannot move from the valance band (VB) of semiconductor 1 to semiconductor 2, instead, holes accumulate in VB1 and VB2 separately, thereby the charge transfer is discontinuous in type I. In type III, the semiconductor 2 has an even higher valance band than the conduction and of semiconductor 1. Electrons and holes recombine easily in type III system. On the other hand, in a type II band alignment, the positions of both valance and conduction bands of semiconductor 2 are higher than those of semiconductor 1, and the steps in the conduction and valance bands go in the same direction.

Importantly, the difference of chemical potential between semiconductor 1 and 2 causes band bending at the interface of junction. The band bending induces a built-in field, which drives the photogenerated electrons and holes to move in opposite directions, leading to a spatial separation of the electrons and holes on different sides of heterojunction. Thus, the formation of type II heterostructures is an effective approach to enhance charge separation efficiency for improved photocatalytic degradation activity and water splitting efficiency.

The coupled system of the type ZnO/TiO<sub>2</sub> showed lower activity for the degradation of amaranth and procion red MX-5B compared to ZnO (Wu 2004). This insignificant inter particle electron transfer effect can be due to: (i) close proximity of the CB edge of both TiO<sub>2</sub> and ZnO; (ii) both ZnO and TiO<sub>2</sub> are being photoactivated by UV illumination resulting in perfunctory separation of charge carriers. In contrast, coupling of ZnO (0.5 atom% of Zn<sup>2+</sup>) with Degussa P-25 (bicrystal of anatase and rutile) by a wet impregnation method showed enhanced activity for the oxidation of

NO<sub>x</sub> under UV light due to the dense hydroxyl groups on the catalyst surface and efficient interfacial charge transfer in the tricomponent ZnO-anatase-rutile system. The VB edge of ZnO lies above the anatase TiO<sub>2</sub> VB, and the CB edge of rutile TiO<sub>2</sub> lies below the anatase TiO<sub>2</sub> CB. Under UV light excitation, vectorial hole transfer takes place from the VB of anatase TiO<sub>2</sub> to ZnO (VB), while electron transfer takes place from the CB of anatase TiO<sub>2</sub> to the rutile TiO<sub>2</sub> CB. However, a high dosage of ZnO (0.5 atom %) is not beneficial to photocatalytic activity because the abundant ZnO particles on the TiO<sub>2</sub> surface act as recombination centers (Wang et al. 2008).

TiO<sub>2</sub>/WO<sub>3</sub> is another semiconductor-semiconductor coupled system, which has been widely used as a photocatalyst (Papp et al. 1994, C. Mart ín 1997, Chai et al. 2006). The band gap of WO<sub>3</sub> is lower (2.8 eV), and both the upper edge of the valence band and the lower edge of the conduction band of WO<sub>3</sub> are lower than those of TiO<sub>2</sub>. Thus, WO<sub>3</sub> can be excited by visible light, and the photogenerated holes can be transferred from WO<sub>3</sub> to TiO<sub>2</sub> (Chai et al. 2006). The electron in the conduction band of TiO<sub>2</sub> could be easily accepted by WO<sub>3</sub> because the standard reduction potential between W(VI) and W(V) is only -0.03 V (He et al. 2003, Smith and Zhao 2008). The electrons in WO<sub>3</sub> would then be transferred to the oxygen molecules adsorbed on the surface of TiO<sub>2</sub>. The increase of the photocatalytic activity of TiO<sub>2</sub> was confirmed by several research groups as a result of coupling with WO<sub>3</sub> for the decomposition of benzene, methylene blue, butyl acetate, and dichlorobenzene. Higher rates of pollutant degradation were recorded owing to the increase of electron transfer from TiO<sub>2</sub> to WO<sub>3</sub> via the formation of an intermediate W(V) species, together with the increased surface acidity in the TiO<sub>2</sub>/WO<sub>3</sub> couple. It has been reported by Papp (Papp et al. 1994) that the surface acidity and the protonated surface hydroxyl groups promote the transfer of electron from the conduction band of TiO<sub>2</sub> to the adsorbed oxygen

molecules and hence increase the photocatalytic activity. However, the TiO<sub>2</sub>/WO<sub>3</sub> coupling does not always enhance the photocatalytic activity of TiO<sub>2</sub> (Tada et al. 2004). Too much loading of WO<sub>3</sub> could act as a center of charge recombination. Furthermore, the preparation technique of coupled semiconductor TiO<sub>2</sub>/WO<sub>3</sub> remains a critical parameter (He et al. 2003, Pan and Lee 2006, Song et al. 2001) that influences the band structure properties and, consequently, the photocatalytic activity.

Coupling TiO<sub>2</sub> with cadmium sulfide (CdS) is highly promising approach in the field of research (Baker and Kamat 2009, Evans et al. 1994, Jang et al. 2007, Gao et al. 2009). Cadmium sulfide, with a narrow band gap of 2.4 eV, is one of the well-known semiconductors. Both the conduction band and the valence band of CdS are higher than their counterparts in TiO<sub>2</sub>. The conduction band potentials of TiO<sub>2</sub> and CdS versus Normal Hydrogen Electrode (NHE) at pH 7 are -0.5 and 0.95 V, respectively. Such appropriate alternation in the energy levels of the valence and conduction bands allows CdS to act as photosensitizer to absorb visible irradiation and to generate electrons and holes (Lee et al. 2008). Subsequently, the electrons are injected into the conduction band of the inactivated TiO<sub>2</sub> leaving the holes behind in the valence band of CdS. The TiO<sub>2</sub> accepts photoelectrons generated from the CdS, which could effectively inhibits the recombination of photoelectrons and holes in CdS. Owing to this charge separation under visible light illumination, the couple TiO<sub>2</sub>/CdS has been widely applied to enhance the degradation of organic pollutants (Jang et al. 2007, Daskalaki et al. 2010, Yin et al. 2001) by photocatalytic and photoelectrocatalytic reactions.

A small amount of CdS dispersed in the TiO<sub>2</sub> matrix can absorb visible light making the photocatalyst TiO<sub>2</sub>/CdS sensitive to visible light. Bassekhouad (Bessekhouad et al.

2006) prepared TiO<sub>2</sub>/CdS by a sol–gel method with a CdS loading varied from 5 to 50%. Higher photocatalytic activity of TiO<sub>2</sub>/CdS containing low proportion of CdS (from 5 to 10%) has been recorded toward the degradation of Acid Orange II (removal more than 50% of Acid Orange II) under visible (less than 20% of Acid Orange II degradation) light irradiation ( $\lambda > 400$  nm) compared to pure TiO<sub>2</sub> or CdS. This higher activity is mainly due to the electron transfer from CdS to TiO<sub>2</sub>, which prevents the recombination of charge carriers. The same trend has been also reported by Tristao (Tristao et al. 2006) while studying the photodegradation of organic dye Drimaren red using the same catalyst. The photocatalytic efficiency of the couple TiO<sub>2</sub>/CdS is highly dependent on the proportion of CdS. For instance, higher degradation of organic dye Drimaren red (more than 95%) has been recorded when the TiO<sub>2</sub>/CdS system containing lower amounts of CdS (only 5%). In water, organic compounds are adsorbed on the CdS surface than the TiO<sub>2</sub>, and the suitable level suggests that the transfer of the electrons from the dye to CdS contributes to the degradation mechanism (Daskalaki et al. 2010, Zhu et al. 2008, Jang et al. 2008).

However, it is well-known that the photocatalytic activity is closely related to the surface area. Thus, catalyst made into nano-scale with large specific surface is widely used. It has been reported (Bessekhouad et al. 2005) while studying the photocatalytic activity of Cu<sub>2</sub>O/TiO<sub>2</sub>, that the physical chemical properties and the structure of the photocatalyst influence the performance of the process. Some other oxides, such as ZnO (Lotus et al. 2011), Bi<sub>2</sub>O<sub>3</sub> (Balachandran and Swaminathan 2012), SnO<sub>2</sub> (Liu et al. 2006), among others, have been used in previous research for enhancing the photoactivity of titanium dioxide. Yet, the application of these different photocatalysts in coupling with TiO<sub>2</sub> remains limited in the photocatalytic treatment of water due to the durability aspect.

## 2.5 Mixed phase Titanium dioxide

Contradicting results are reported about the influence of phase composition on the photocatalytic degradation of organic pollutants in both air and water. Indeed, several findings reported that anatase works better than rutile (Arnal et al. 1996, Li et al. 2007, Koelsch et al. 2004), while other findings reported the best results for rutile (Darwin Castillo 2014). Much experimental evidence supports the existence of a synergistic effect in the bicrystalline titanium dioxide containing anatase-rutile (Liu et al. 2007, Bakardjieva et al. 2005, Gerloff et al. 2012, Pei and Leung 2013a), anatase-brookite (Kandiel et al. 2013, Hu et al. 2003, Ozawa et al. 2005, Ardizzone et al. 2007), rutile-brookite (Kim et al. 1996, Cassaignon et al. 2007), or tricrystalline anatase-rutile-brookite (Li et al. 2007, Matsui and Akaogi 1991, Ranade et al. 2002) in enhancing the photocatalytic activity.

Figure 2.6 shows a schematic illustration of the energy diagram for the heterogeneous anatase/rutile  $\text{TiO}_2$  system. It has been reported that the band gaps of anatase and rutile  $\text{TiO}_2$  are 3.2 and 3.0 eV, respectively; also, the conduction band potentials of anatase and rutile  $\text{TiO}_2$  are about -4.21 V and -4.31 V (versus vacuum at pH 7), respectively. Therefore, the conduction band of rutile is considered to be lower level than that of anatase. As shown in Figure 2.6, the coupling of two phases allows the vectorial displacement of electrons from the anatase phase to the rutile phase and retards the recombination of the electron-hole pairs in anatase (Cassaignon et al. 2007, Ranade et al. 2002). Upon UV excitation, photo-generated electrons accumulate in the lower-lying conduction band of rutile; whereas holes can accumulate in the valence bands of both anatase and rutile, since the holes cannot transfer from rutile to anatase (the valence potential of rutile is higher than that of anatase). Accumulated electrons

in the conduction band of rutile can be transferred to oxygen adsorbed on the surface to form  $O_2^-$ . Accumulation of holes in the valence band of anatase and rutile leads to the production of surface hydroxyl radicals, which are responsible for the oxidation decomposition of acetone. As for the heterogeneous anatase/rutile  $TiO_2$  system, photo-generated electrons are effectively accumulated in the rutile phase, without recombining with the holes in the anatase valence band, which leads to the enhancement of the photocatalytic activity of anatase.

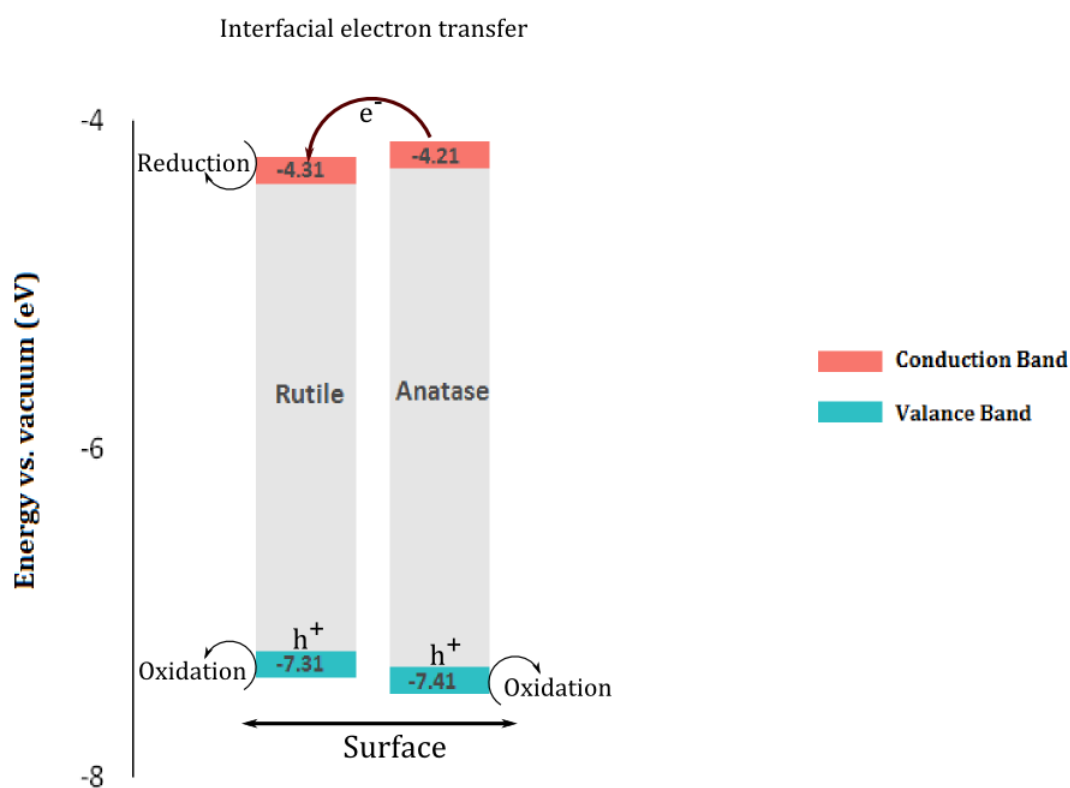


Figure 2.6 Energy diagram for the heterogeneous anatase/rutile  $TiO_2$  films.

Overall, what is missing in the literature is the use of ZnO, anatase and rutile in 1-D nanofiber for use in photocatalytic oxidation as the 1-D nanofibers may further favor electron transport along the nanofiber. Another missing information is how the ratio

of anatase-rutile can affect performance of the photocatalyst. The ratio of these two crystals in  $\text{TiO}_2$  can be readily adjusted through changing the calcination temperatures. Also in configuration, the size and morphology of the crystals that makes up the nanofibers are important factors affecting photocatalytic process that has yet been investigated.

This study focuses on the semiconductor composites together with the mixed phases  $\text{TiO}_2$  with relatively low band gap energy level, high charge separation efficiency and low electron/hole recombination rate to achieve high photocatalytic efficiency. Furthermore, the composite semiconductors are made into 1-D nanofibers to facilitate the contact probability between the photocatalyst and target pollutant and also to increase the durability of the catalyst for use in environmental applications.

## **Chapter 3**

# Methodology

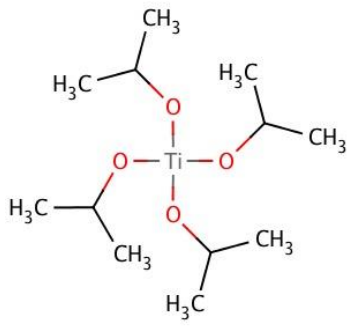
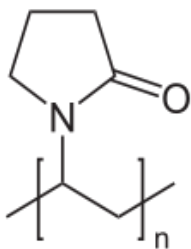
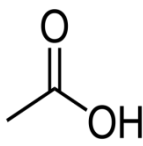
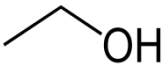
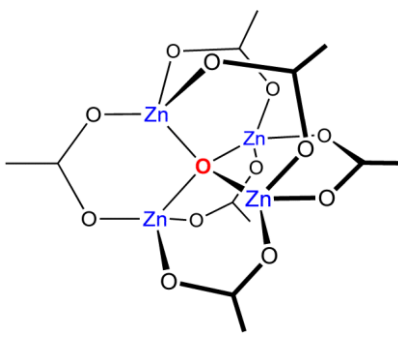
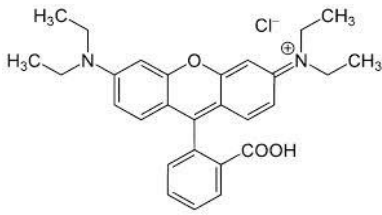
## 3.1 Introduction

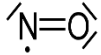
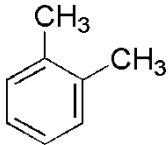
This chapter describes the methodology of experimental setup for the fabrication of composite nanofibers and the photocatalytic process employed in this study. The characterization methods of photocatalysts are also depicted in this chapter. The sampling and analytic methods of target compounds can be found in this chapter, and also how the generated intermediates are determined qualitatively and quantitatively are explicated in details.

## 3.2 Materials and Reagents

The materials used in the experiments are listed in Table 2.1. All the chemicals were used without further purification. The water used in the preparation of all the solutions was 18 M $\Omega$  deionized distilled water obtained from a Barnstead NANO pure water purification system.

Table 3. 1 Experimental chemicals.

Materials	Name	Manufactory	Purity
	Titanium isopropoxide (TIP)	Sigma Aldrich	97%
	Polyvinyl pyrrolidone (PVP) (MW = 360,000)	Sigma Aldrich	NA
	Acetic acid (HAc)	Sigma Aldrich	≥99.7%
	Ethanol	Advanced	95%
	Zinc acetate (ZnAc)	Sigma Aldrich	≥98%
$\text{Bi}(\text{NO}_3)_3 \cdot 5\text{H}_2\text{O}$	Bismuth(III) nitrate pentahydrate	Sigma Aldrich	≥98%
	Rhodamine B (RhB)	Acros	~96%

	Nitrogen monoxide	BOC gas	98.5%
	o-Xylene	Scientific Gas Engineering Co., Ltd.	$\geq 99.0\%$

### 3.3 Preparation of composite nanofibers

Electrospinning is a widely used fabrication technique for fabricating continuous, electro-active nanofibers from a wide range of materials with diameters in the range of several nanometers to the micrometer regime. Out of various classifications of materials, nanofibers by electrospinning can be successfully obtained from polymers, semiconductors, ceramics and their composites. Because of the decrease in the fiber diameter to nanoscale, these materials show enhanced properties of high surface area to volume ratio, porosity, flexibility, electrochemical and mechanical properties, which make them excellent candidates for a broad range of applications such as in energy conversion and storage devices, electronic devices and tissue engineering etc.

The basic principle behind the processing of nanofibers by electrospinning is based on the unidirectional elongation of a spin-able viscoelastic solution by considering various parameters involved in the process of electrospinning. Continuous nanofibers are formed due to the electrostatic Coulombic repulsive forces applied during elongation of the viscoelastic solution as it stretches to form a fiber. For a schematic representation of the electrospinning set-up shown in Figure 3.1, a viscoelastic solution is first loaded into a syringe and fed through a flow meter pump. When a high

electric potential is applied to the spin-able solution, at a threshold voltage usually around 6 kV, the repulsive force developed in the electro-active solution is greater than its surface tension and a droplet, namely a Taylor cone, is formed at tip of syringe. This droplet is further elongated because of electrostatic forces, which results in evaporation of the solvent and formation of solidified nanofibers, which are usually collected randomly on the grounded static/rotating mandrel collector substrates. Although the electrospinning process is simple, because of various instabilities such as the Rayleigh instability, an axisymmetric instability, and whipping/bending instability, it is very complicated to control the diameter and morphology of nanofibers for use in potential applications.

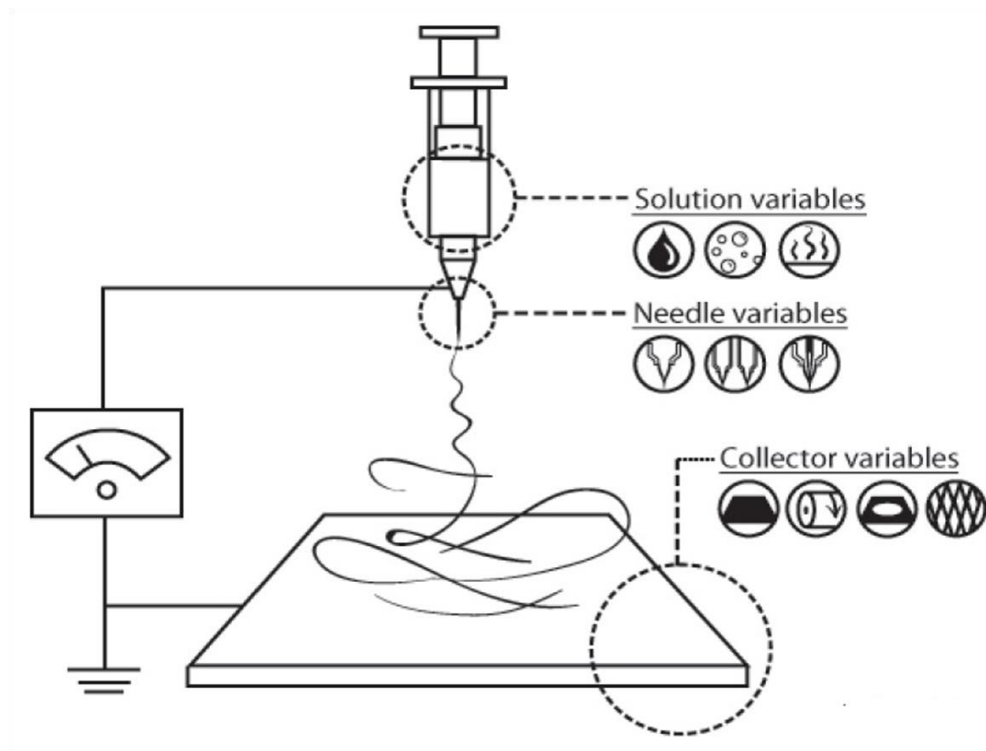


Figure 3.1 Schematic setup for a traditional electrospinning setup.

In this study, the nozzle-less electrospinning device is applied to fabricate nanofibers. The picture and sketch of the nozzle-less electrospinning are shown respectively in

Figure 3.2 a and b. The electrode in form of a rotating cylinder is set at a high positive voltage of 75 kV and the distance between the electrode and the ground collector is adjusted to 19 cm. The electrode is partially submerged in a trough of feed solution. A very thin film (less than 1 mm) of the solution is being continuously conveyed out of the liquid pool by the rotation of the electrode. Under the electric field with high intensity, the thin film coated on the rotating electrode develops into numerous unstable “Taylor cones” wherein the liquid droplet carrying positive charge jets out of the film toward the ground electrode. As the jet leaves the rotating electrode in form of a fine thread, neighboring positive charges deposited on the thread repel against each other thereby stretching the thread further to a smaller diameter fiber. This process continues until thin nanofibers reach the ground collector. During free flight in air, evaporation of liquid from the fiber by ventilation in the chamber further enhances the formation of the nanofibers.



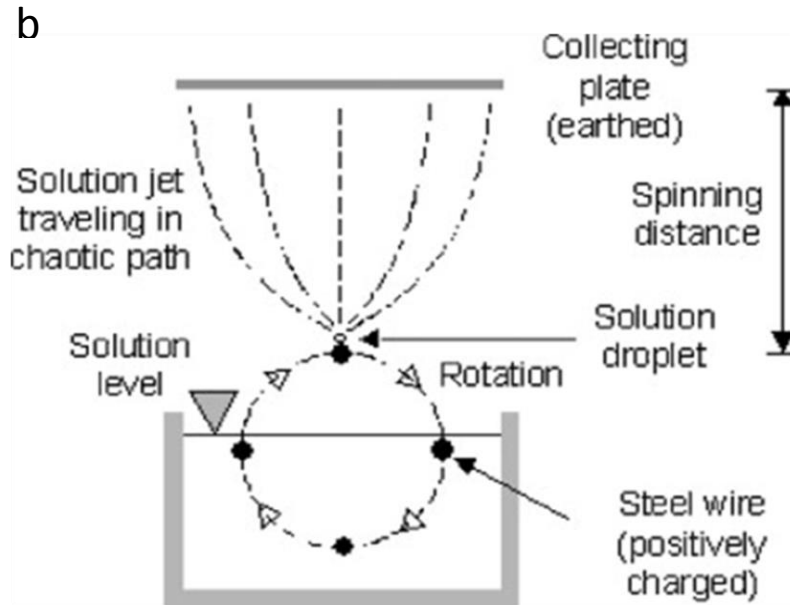


Figure 3.2 Schematic setup for nozzle -less electrospinning setup.

The typical spinning solution was prepared by the following procedures. Based on a sol-gel method, TIP and isometric HAc were mixed with PVP powders and ethanol under ultrasonic mixing for 30 min. Subsequently, a portion of ZnAc and/or  $\text{Bi}(\text{NO}_3)_3$  was added to the solution by sufficiently ultrasonic dispersing for 6 h to obtain a homogeneous solution. The precursor solution is fed to the trough of the needless electrospinning machine for producing nanofibers under present conditions. The fresh precursor nanofibers prepared from electrospinning were kept in air for 12 h during which the TIP components were fully transformed to  $\text{TiO}_2$  due to hydrolysis. Finally, the fibers were calcinated for 2 h in air to remove the organic fractions yielding ultimately the composite nanofibers.

## **3.4 Characterization of the prepared composite nanofibers**

### **3.4.1 Thermal behavior**

Thermo gravimetric analysis (TGA) is a method of thermal analysis in which changes in physical and chemical properties of materials are measured as a function of increasing temperature (under constant heating rate), or as a function of time (under constant temperature and/or constant mass loss). TGA can provide information about physical phenomena, such as second-order phase transition, including vaporization, sublimation, absorption, adsorption, and desorption. Likewise, TGA can provide information about chemical phenomena including chemisorptions, desolvation (especially dehydration), decomposition, and solid-gas reactions (e.g., oxidation or reduction).

The thermal decomposition behavior of precursor xerogel was examined using a thermo gravimetric analyzer and differential scanning calorimeter (TGA–DSC) (Netzsch) under ambient pressure in the temperature range between 30 and 1000 °C at a controlled heating rate of 10 °C min<sup>-1</sup>.

### **3.4.2 Morphology characterizations**

The morphology of nanostructure was characterized by scanning electron microscopy (SEM, JEOL Model JSM-6490) and transmission electron microscopy (TEM, JEOL 2100F). The equipments were also equipped with an energy dispersive X-ray spectroscopy (EDS) detector to carry out the X-ray analysis for the elements in the test samples.

### **3.4.3 Crystal structure characterization**

The crystal forms of the TiO<sub>2</sub> nanofiber under different calcination temperatures were investigated by X-Ray diffraction (XRD). In this work, the XRD was performed by Rigaku 9KW Smartlab using Cu k $\alpha$  ( $\lambda=0.1540\text{nm}$ ) radiation.

The crystal phases were identified from the PDF card, JCPDS card No. 21-1272 for anatase, JCPDS card No.21-1276 for rutile, JCPDS card No.65-682 for zinc oxide, and JCPDS card No. 41-1449 for bismite.

### **3.4.4 BET test**

Specific surface area (SSA) is an important aspect in heterogeneous photocatalysis. It is a property of materials, which is the total surface area of a material per unit mass, solid or bulk volume, or cross-sectional area. It is a derived scientific value that can be used to determine the type and properties of a material (e.g. soil). It is defined either by surface area divided by mass (with units of  $\text{m}^2/\text{kg}$ ), or surface area divided by the volume (units of  $\text{m}^2/\text{m}^3$  or  $\text{m}^{-1}$ ).

The SSAs of nanofibers in different diameters were tested by NOVA<sup>R</sup> – 1200 Surface Area Analyzer using N<sub>2</sub> adsorption. All samples were pre-treated at 250 °C for 5 h in vacuum for out-gassing.

### **3.4.5 Spectroscopic Measurement**

#### **3.4.5.1 UV-Visible absorption and reflectance spectra**

The UV–Vis diffuse reflectance spectra (DRS) were recorded on a Varian Cary 100 Scan UV–Vis system equipped with a Labsphere diffuse reflectance accessory to

obtain the reflectance spectra of the catalysts over a range of 200–800 nm. BaSO<sub>4</sub> (Labsphere USRS-99-010) was used as a reference in the measurement. The measured spectra were converted from reflection to absorbance by the Kubelka–Munk equation.

For a crystalline semiconductor, the optical absorption near the band edge is expressed by the formula

$$\alpha h\nu = A(h\nu - E_g)^{n/2} \quad (3.1)$$

where  $\alpha, h, \nu, E_g$  and  $A$  correspond to absorption coefficient, Planck constant, light frequency, band gap energy, and a constant, respectively. Parameter  $n$  depends on the characteristics of the transition in a semiconductor. For a direct transition,  $n = 1$ , whereas for an indirect transition,  $n = 4$ . The absorption coefficient  $\alpha$  is proportional to the absorbance. For the composite photocatalyst, the transition was shown to be indirect. The band gap energy is estimated on the plot  $(\alpha h\nu)^{1/2} = f(h\nu)$  by the intercept of the tangent to the plot with abscissa (Hu et al. 2006, Xiang et al. 2012).

#### **3.4.5.2 Photoluminescence spectrum**

Photoluminescence (PL) is light emission from a test sample (taking a various form) after the absorption of photons (electromagnetic radiation). It is one of many forms of luminescence (light emission) and is initiated by photoexcitation (excitation by photons), hence the prefix photo. The excitation typically undergoes various relaxation processes with subsequent photons being re-radiated. The period between absorption and emission can be extremely short: it ranges from the femtosecond-regime for the emission from, e.g., free-carrier plasma in inorganic semiconductors up to milliseconds for phosphorescent processes in molecular systems; however, it can also be extended into minutes or hours under special circumstances.

The observation of photoluminescence at certain energy can be seen most-straightforwardly as indication of population of the state associated with this transition energy.

PL data was measured using an Edinburgh FLSP920 spectrophotometer with an incidence-and-detection angle of 45° at room temperature. The emission spectrum was measured at an excitation using a 325-nm monochromatic filter and an increment of 1nm was adopted for data collection.

### **3.4.6 X-ray photoelectron spectroscopy**

X-ray photoelectron spectroscopy (XPS) is a powerful surface analysis technique, which provides elemental information about a surface as well as chemical state information (Scuderi et al. 2009, Watt 2003, Hu et al. 2007, Zhao et al. 2003). A sample material is bombarded by mono-energetic soft X-rays, resulting in electrons being ejected. Emitted photoelectrons from the sample material are collected as a function of their energies from which binding energies can be calculated by the Einstein equation:

$$E_b = h\nu - E_k - \varphi \quad (3.2)$$

Where  $E_b$  is the binding energy of the electron,  $E_k$  is the kinetic energy and  $\varphi$  is the work function of the spectrometer. On a finer scale it is also probable to identify the chemical state of the elements present from small variations in the determined kinetic energies.

The relative concentrations can be obtained with the sensitivity of 0.1-1% for a monolayer (around  $10^{15}$  atoms/cm<sup>2</sup>) from the measured photoelectron intensities. The

intensity  $I_A$  of a photoelectron peak of element A is given by

$$I_A = I_{RX} \sigma_A f(E_k) \int_0^{\infty} \{C_A(z) \exp[-z/(\lambda_A \sin \alpha)]\} dz \quad (3.3)$$

where  $I_{RX}$  is the intensity of the incident X-rays,  $\sigma_A$  the cross section of emission of a photoelectron from an inner core shell of A,  $f(E_k)$  the detection efficiency of the spectrometer for a photoelectron with a kinetic energy  $E_k$ ,  $C_A(z)$  the concentration of element A as a function of the depth  $z$ ,  $\lambda_A$  the inelastic mean free path of a photoelectron emitted by A and  $\alpha$  the take-off angle of the photoelectron with respect to the surface of the sample. In a homogeneous matrix, the concentration of  $C_A$  can be approximated by the relation:

$$C_A = \frac{\left(\frac{I_A}{S_A}\right)}{\sum_{i=0}^n \left(\frac{I_i}{S_i}\right)} \quad (3.4)$$

where  $S_i$  is the relative atomic sensitivity factor. Typically, the XPS probes 2-20 atomic layers (3-10 nm) deep for a solid sample. The energy of the photoelectron depends on the angle (with respect to the surface) of the measurement. The escape depth  $z$  of the photoelectron depends on its inelastic mean free path length  $\lambda$  as well as on its emission angle  $\alpha$  with respect to the surface. The sampling depth can therefore be varied by making use of the equation:

$$z = \lambda \sin \alpha \quad (3.5)$$

The lateral resolution of this technique is approximately 2-10  $\mu\text{m}$ .

XPS measurements can provide a semi-quantitative elemental analysis of surfaces, as well as chemical state analysis for vacuum-compatible materials, which cover with a diversity of materials from biological to metallurgical samples. Due to the very small

emission cross-sectional area and the corresponding long analysis times, this technique is not applicable to hydrogen and helium.

### **3.4.7 Electrochemical impedance spectroscopy**

Electrochemical impedance spectroscopy (EIS) can be used to investigate the electron transport properties in electrochemical devices. In EIS, the potential applied to a system is disturbed by a small sine wave modulation and the resulting sinusoidal current response is recorded as a function of modulation frequency. The impedance is defined as the frequency domain ratio of the voltage to the current and is a complex value. For the resistor (R), the impedance is a real value, which is independent of the modulation frequency. The capacitors (C) and inductors (L) both generate imaginary impedance, whose value change with frequency. The impedance spectrum of a real system, i.e., the impedance measured in a wide range of frequencies, can be described in forms of an equivalent circuit consisting of series and parallel connected elements R, C, L, and W (Warburg element which describes diffusion processes). From measurements of EIS, the following parameters can be deduced: series resistance, charge transfer resistance of the counter electrode, diffusion resistance of the electrolyte, resistance of electron transport, and recombination in the photoanode.

The nanofiber film was peeled off from the glass slide after 2h heat treatment and subsequently transferred to a clean FTO glass pre-coated with an ultra-thin adhesive layer made of TiO<sub>2</sub> paste. The EIS test sample was obtained after calcinated again at 450 °C for 2 h. The thickness was 20 μm from Surface Profiler and the active area was 10 mm<sup>2</sup>. The AC perturbation signal applied in this test was 10 mV over the frequency range of 1 MHz to 100 mHz. The illumination condition was AM 1.5

spectrum illumination with an incident power density of  $100 \text{ mW cm}^{-2}$  and a test temperature of 298 K. In the case of dark condition, EIS measurements on the test sample were carried out without light but with the same bias voltage as that under illumination.



Figure 3.3 Fabrication procedures for EIS test samples.

## 3.5 Photocatalytic performance test

### 3.5.1 Photocatalytic test in water

The photocatalytic experiment reaction suspension was prepared by adding  $0.5 \text{ g L}^{-1}$  catalysts into RhB aqueous solution with the initial concentration of  $10^{-6} \text{ M}$ . The full absorbance spectrum of RhB is given in Figure 3.4, which confirms that RhB does not have absorbance at 420 nm from the spectrum (no sensitization effect from the RhB dye). Before the irradiation, the suspension was magnetically stirred in dark for 15 min to reach an adsorption and desorption equilibrium, which is known as dark adsorption. The test photoreactor was 400 mm high with a square cross-section of  $300 \times 300 \text{ mm}^2$ . The reactor barrel has a diameter of 250 mm and a depth of 375 mm. The light sources of eight 8 W 420 nm lamps (Rayonet RPR-4190) were symmetrically placed in the Rayonet<sup>TM</sup> photochemical reactor RPR-200 (Southern New England Ultraviolet Company). The light source can be changed with lamps of different wavelength while rearranging the number of lamps involved in the test can

modify the intensity of irradiation. A UV–Visible spectrophotometer (Spectronic Genseys 2) was used to determine the concentration of RhB solution. The photocatalytic activity of the catalyst can be quantitatively evaluated by the apparent reaction rate constant. The experimental setup is shown in Figure 3.5. The benchmark tests were processed with the same test set-up but at a different light irradiation with wavelength of 365 nm (Philips TL8 W BL).

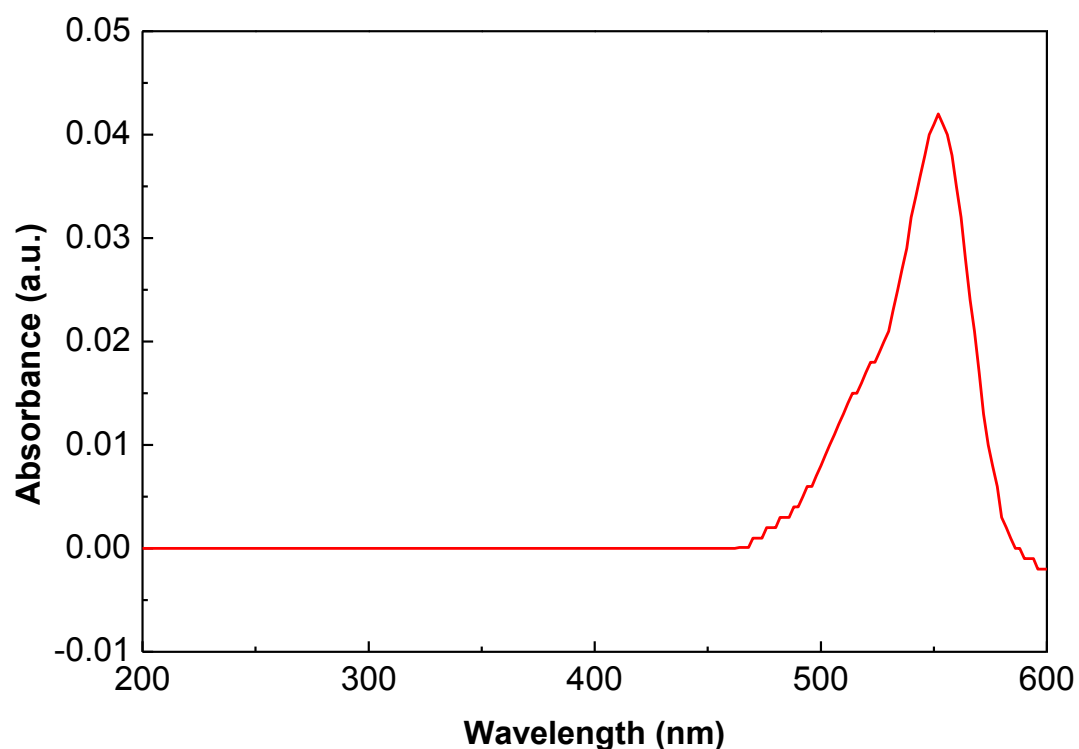


Figure 3.4 Full UV–Vis spectrum of RhB solution.

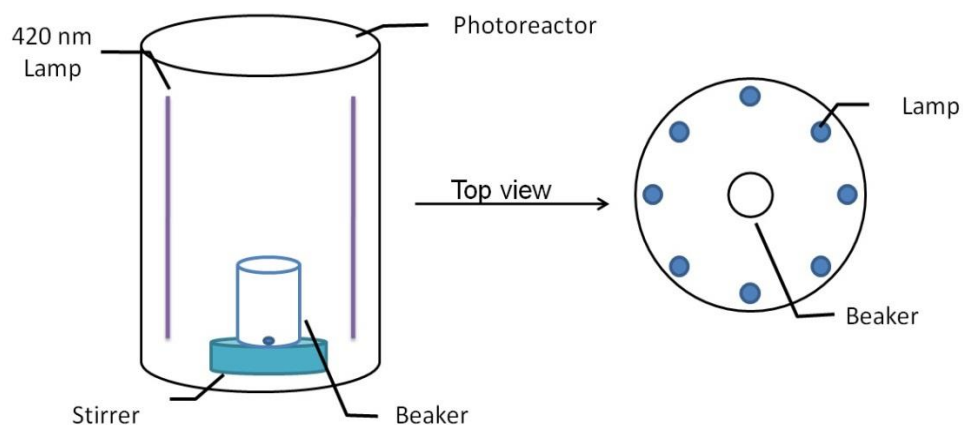


Figure 3.5 Sketch of the Rayonet™ photochemical reactor.

## 3.5.2 Photocatalytic test in air

### 3.5.2.1 Photocatalytic conversion of NO

The photocatalytic experiments for the conversion of NO in air were carried out in a continuous flow reactor at ambient temperature. The key mechanisms for the oxidation of NO are summarized below [12, 13]:



The electron in the conduction-band reacts with  $O_2$  forming the superoxide anion ( $O_2^-$ ).  $O_2^-$  will form  $\bullet HO_2$  radicals with water vapor in air. The  $\bullet HO_2$  radicals may react with NO forming  $NO_2$  and a hydroxyl radical. The byproducts can further react to form the end product nitric acid ( $HNO_3$ ).

The rectangular reactor, made of stainless steel with Saint-Glass cover, has a volume of 4.5 L ( $10 \times 30 \times 15 \text{ cm}^3$ ). A sample dish ( $150 \times 25 \text{ mm}$ ) containing nanofiber was positioned in the center of the reactor. The simulated solar light source was simulated using a 300 W commercial tungsten halogen lamp (General Electric), which was vertically positioned above the sample dish outside the reactor. Six mini-fans, blowing air, were distributed around the lamp to suppress any temperature rise during the reaction.

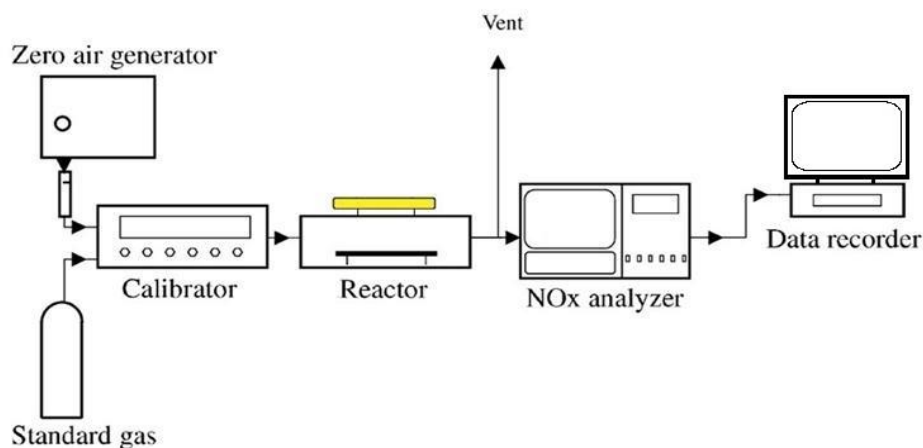


Figure 3.6 Experiment setup of photocatalytic reaction of NOx.

The NO gas was acquired from a compressed gas cylinder at a concentration of 50.1 ppm NO. The initial concentration of NO was diluted to about 1000 ppb by the air stream supplied by a zero-air generator (Thermo Environmental Inc. Model 111). The

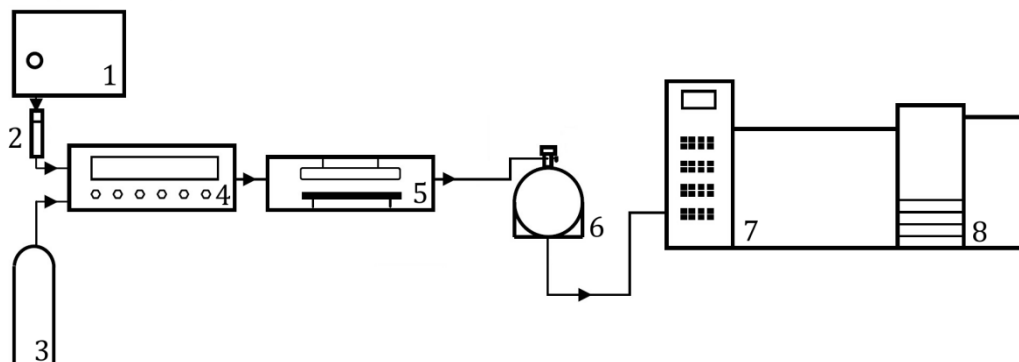
relative humidity (RH) level of the NO flow was controlled at 20%. The gas streams were uniformly mixed by a gas blender, and the total flow rate was controlled at 3 L min<sup>-1</sup> by a mass-flow controller. The lamp was turned on once the adsorption–desorption equilibrium was attained among water vapor, gases, and photocatalysts. The concentration of NO was continuously measured by a chemiluminescence NO analyzer (Thermo Environmental Instruments Inc. Model 42c), which can monitor NO, NO<sub>2</sub>, and NO<sub>x</sub> with a sampling rate of 0.7 L min<sup>-1</sup>. The removal rate (%) of NO was calculated from the concentration of NO in the feed and outlet streams, respectively. The reaction of NO with air can be ignored when performing a control experiment with, or without light, in the absence of photocatalyst.

### **3.5.2.2 Photocatalytic degradation of o-xylene**

Figure 3.7 shows a schematic diagram of the experimental setup for the o-xylene experiments. A reactor with a volume of 4.5 liter (10 × 30 × 15 cm<sup>3</sup>) with its surface coated by a Teflon film (BYTAC Type AF-21) was used for this study. Illumination was provided by a 300 W commercial tungsten halogen lamp (General Electric), which was horizontally positioned above the sample outside the reactor.

A zero air generator (Thermo Environmental Inc. Model 111) was used to supply the air stream. The desired humidity of the flow was controlled by blowing the zero air streams through a humidification chamber. The reactant stream and the zero air streams were connected to a mass flow calibrator (Advanced Pollution Instrumentation Inc. Model 700). The gas streams were pre-mixed by a gas blender and the desired flow was controlled by a mass flow controller inside the calibrator.

After the inlet and the outlet concentration achieved equilibrium (1 hour), the lamp was turned on and the reaction was initiated.



- |                       |                            |
|-----------------------|----------------------------|
| 1. Zero air generator | 2. Humidification chamber  |
| 3. Standard gas       | 4. Calibrator              |
| 5. Reactor chamber    | 6. Summa canister          |
| 7. Gas Chromatograph  | 8. Mass Selective Detector |

Figure 3.7 Schematic diagram of the experimental setup.

Pre-cleaned Summa canisters were evacuated for volatile organic compounds (VOCs) sampling. Constant VOC sampling time was achieved using a mass flow controller. Samples of VOC were collected at designated times during the experiment. After collection, the canister sample was first concentrated by a Nutech Cryogenic Concentrator (Model 3550A), and the trapped VOC were separated and analyzed by Hewlett Packard Gas Chromatograph (Model HP 6890) and quantified by a Mass Selective Detector (Model HP 5973). After analysis, the canister was sequentially evacuated and pressurized with humidified zero air until all compounds were purged with level detected smaller than 0.2 ppb.

## Chapter 4

# Fabrication and Photocatalytic Activity of TiO<sub>2</sub>/ZnO Nanofibers

### 4.1 Overview

Photocatalysis with semiconductors such as TiO<sub>2</sub> and ZnO has been an intensive research topic for their ability to degrade organic pollutants in water such as detergents, dyes, herbicides, and pesticides. Photocatalyst stands out from other methods of pollutant degradation due to their physicochemical properties, high photocatalytic activities, and relatively low costs (Suzuki et al. 2001). However, the conditions needed to utilize these semiconductor photocatalysts, such as UV irradiation, restrict their applications in reality. To improve the practical applicability of the photocatalyst, TiO<sub>2</sub>/ZnO nanocomposites are synthesized by chemical or physical processes for two purposes. The first objective is to extend the light adsorption spectrum and improve the efficiency of light utilization. The second objective is to suppress the recombination of photogenerated electron/hole pairs which reduces the function of the photocatalyst (Wang et al. 2001, Perkgoz et al. 2011, Bashouti et al. 2006, Wang et al. 2012). Nanosized TiO<sub>2</sub> coupled with ZnO can improve their photocatalytic efficiency due to the synergistic effect on photocatalytic properties (Zhao et al. 2008). The TiO<sub>2</sub>/ZnO nanocomposition not only improves the separation efficiency between the photogenerated electrons and electron holes, but also introduces both impurity and defect levels to the forbidden band of TiO<sub>2</sub>. As a

consequence, these benefits decrease the energy band gap of TiO<sub>2</sub> (See Figure 4.8) and reduce the excitation energy of the catalyst, leading to the red shift of the absorption range and increasing the utilization ratio of visible light. Another added benefit is that these processes can increase the lifetime of the separation of electrons and holes, thereby reducing the recombination rate of electrons and holes, which is a limitation of conventional photocatalyst.

It has been known that improved catalytically performance can be realized for catalyst with a larger specific surface area to enhance contact with pollutants. Thus, catalyst made into nano-scale with large specific surface is widely used. Most studies on the photocatalytical activities of TiO<sub>2</sub>/ZnO composites are in the form of nanoparticles because of their relatively large surface-to-volume ratio by virtue of their geometry (Zhao et al. 2008, Liu et al. 2009, Azouani et al. 2010). However, these nanoparticle photocatalysts may detach from the point of contact or adhesion, thus re-contaminating the treated water or air. Further, it is difficult to recover these nanoparticles because of their nano-size and dilute concentration (Bakhtari et al. 2006, Dreher 2004). Due to the large aspect ratios (length-to-diameter) of nanofiber, photocatalyst in the form of fiber is superior to particles as far as the recycling and aggregation are concerned. In 1934 Formahals patented the first invention of electrostatic spinning of nanofibers. In comparison with other spinning techniques, the electrostatic force is applied to draw out fibers from the minute drop (from instability) of spinning solution. Electrospinning produces nanofibers with many different linear-dimension shaped fibers such as round fibers, ribbons, filled and hollow tubes (Bashouti et al. 2006, Kim et al. 2008, Li and Xia 2004, Sun et al. 2003). Because of the ultrafine diameter, electrospun nanofibers have large specific surface areas. One cubic centimeter of material when drawn into 100-nm diameter nanofiber covers 40

m<sup>2</sup> of surface. With the expansion of electrospinning from polymers to composites and to ceramics, the applications of electrospun fibers are widely expanded. Also, some existing researches on TiO<sub>2</sub> and ZnO composite nanofibers are limited to the fabrication process (Lotus et al. 2011, Cai et al. 2010) and very little have been devoted to the application of the nanofibers utilizing their unique properties.

In the present study, the photocatalytic activities of TiO<sub>2</sub> nanofibers with the presence of zinc are systematically studied. The TiO<sub>2</sub>/ZnO composite nanofibers are prepared from a nozzle-less electrospinning solution system, with zinc acetate (ZnAc) and titanium tetraisopropoxide [Ti(OiPr)<sub>4</sub>] as precursor, polyvinyl pyrrolidone (PVP) as the fiber template, and ethanol as the solvent. The electrospun Ti(OiPr)<sub>4</sub>/ZnAc/PVP nanofibers is hydrolyzed and calcinated to obtain TiO<sub>2</sub>/ZnO composite nanofibers. The change in morphologies of TiO<sub>2</sub>/ZnO nanofibers with the calcination temperature are investigated to elucidate the synthesis mechanism using scanning electron microscopy combined with energy dispersive spectroscopy (SEM-EDS), thermo gravimetric analyzer and differential scanning calorimeter (TGA–DSC), X-ray photoelectron spectroscopy (XPS), diffuse reflectance UV-Vis spectrophotometer (DRS) and X-ray diffraction (XRD). Subsequently, the photocatalytic activity activities of the different TiO<sub>2</sub>/ZnO composite nanofibers are evaluated by measuring the photodegradation of Rhodamine B (RhB) dye in aqueous suspension under the irradiation of 420 nm visible light. The photocatalytic efficiency is investigated in relation to the ZnO content, and the catalyst loading in the reaction. Moreover, benchmarking tests are carried out among TiO<sub>2</sub> nanoparticles, TiO<sub>2</sub> nanofibers, and TiO<sub>2</sub>/ZnO nanofibers, all under the irradiation of UV light in the wavelength of 365 nm, to confirm the benefit of the latter.

## **4.2 Characterizations of TiO<sub>2</sub>/ZnO composite nanofibers**

### **4.2.1 Thermal behavior of precursor nanofibers**

From the thermal behavior of precursor xerogel electrospun fibers presented in Figure 4.1, four distinct stages of loss in mass can be identified in the TG-DSC curve. The first stage was between 30 and 170 °C with a broad peak in the DSC curve indicating the loss of solvent (such as ethanol and water) in the composite sol. In the second stage with temperature between 170 and 400 °C, there was a sharp exothermic peak at about 355 °C, which was due to decomposition of the side chains of PVP, acetate, titanate, and the by-products, such as isopropanol. In the third stage with temperature between 400 and 600 °C, an exothermic peak appeared in the TG-DSC curve at about 500 °C, which was attributed to the degradation of the main chain of PVP, and the phase transitions of TiO<sub>2</sub> and ZnO. Both TG and DSC curves became stable after 600 °C, indicating that water, ethanol and organic compounds in the precursor fibers have been completely removed.

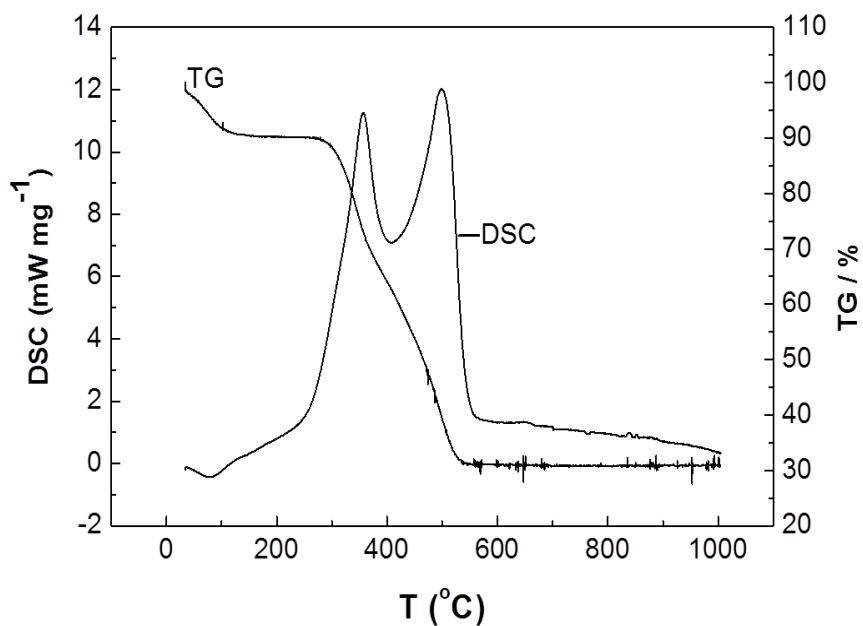


Figure 4.1 TG- DSC curves of the as-spun precursor  $\text{TiO}_2/\text{ZnAc}/\text{PVP}$  nanofibers.

#### 4.2.2 XRD analysis of composite nanofibers

The XRD patterns of both  $\text{TiO}_2$  nanofiber and  $\text{TiO}_2/\text{ZnO}$  composite nanofibers are shown in Figure 4.2.  $\text{TiO}_2$  exists in two main crystallographic forms, anatase (A) and rutile (R). The characteristic peaks of anatase and rutile crystal phase are  $25.28^\circ \text{A}$  (A101) and  $27.4^\circ \text{R}$  (R110), respectively. The XRD intensities of the anatase A(A101) and rutile R(R110) characteristic peaks have been analyzed. It can be seen that the fibers without Zn content are mainly in anatase phase. When ZnAc was introduced in the precursor solution, the presence of the ZnO phase was visible in the XRD. Also, the presence of Zn can be seen in the XPS spectra of the  $\text{TiO}_2/\text{ZnO}$  nanofibers in Figure 4.9, which contrasts with the negative result of  $\text{TiO}_2$  nanofibers that was included as a control in the XPS measurement.

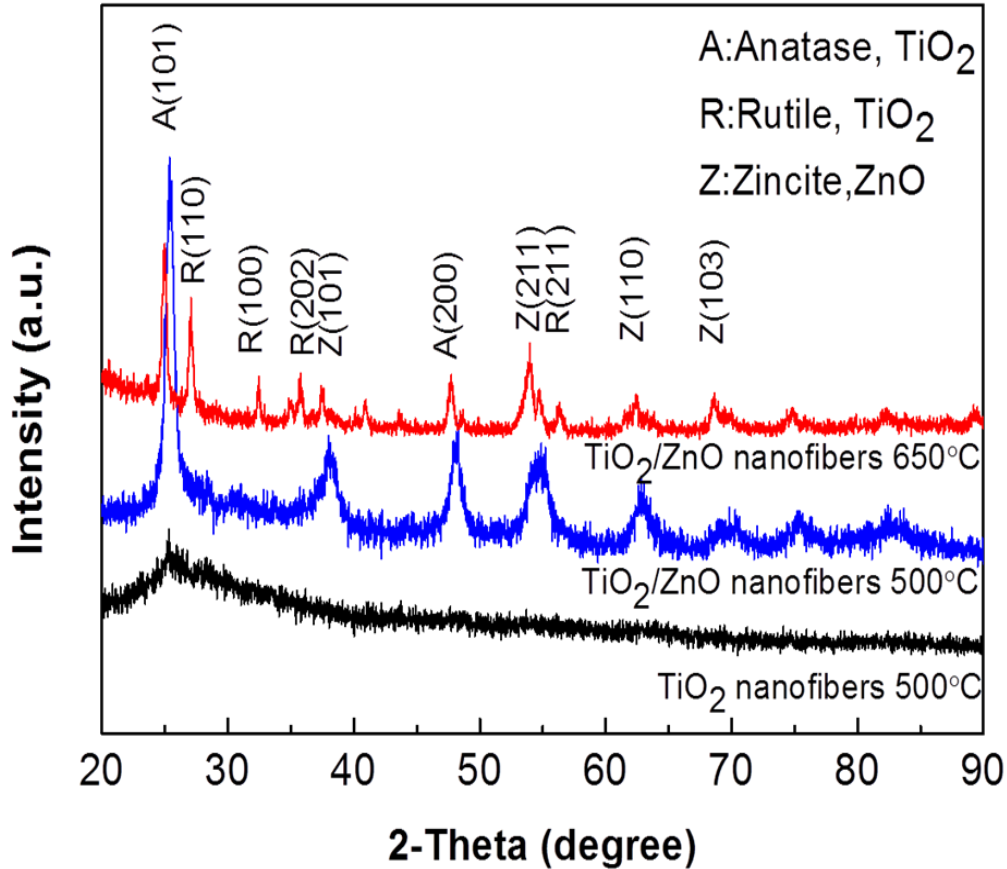


Figure 4.2 XRD patterns of  $\text{TiO}_2$  nanofibers and  $\text{TiO}_2/\text{ZnO}$  (6.0 % TIP, 0.30 % ZnAc) composite nanofibers calcined at different temperatures.

### 4.2.3 Morphology and crystal structure of composite nanofibers

The morphologies of the as-prepared nanofibers before- and after-calcination at different temperatures were characterized by SEM. The beam energy used in SEM experiments was 20 kV, which was labeled marked in the SEM pictures. The surface morphology and size of the samples varied depending on the calcination temperature as shown in Figure 4.3. The surface of as-spun, randomly oriented, composite fibers appeared to be relatively smooth and uniform due to the amorphous nature of the  $\text{Ti}(\text{OiPr})_4/\text{ZnAc}/\text{PVP}$  fibers. Diameter of nanofibers was calculated from high resolution SEM picture (in Figure 4.5a). The diameter distribution was plotted in

Figure 4.5b. The diameter of the precursor nanofibers ranged from 150 to 200 nm as shown in Figure 4.3a). The diameter of the finally formed nanofibers subsequently reduced to 80–100 nm due to evaporation of water and decomposition of PVP, ZnAc or Ti(OiPr)<sub>4</sub> after calcination, respectively, at 450, 500 and 650 °C as shown in Figure 4.3 b)-d). Despite the network structure still retained during the annealing process, a change in fiber morphology was observed after increasing the calcinations temperature to 650 °C. Here, some fibers were broken, exposing the loose ends of the fibers; moreover the surface became roughened as depicted in Figure 4.3d), which was attributed to burn-out of PVP, crystallization and coalescence of the grains. Based on this trial, the TiO<sub>2</sub>/ZnO nanofibers can be best prepared by sol–gel assisted nozzle-less electrospinning technique with calcination temperature at 500 °C.

Figure 4.4 shows the SEM images of the TiO<sub>2</sub>/ZnO composite nanofibers with different ZnAc contents in the precursor solution. It is apparent that the diameter of nanofibers slightly increases with increasing ZnAc contents. The statistical average diameter from SEM images versus the ZnAc content is shown in the inset of Figure 4.6, and an approximate linear relationship can be seen wherein larger fiber diameter results from increasing ZnAc contents in the precursor. The measured specific surface area (SSA) of nanofiber using BET test (detailed in Sec. 3.4.4) with different diameters is shown in Figure 4.6. When the diameter is increased from 80 to 120 nm the SSA decreases from 44.97 to 38.89 m<sup>2</sup> g<sup>-1</sup> due to reconfiguration of the fiber. This implies that the specific surface area for improved absorption of the visible light spectrum in the first stage adsorption of the photocatalytic reaction is sacrificed as the Zn content in the TiO<sub>2</sub>/ZnO composite nanofibers is increased.

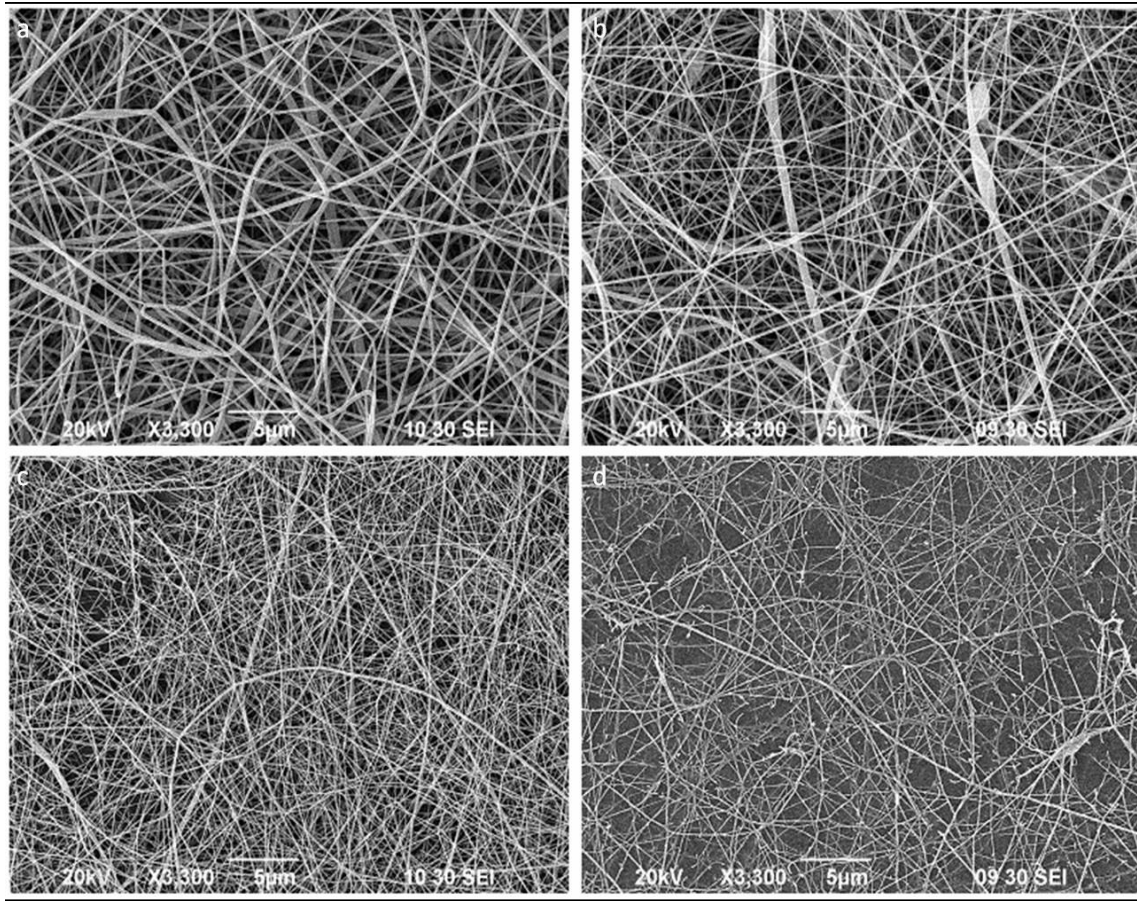


Figure 4.3 SEM pictures of  $\text{TiO}_2/\text{ZnAc}/\text{PVP}$  composite nanofibers calcined at different temperatures. a) Before calcination, b) 450 °C, c) 500 °C, d) 650 °C

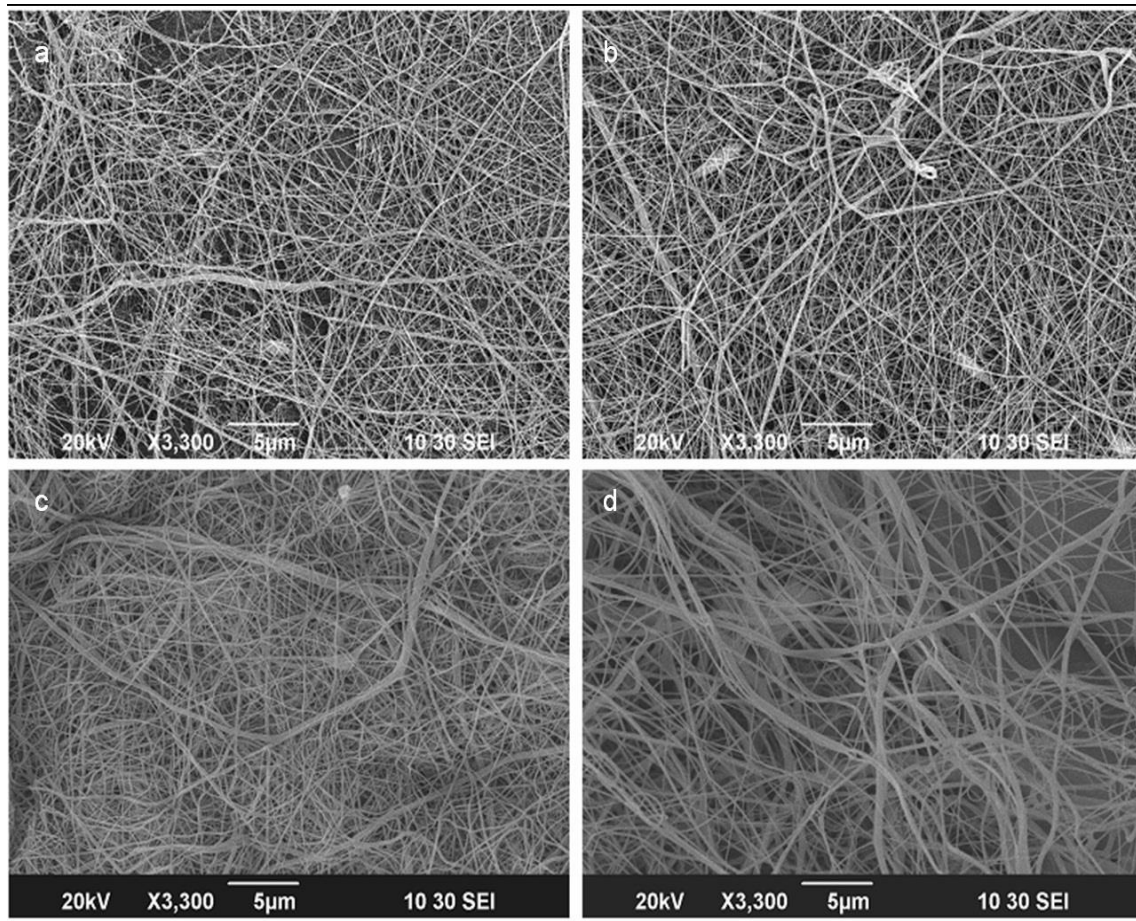


Figure 4.4 SEM images of the  $\text{TiO}_2/\text{ZnO}$  composite nanofibers with different zinc acetate contents in precursor solutions calcined at  $500^\circ\text{C}$ . a) 0.15 wt. %, b) 0.30 wt. %, c) 0.45wt. %, d) 0.60 wt. %.

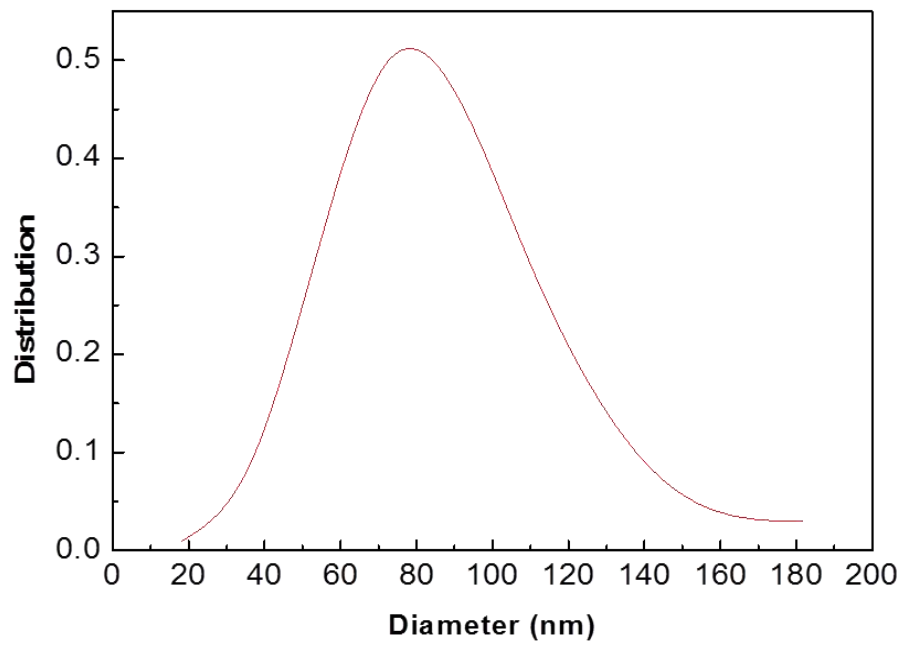
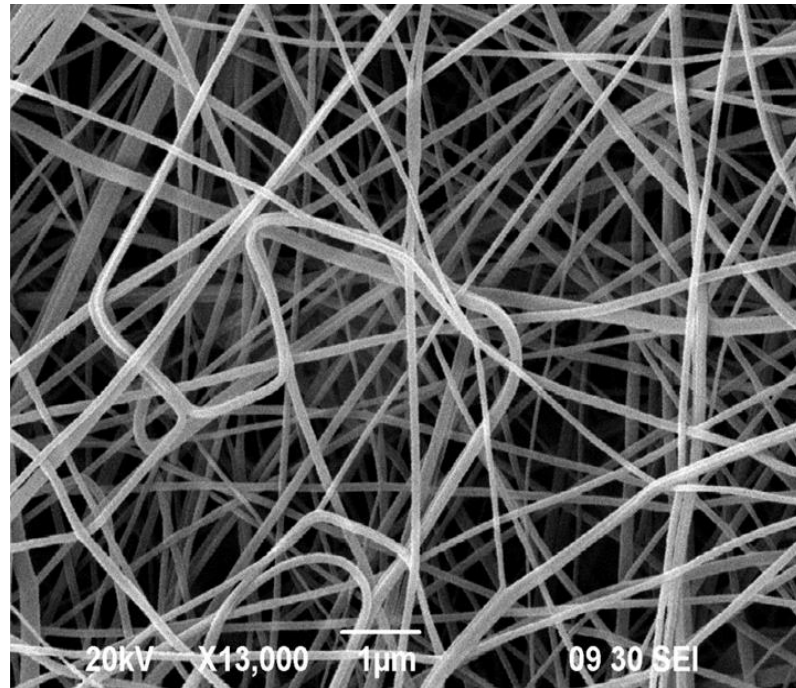


Figure 4.5 Mean diameter of fiber is calculated from high resolution SEM picture.

The figure below shows the diameter distribution of this SEM picture.

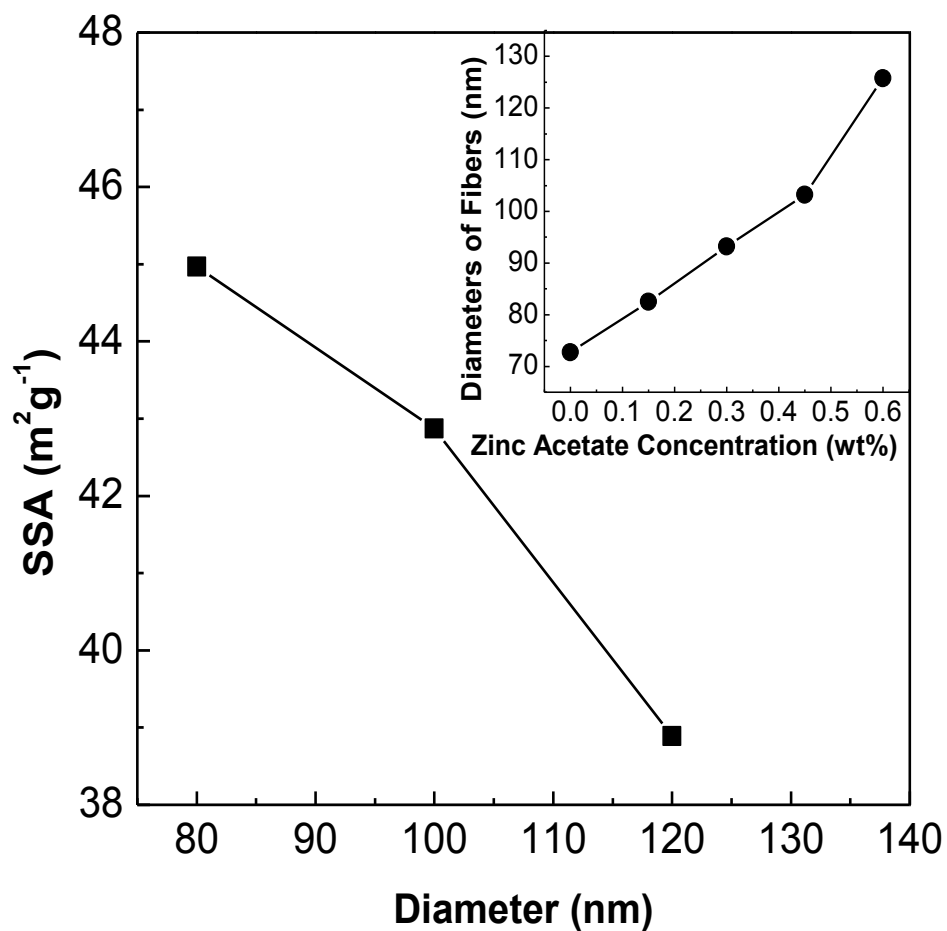


Figure 4.6 The specific surface areas (SSA) of nanofibers with different diameters, insert shows the  $\text{TiO}_2/\text{ZnO}$  nanofibers with different diameters obtained in the presence of different zinc acetate contents in precursor solutions.

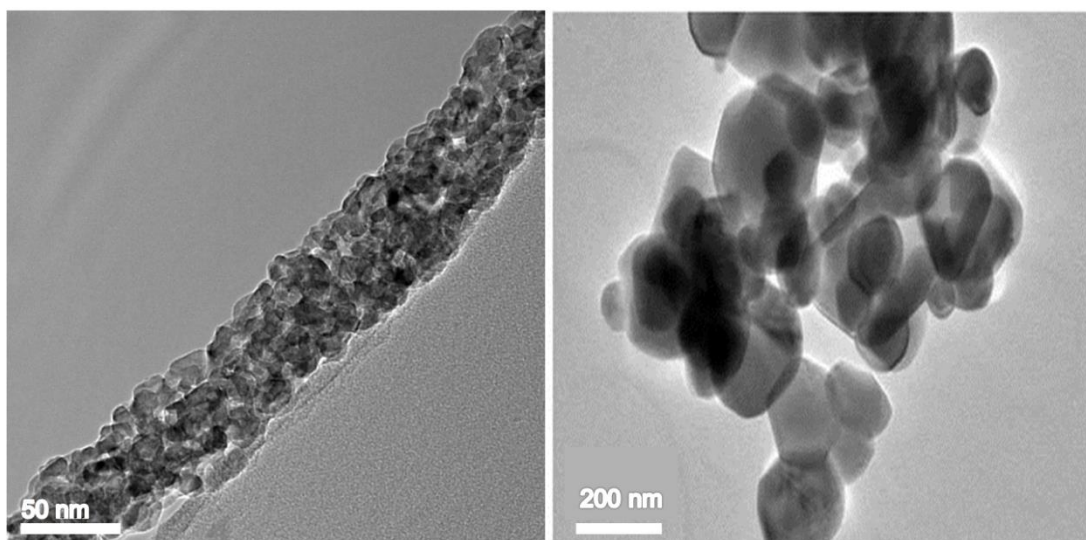


Figure 4.7 TEM images of  $\text{TiO}_2/\text{ZnO}$  nanofibers and benchmark  $\text{TiO}_2$  nanoparticles.

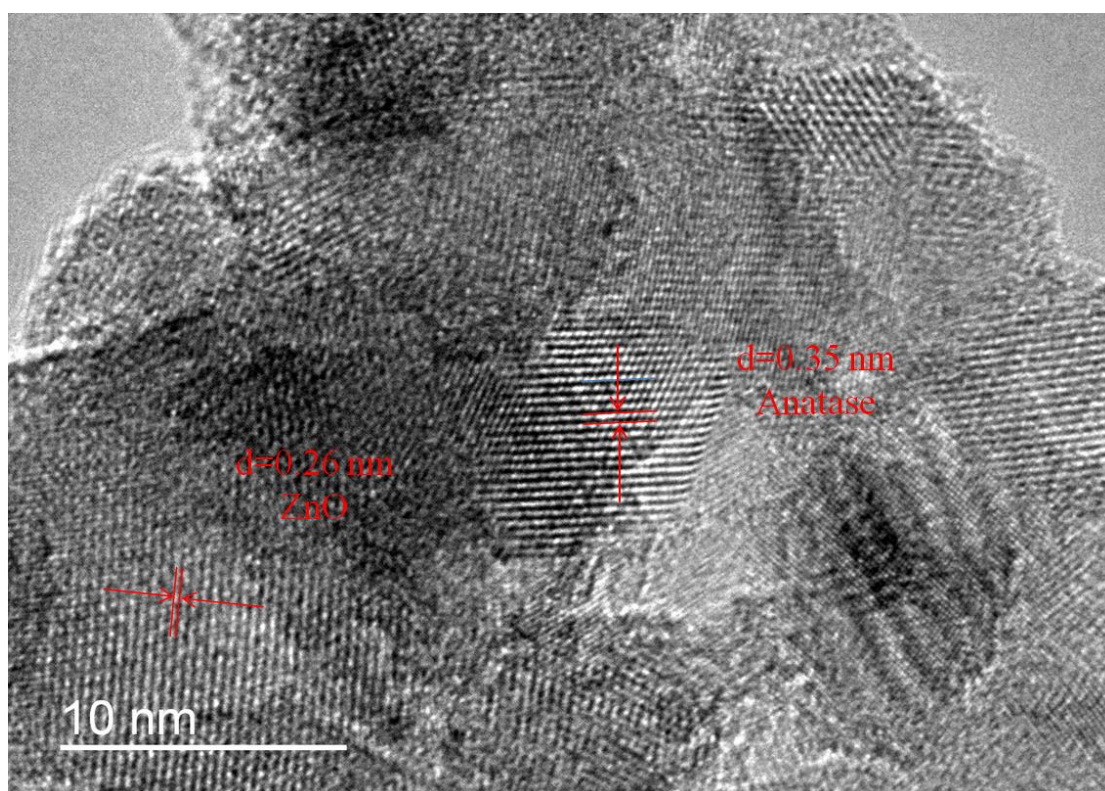


Figure 4.8 HRTEM picture of  $\text{TiO}_2/\text{ZnO}$  nanofibers

TEM image revealed that the  $\text{TiO}_2$  nanofibers were composed of compactly packed anatase nano-crystallites with sizes less than 10 nm.  $\text{TiO}_2$  crystallites had large surface-to-volume ratio, which favored the photocatalytic reaction as compared to the

crystals of TiO<sub>2</sub> nanoparticles (shown in Figure 4.7). The lattice spacing was determined from the HRTEM image (Figure 4.8) to be 0.35 and 0.26 nm between adjacent lattice planes of the nanofibers corresponding, respectively, to the distance between (101) crystal planes of the anatase phase of TiO<sub>2</sub> and the distance between (0002) crystal planes of ZnO.

#### **4.2.4DRS test of composite nanofibers**

The diffuse reflectance UV-Vis spectra of both TiO<sub>2</sub>/ZnO nanofibers and P25 nanoparticles were compared in Figure 4.9. From the absorption spectra between 200 and 800 nm, the absorption edge of TiO<sub>2</sub>/ZnO nanofibers has been red-shifted to the visible region. Using the well-known Kubelka-Munk equation, the band gap of TiO<sub>2</sub>/ZnO nanofibers and P25 nanoparticles were determined to be 2.87 eV and 3.08 eV, respectively. The decrease in band gap energy of TiO<sub>2</sub>/ZnO nanofibers can be attributed to the synergistic effect between the conduction band of ZnO and that of TiO<sub>2</sub>. Some sub-bands were formed introducing both impurity and defect levels to the forbidden band of TiO<sub>2</sub> thereby reducing the band-gap energy (Štengl et al. 2009, Perkgoz et al. 2011). Schematic diagrams for the principle of synergistic effect between TiO<sub>2</sub> and ZnO are shown in Figure 4.10.

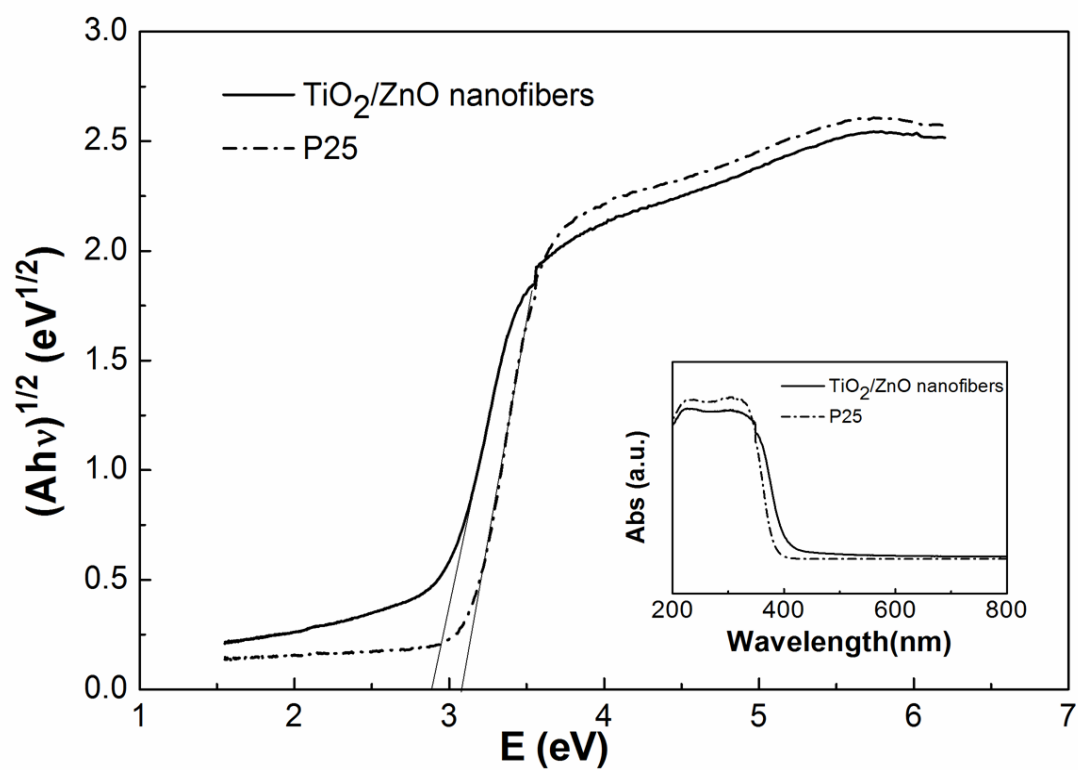


Figure 4.9 DRS of TiO<sub>2</sub>/ZnO nanofibers and P25 nanoparticles. Data are plotted as transformed Kubelka-Munk function versus the energy of light. Insert shows the absorption spectra between 200 and 800 nm.

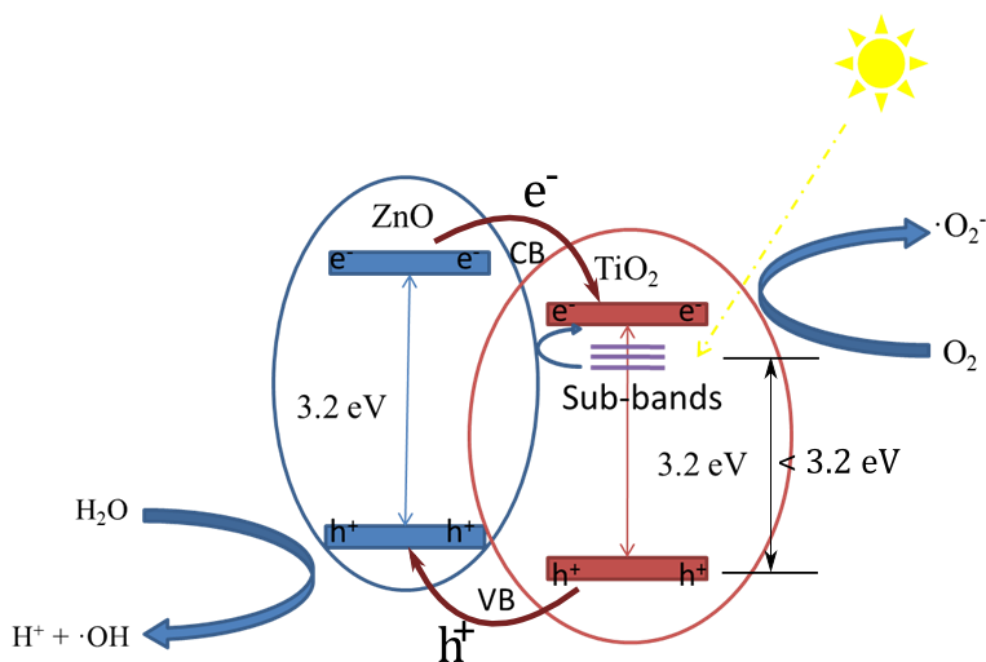


Figure 4.10 Schematic diagrams for the principle of synergistic effect between TiO<sub>2</sub> and ZnO.

#### 4.2.5 XPS analysis of composite nanofibers

The role of oxygen in the photocatalytic activity is examined by XPS test. The XPS spectra of TiO<sub>2</sub> nanofibers and TiO<sub>2</sub>/ZnO nanofibers are shown in Figure 4.11. The insert reveals the existence of ZnO in the composite nanofibers. As seen from Figure 4.12, the XPS spectra of O 1s of different doping concentration of ZnAc are asymmetric, indicating that there are at least two kinds of chemical states in the binding energy ranging from 528 to 535 eV. After curve fitting the measured data using the Origin software, the first peak of the XPS spectra curve corresponds to the crystal lattice oxygen in TiO<sub>2</sub> (O<sub>L</sub>) with the binding energy of O 1s in metallic oxide that exists in the range of 528-531 eV, and the second peak refers to the chemisorbed oxygen (O<sub>H</sub>) with binding energy being approximately 0.5 eV higher than that of O<sub>L</sub> peak (Yu et al. 2003). Surface oxygen vacancy (SOV) is an indication of the

chemisorbed oxygen that takes part in the oxidation of the pollutants. Higher SOV infers better ability for the catalyst to actively take part in the oxidation process as more hydroxyl radicals are formed on the surface of the catalyst. The SOV content of each sample were calculated from the XPS measurements and the analysis results were plotted in the inset of Figure 4.12. The SOV content increases from 12.54% to 24.31% as ZnAc in the precursor solution increases from 0 to 0.3% by weight, and subsequently it decreases back to 14.68% at higher ZnAc of 0.6%. This indicates that the SOV content of TiO<sub>2</sub> is generally enhanced by increasing the amount of Zn content and a maximum value of SOV can be achieved. As discussed, the increased SOV content is due to the increased chemisorbed oxygen. In essence, oxygen atoms adsorb physically on the surface of the catalyst and subsequently combine with electrons from the conduction band of the semiconductor to become chemisorbed oxygen. Chemisorption is one of the most significant stages in catalytic reaction. Thus, the process of increasing OH, such as increasing the Zn content in the TiO<sub>2</sub>/ZnO composite nanofibers, can benefit photocatalytic reaction.

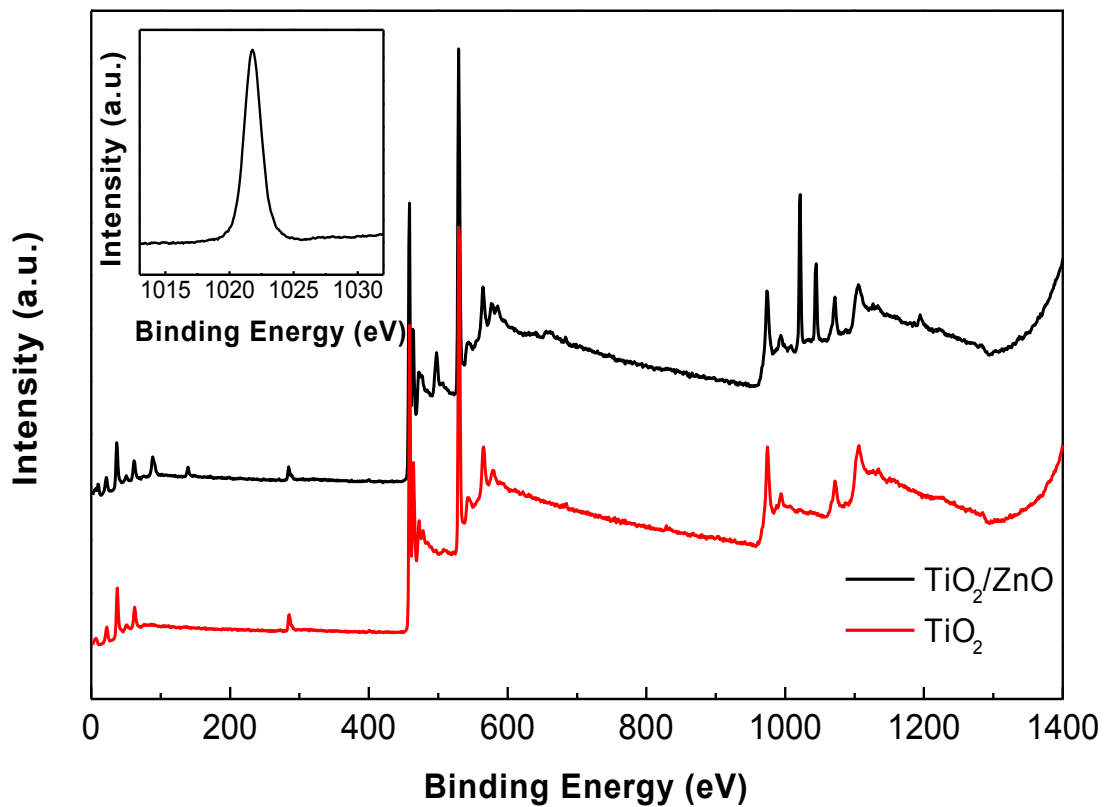


Figure 4.11 XPS spectra of TiO<sub>2</sub> nanofibers and TiO<sub>2</sub>/ZnO nanofibers. Insert shows the Zn spectrum of TiO<sub>2</sub>/ZnO nanofibers. It shows a peak at 1021.8 eV (Zn 2p<sup>3/2</sup>) indicating the presence of ZnO.

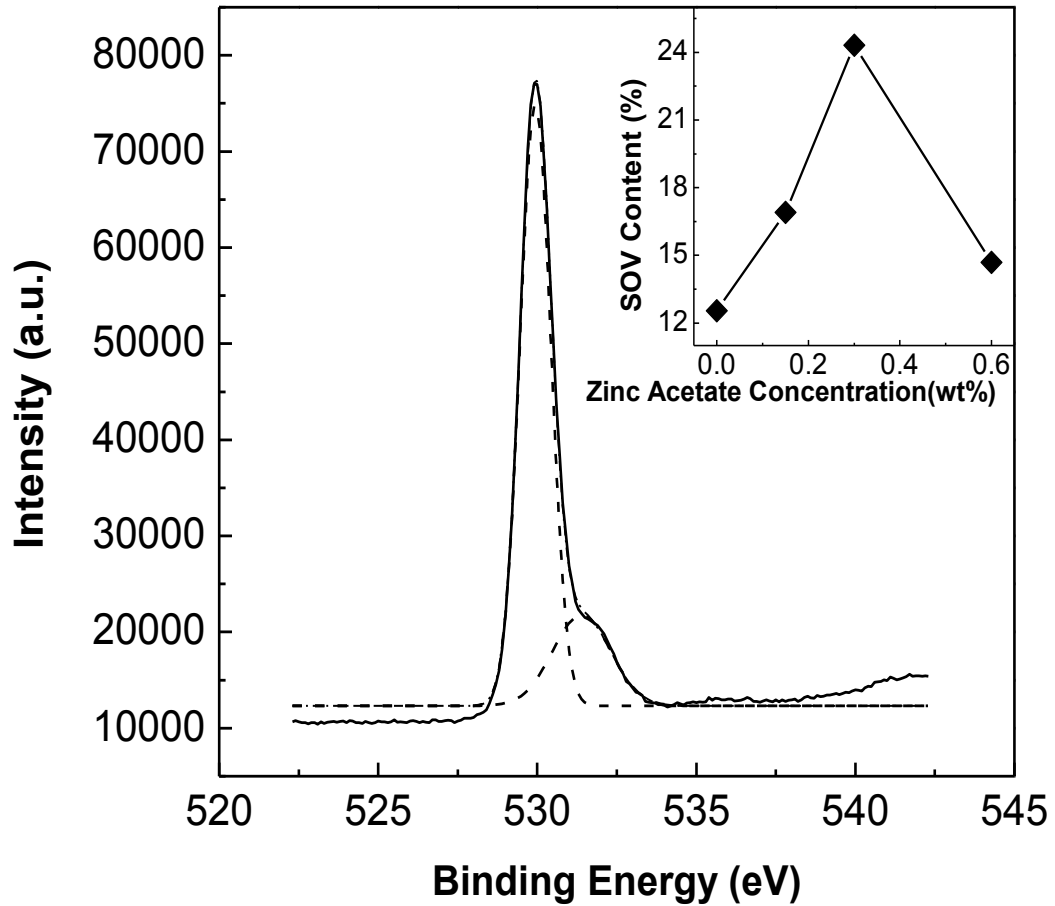


Figure 4.12 XPS spectra of O 1s curve fitting results of TiO<sub>2</sub>/ZnO composite nanofibers with zinc acetate content of 0.30 % (6.0 % TIP), insert shows the surface oxygen vacancy (SOV) contents of nanofibers obtained in the presence of different zinc acetate concentrations in the precursor solution.

## 4.3 Photocatalytic efficiency

### 4.3.1 Photocatalytic test on RhB in water

The photocatalytic activity of TiO<sub>2</sub>/ZnO composite nanofibers was evaluated by the photocatalytic degradation of RhB dye under the irradiation of visible lights at a wavelength of 420 nm. RhB has often been used as a model dye molecule for photocatalytic degradation by a transition metal oxide. Figure 4.13 shows the evolution of the concentration of RhB as a function of time during experiment with different ZnAc concentration in the precursor solution. The dark adsorption behavior of RhB for different samples, each with different nanofiber diameter, is shown in Figure 4.14. As evident, the adsorption rate constant behaved inversely related to the diameter of the nanofiber. This is due to the fact that larger diameter nanofiber results in smaller specific surface area (SSA) for adsorption, which is in accord with the results of Figure 4.6. Therefore, dark adsorption can play an important role in reducing the RhB in a two-step process (adsorption followed by oxidation) by deploying small-diameter nanofibers.

Of interest is that the wavelength of absorption peak of RhB is 556 nm, therefore photosensitization at 420-nm irradiation should be ruled out and the degradation of RhB with presence of TiO<sub>2</sub>/ZnO is strictly attributed to photocatalytic reaction (See Figure 3.4). The degradation rate of RhB was determined also from the rate constant based on the first order equation (see exponential decay of RhB concentration under “dark/photo” in Figure 4.13. The larger is the degradation rate of RhB, the higher is the photocatalytic activity. The photocatalytic degradation rate measurements of RhB for various samples with different ZnAc concentrations in precursor solutions are

displayed in Figure 4.15. The optimum Zn content (refers to ZnAc in the precursor) of TiO<sub>2</sub>/ZnO nanofibers is at 0.30%, which has the best photocatalytic degradation activity of RhB under visible light irradiation. This is in accord with the measurement of SOV indicating also a maximum amount of chemisorbed oxygen at 0.3% Zn. As discussed in the foregoing, TiO<sub>2</sub>/ZnO nanofibers have a high specific surface area. Reducing the diameter of the nanofibers results in increasing surface area as well as the available surface active sites, both of which benefit photocatalytic efficiency (Zhao et al. 2007). Also, the SOV content varies with the concentration of Zn in nanofibers. Higher SOV expresses better photocatalytic performance. Given the trade-off of SSA and SOV with Zn content in the TiO<sub>2</sub>/ZnO composite nanofibers, an optimized zinc concentration can be achieved when there is an optimal balance between these two factors. The results of the photoreaction experiments results were indeed in accord with the characterization tests.

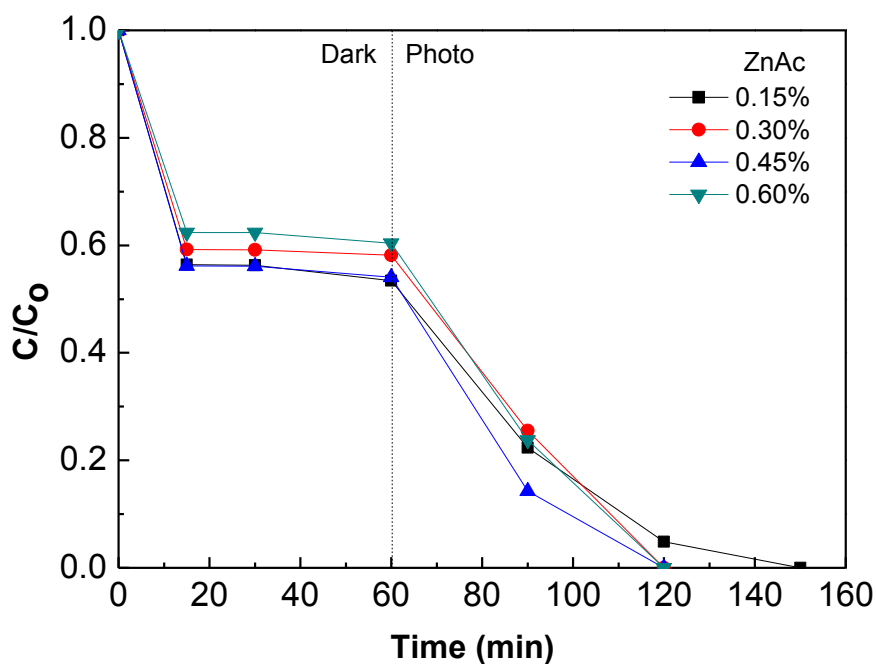


Figure 4.13 Adsorption and photodegradation of RhB ( $10^{-6}$  M) with various ZnAc

dopant TiO<sub>2</sub> nanofibers in suspension (0.5g L<sup>-1</sup>).

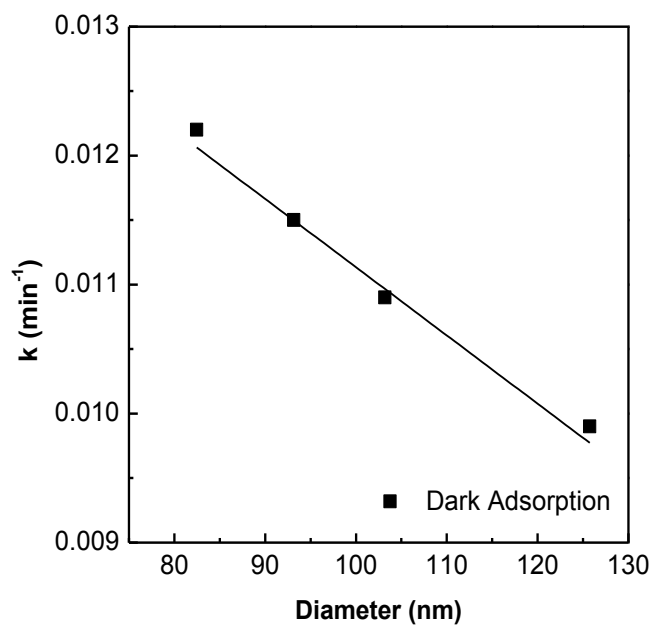


Figure 4.14 Rate constants of the adsorption of RhB of different diameter of fibers.

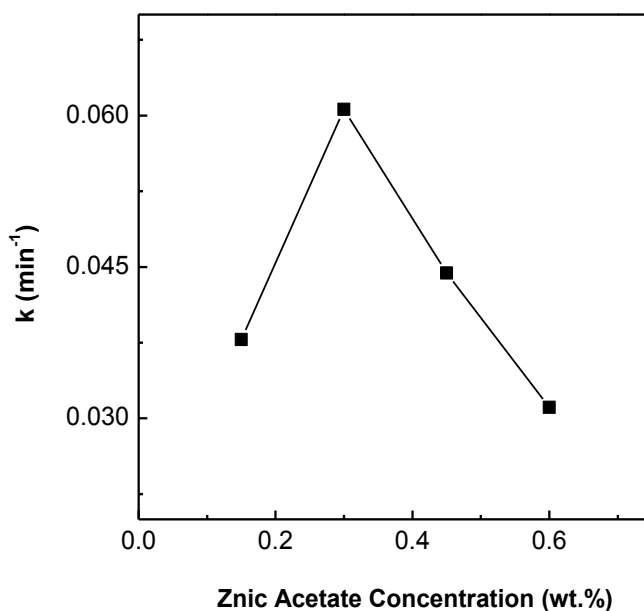


Figure 4.15 Rate constants of photocatalytic degradation of RhB of different zinc acetate contents in the precursor solution with the catalyst loading of 0.5 g L<sup>-1</sup> under

light irradiation intensity of 750 lux.

Several studies have shown that the photocatalytic degradation rate initially increases with increasing catalyst loading and subsequently decreases at high catalyst dosage (Sakthivel et al. 2003, Nagaveni et al. 2004, Evgenidou et al. 2005, Sobana and Swaminathan 2007). Under low catalyst loading, the degradation efficiency is enhanced with increasing catalyst concentration due to the increased number of active sites in the solution. On the other hand, too high a catalyst loading can lead to two detrimental effects. First, the excessive catalyst results in increasing opacity of the suspension thereby blocking light penetration and increasing light scattering in the suspension resulting in poor photoreaction. Second, agglomeration of the nanofibers results from excessive catalyst dosage and this ends up in reduction of surface area available for light absorption. Therefore, an optimal catalyst loading for the photocatalytic reaction exists as a result of the balance between these two opposing factors. In the investigation, both the increase and decrease of photocatalytic rate have been observed when the catalyst loading was increased. As shown in Figure 4.16, the optimum concentration for efficient removal of RhB was determined to be 2 g  $\text{TiO}_2/\text{ZnO}$  nanofibers per liter of suspension.

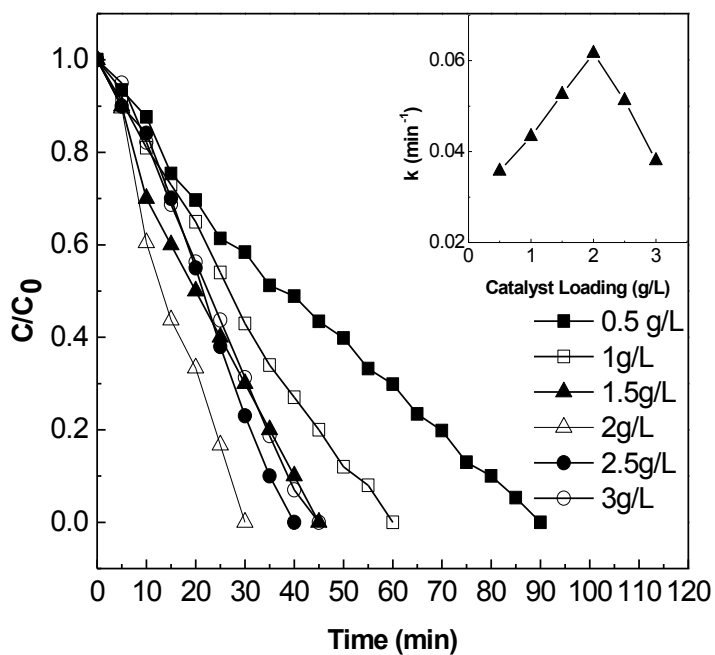


Figure 4.16 Rate constants of photocatalytic degradation of RhB of different catalyst loading with 0.30 wt. % zinc acetate in the precursor solution under the light intensity of 450 lux.

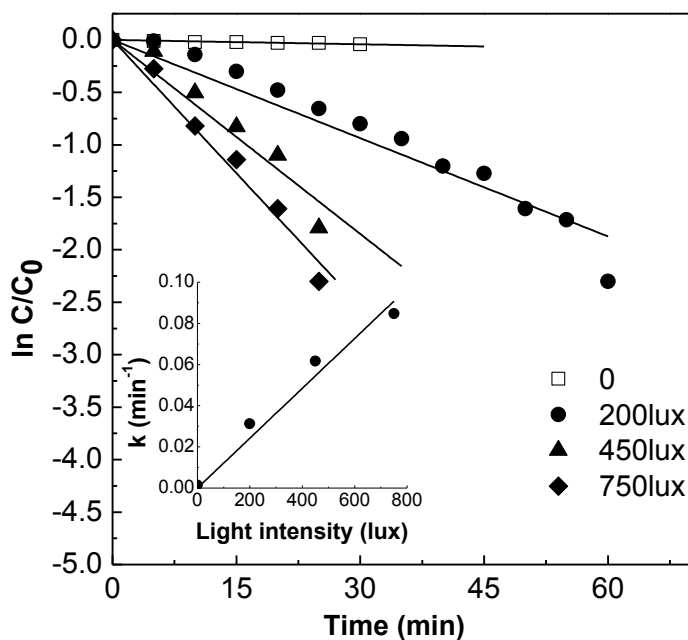


Figure 4.17 Light intensity effect on the photocatalytic reaction of RhB at a constant catalyst loading of 2 g L<sup>-1</sup> with 0.30 wt. % zinc acetate in the precursor solution.

The effect of light intensity was also investigated for the degradation of RhB (see Figure 4.17). The light intensity to which the reactor was exposed was determined from the light meter (Extech). When light intensity is nearly zero, the degradation rate of RhB is negligible (0.0014), which further confirms that the adsorption and desorption equilibrium had been reached after 15 min of mixing and stirring. With increasing light intensity, the photocatalytic degradation rate of RhB was found to increase. The increase in the rates was solely due to the increase of photon dosage that induced more electron-hole pairs generation on the surface of catalyst.

To confirm the benefits of the new nano-photocatalyst, benchmark tests were carried out among commercial TiO<sub>2</sub> nanoparticles, as-prepared TiO<sub>2</sub> nanofibers and TiO<sub>2</sub>/ZnO nanofibers under UV irradiation (365 nm). These three photocatalysts, all at the same dosage, were tested respectively with identical initial concentration of RhB; and the results are depicted in Figure 4.18. The photocatalytic reactions took place after dark reaction when the adsorption and desorption equilibrium was achieved. The reaction rates of TiO<sub>2</sub> nanoparticles (~35-nm diameter), TiO<sub>2</sub> nanofibers (~72-nm diameter) and TiO<sub>2</sub>/ZnO nanofibers (~93-nm diameter) were 0.025, 0.036, and 0.054, respectively. The specific surface area (SSA) of nanofibers with diameter of 100 nm from BET test was determined to be 42 m<sup>2</sup> g<sup>-1</sup>; while the SSA of nanoparticles was given by the supplier as 40 m<sup>2</sup>g<sup>-1</sup> which is quite comparable to that of the nanofibers. Unlike the single-crystal nanoparticles, nanofibers have a poly-nanocrystallite structure with each crystallite about 10 nm in size packed on the nanofibers (Yang and Leung 2011). The nanopores in these nanocrystals would promote the absorbance of the target compound RhB, thus enhancing the catalytic reaction. The advantage is more pronounced as the diameter of the nanofibers is further reduced. Besides the band gap energy of TiO<sub>2</sub>/ZnO nanofibers is lower, the

excitation energy of the catalyst is also reduced leading to the red shift of the absorption range and increasingly utilizing of visible light. In addition, this process can increase the time period of the separation of electrons and holes, thereby reducing the recombination rate (Štengl et al. 2009). All of these benefits increase the photocatalytic reaction activity of TiO<sub>2</sub>/ZnO nanofibers in relation to TiO<sub>2</sub> nanofibers and TiO<sub>2</sub> nanoparticles as evident in Figure 4.18. This provides a rationale on the fast kinetics of TiO<sub>2</sub>/ZnO nanofibers, followed by TiO<sub>2</sub> nanofibers, and lastly TiO<sub>2</sub> nanoparticles despite the diameter of these test samples are in inverse trend.

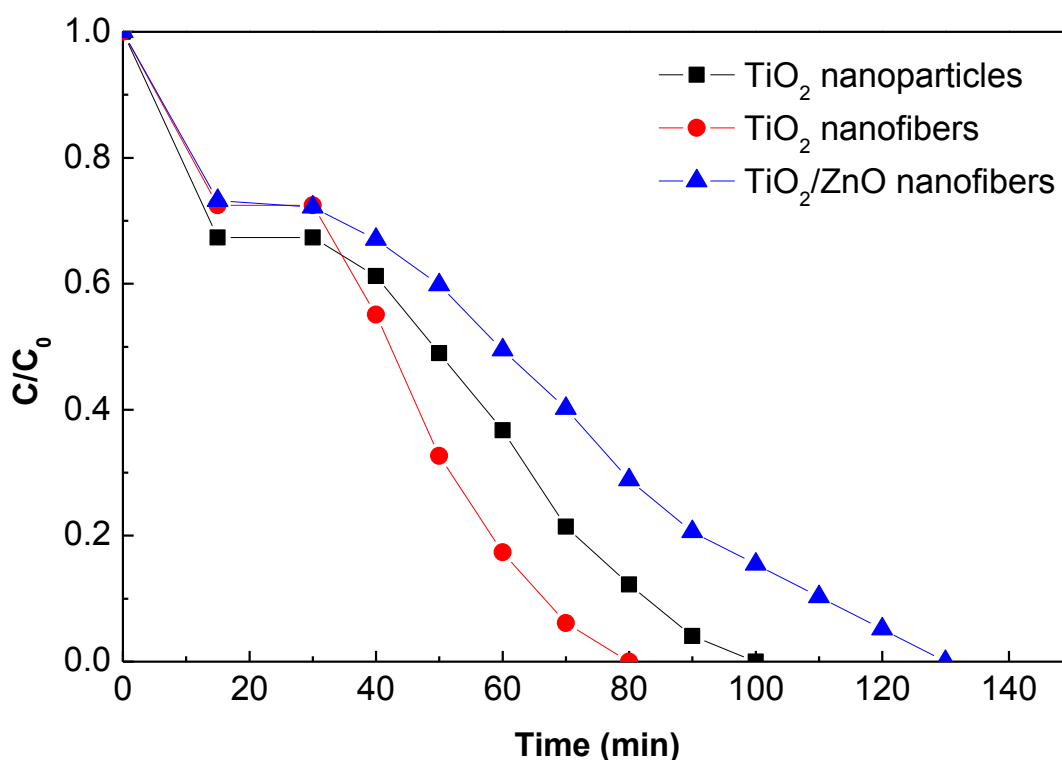


Figure 4.18 Benchmark tests among TiO<sub>2</sub> nanoparticles, TiO<sub>2</sub> nanofibers and TiO<sub>2</sub>/ZnO nanofibers with same catalyst loading of 1g/L under the irradiation of 365 nm UV light.

### 4.3.2 Modeling of reaction kinetics of RhB degradation

During the photocatalytic process, with respect to the results summarized in Figures 7a and 7b, the pseudo first-order reaction rates increased linearly both with catalyst loading (L) at a lower dosage and with light intensity (I), indicating that the reaction rate of RhB photodegradation is a function of the two operating parameters. Therefore, the reaction rate can be defined mathematically by Eqn. 4.1 which further assumes a simplified form in Eqn. 4.2 as follows:

$$k = f(L, I) \quad (4.1)$$

$$k = aL + bI + c \quad (4.2)$$

where L is the loading of TiO<sub>2</sub>/ZnO nanofiber in the reaction unit (g/L) ( $L \leq 2 \text{ g L}^{-1}$ ); I is the light intensity applied (lux); a and b are the coefficients of L and I, respectively; and c is the the intercept (min<sup>-1</sup>).

Eqn. 4.1 and 4.2 are valid when the input of L and I are within the range of the tests. Based on the experimental data, a, b, and c can be solved by multiple regressions and the correlation is given by,

$$R = \left\{ 1 - \exp \left[ (1.5113 \times 10^{-2} L + 1.04 \times 10^{-4} I - 2.137 \times 10^{-2}) t \right] \right\} \times 100\% \quad (4.3)$$

The coefficient of regression ( $r^2$ ) of 0.9718 for Eqn. 4.3 is acceptable. The predicted first order decay based on the model (Eqn. 4.3) can be compared to the experimental data as delineated in Figure 4.19. In general, the predicted reaction rates are quite close to the measurements, and the deviation is less than 10%. For the purpose of system design, the removal percentage of RhB, R (%), can be estimated from Eqn. 4.3

by the two measurable parameters of L and I.

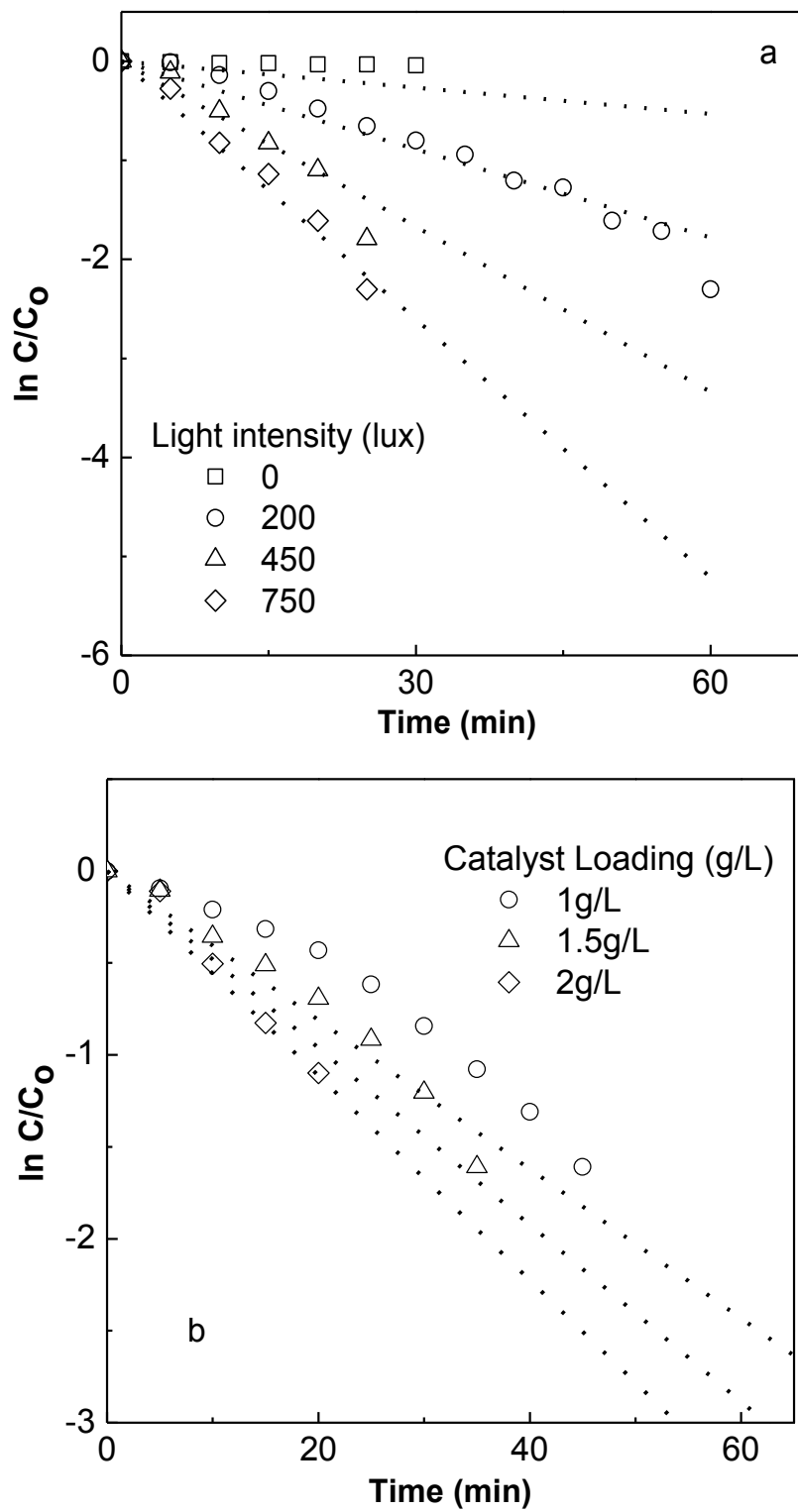


Figure 4.19 Comparison of model and experimental data at (a) different light

intensities (catalyst loading of  $2 \text{ g L}^{-1}$ ) and (b) different catalyst loadings (light intensity of 450 lux). (Note: dot lines were calculated from model and marked data were experimental measurements.)

### 4.3.3 Photocatalytic test on NO

The result of the benchmark tests carried out for  $\text{TiO}_2$  nanofibers (respectively with diameter of 70 nm and 100 nm in the absence of ZnO) and  $\text{TiO}_2$  nanoparticles (with the diameter of 100 nm) under UV irradiation is shown in Figure 4.20. The  $\text{TiO}_2$  nanofibers, with 70 nm and 100 nm diameters, respectively, had 26.5% and 40% efficiency for NO removal, which are much higher than that of the  $\text{TiO}_2$  nanoparticles with only 14% NO removal. Based on previous study (Pei and Leung 2013b), the specific surface area (SSA) of nanofibers with diameter of 80 nm from BET test was  $45 \text{ m}^2/\text{g}$ , while the SSA of 100 nm nanoparticles was around  $40 \text{ m}^2/\text{g}$  (in accordance with the supplier). In essence, the SSA of these two nanostructures was quite comparable. On the other hand, nanofibers are packed with poly-crystallites (see TEM images Figure 4.7) distinctly different from that of the single-crystal nanoparticles. The pores formed between these nano-crystallites can promote the physical adsorption of NO gas molecules thereby increasing the contact between the target gas NO and the surface of catalyst, which is the preliminary step prior to the catalytic reaction. This benefit was more evident when small-diameter nanofibers (i.e. 70-nm  $\text{TiO}_2$  nanofibers comparing with the 100-nm nanofibers) were used, see Figure 4.20.

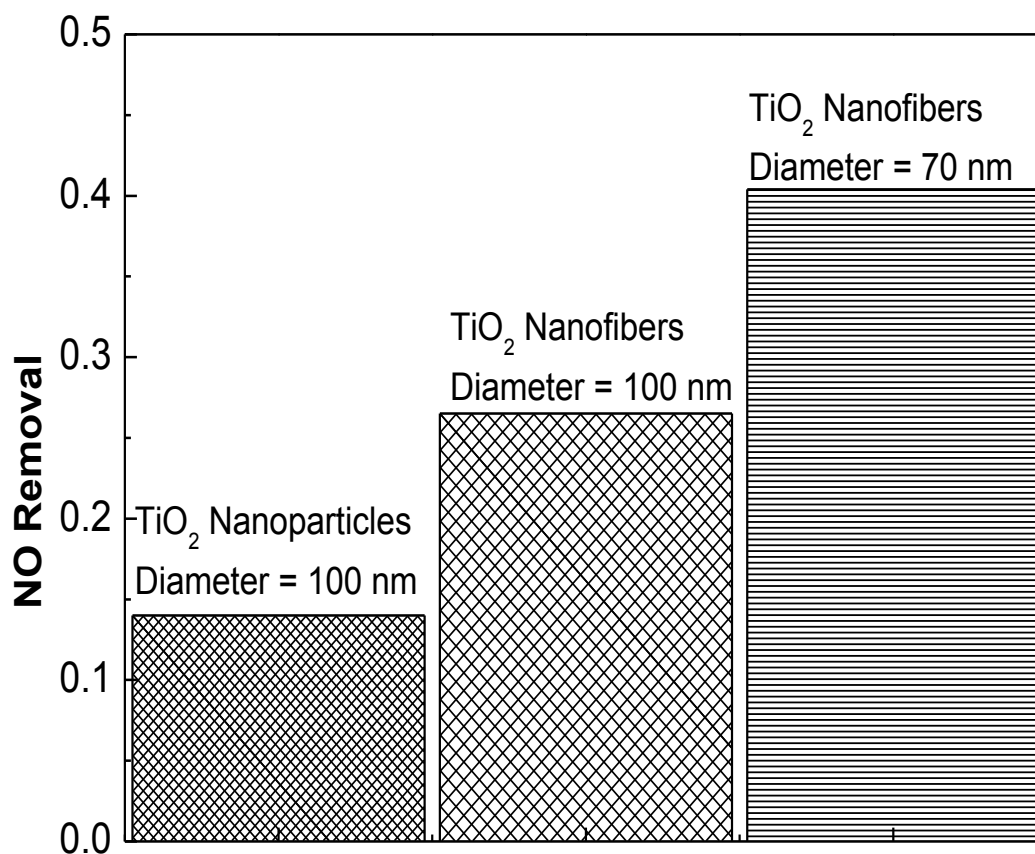


Figure 4.20 Benchmark test of nitrogen oxide removal by three different samples: TiO<sub>2</sub> nanoparticles (Diameter of 100 nm) and TiO<sub>2</sub> nanofibers (Diameter of 100 nm and 70 nm) under UV irradiation.

The concentration of NO decreased rapidly when the light was turned on due to photocatalytic reaction. After initial transient, an equilibrium concentration was ultimately reached where the conversion of NO to NO<sub>2</sub> in presence of oxygen radicals was balanced by the back-reaction where NO<sub>2</sub> was reverted back to NO. The removal of NO was calculated from the difference of initial and final concentration. The plot of NO removal for samples with different concentrations of ZnAc in precursor solution is shown in Figure 4.21. For 3% TIP, TiO<sub>2</sub>/ZnO nanofibers with 0.1 w/w% ZnAc has the best performance with approximately 52% removal of NO; while for 6%

TIP TiO<sub>2</sub>/ZnO nanofibers with 0.3% ZnAc has the best performance with approximately 38% removal of NO. Interestingly, the TiO<sub>2</sub>/ZnO nanofibers prepared with 3% TIP in the precursor solution showed the best performance at 0.1 w/w% ZnAc. The oxygen vacancy functions as a photoexcited electron trapper, thus higher SOV content would express greater photocatalytic activity and higher NO removal. On the other hand, introduction of ZnO in the nanofibers would slightly increase their diameter. The increase in diameter resulted in smaller surface area per unit volume, which decreased the absorbance of NO in the same geometry, with consequence of lower photocatalytic efficiency.

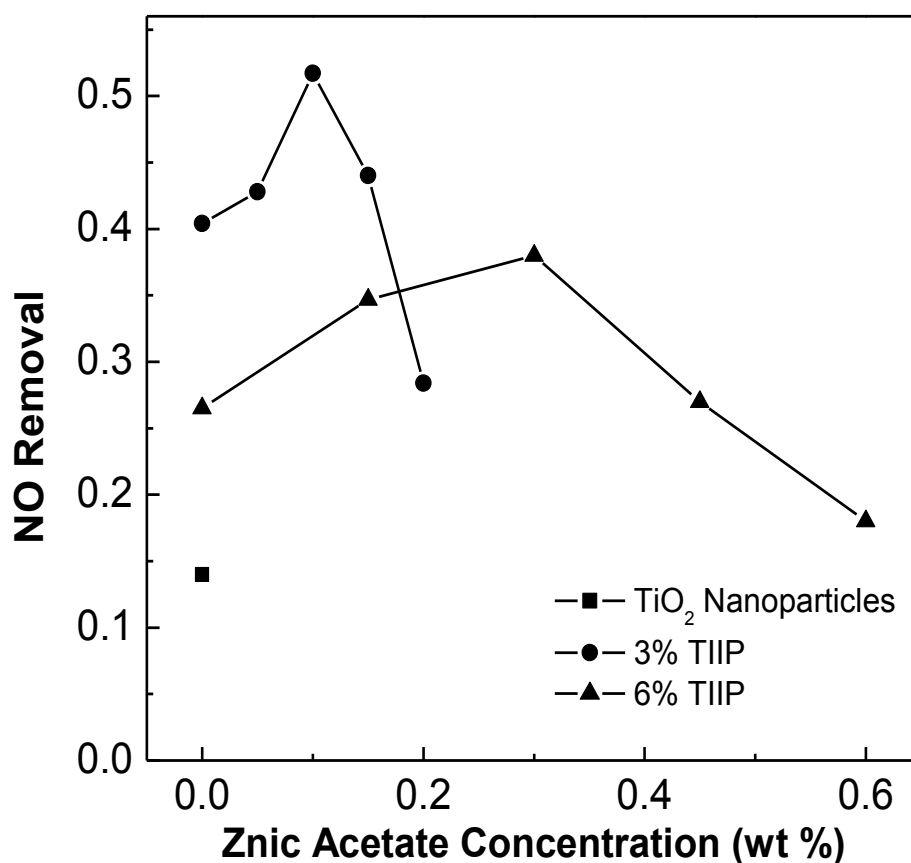


Figure 4.21 Nitrogen oxide removals by nanofibers obtained in the presence of different zinc acetate concentrations in the precursor solution (weight of nanofibers

0.150g, irradiation area  $5.08 \times 1.27 \text{ cm}^2$ , and relative humidity 20%).

After balancing between surface oxygen vacancies, specific surface area, and coating of active sites of the  $\text{TiO}_2$  catalyst by excess ZnO, an optimal ZnAc concentration can be achieved for both TIP concentrations. The distinct difference in performance between the 3% and 6% TIP concentration tests was a result of different nanofiber diameters (70 nm for 3 %TIP and 100 nm for 6% TIP), resulting in different surface areas per unit volume. 3% TIP with larger surface-to-volume ratio was chosen in the following tests for relatively higher NO removal rate.

In the SEM picture, it can be seen that nanofibers were arranged in two dimensional strata or layers. The total thickness of the layers of nanofibers can be controlled by the time of electrospinning under constant condition. Instead of deploying a thick strata/layer, multiple thinner layers (i.e. multilayer) of nanofiber mat samples with the same amount (measured by total weight) of fibers were prepared for photocatalytic reaction. As shown in Figure 4.22, when a fixed total mass of fibers was spread out into, respectively, two times or three times the area under illumination, the photocatalytic efficiency increased due to more light-harvesting (presumably due to better light contact with the fibers, and without shadows being cast from the upper onto the lower layers) from the initial 52% removal efficiency (1 area), 54% (2 areas) to 55% (3 areas). It may also be related to better contact of the pollutant gas with the catalyst given higher porosity and permeability with the multilayer nanofiber configuration versus the more compacted single-layer nanofiber configuration.

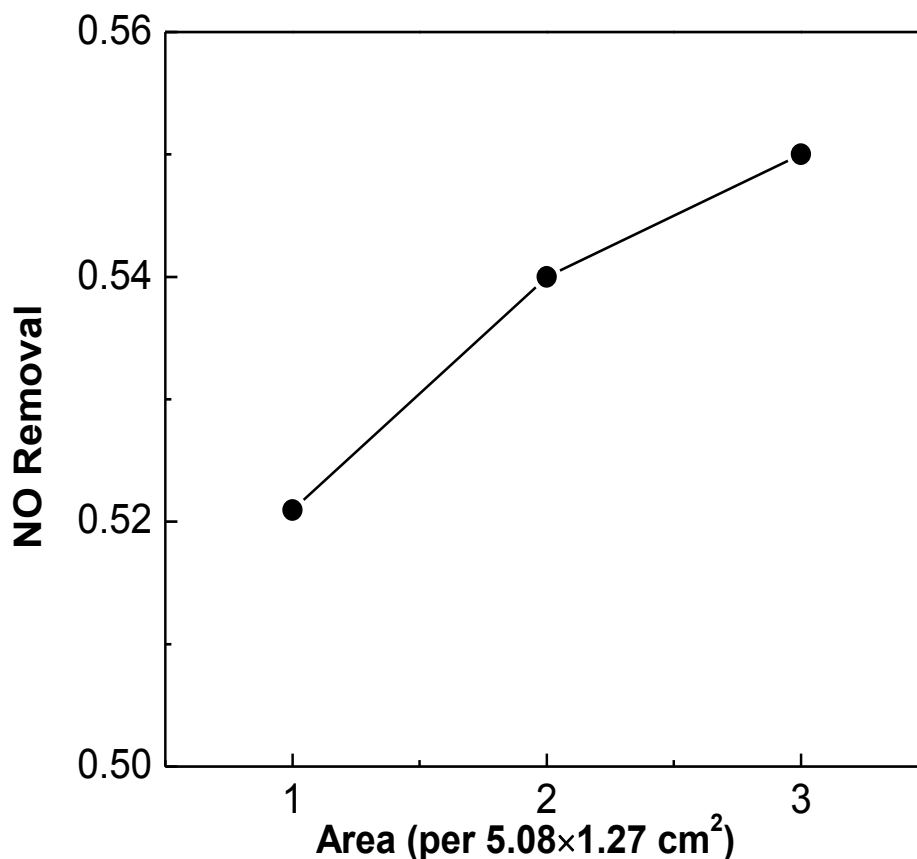


Figure 4.22 Nitrogen oxide removal by nanofiber catalyst with different irradiation area (1 unit of irradiation area is  $5.08 \times 1.27 \text{ cm}^2$ ) (weight of nanofibers 0.150g, relative humidity 20%).

The effect of relative humidity on the photocatalytic efficiency was also investigated. As shown in Figure 4.23, the removal of NO first increased from 40% to 58% as the humidity was raised from 10% to 50%, subsequently it dropped from 58% to 46.2% when the humidity was raised further to 70%.  $\text{TiO}_2$  surface carried both weakly and strongly bound water molecules, as well as hydroxyl groups created by the dissociative chemisorption of water.

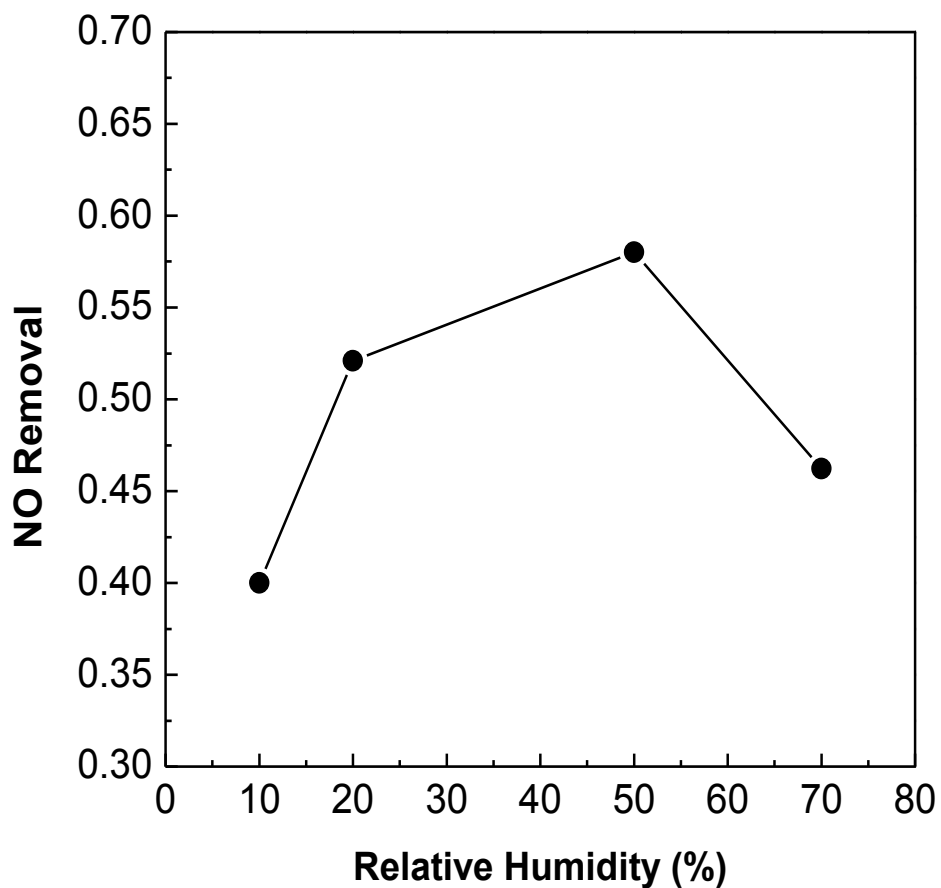


Figure 4.23 Nitrogen oxide removal by nanofiber catalyst under different humidity conditions (25°C, 1 atm,  $\rho_{\omega, \max} = 23.01 \text{ g/m}^3$ ) (weight of nanofibers 0.150g, irradiation area  $5.08 \times 1.27 \text{ cm}^2$ ).

The key mechanisms for the oxidation of NO are summarized below (Laufs et al. 2010, Weiss et al. 2012):





The electron, generated from the incidence of photon, in the conduction-band of TiO<sub>2</sub> reacts with O<sub>2</sub> forming the superoxide anion (O<sub>2</sub><sup>-</sup>). O<sub>2</sub><sup>-</sup> will form ·HO<sub>2</sub> radicals with water vapor in air. The ·HO<sub>2</sub> radicals further react with NO forming NO<sub>2</sub> and a hydroxyl radical. The byproducts can further react to form the end product, nitric acid (HNO<sub>3</sub>). In the absence of water vapor, there is no free hydrogen ions (see Eq. 4.5) and the photocatalytic oxidation of chemical compounds is seriously retarded and the total oxidation to NO<sub>2</sub> cannot take place. On the other hand, excessive water vapor coated on the catalyst surface retards reaction rate because the water molecules occupy the active sites of the reactants. As a result of these two competitive effects, there is a maximum rate of NO removal corresponding to relative humidity at about 50%.

An interesting observation is that the reaction as represented by Eq. 4.6 can be enhanced by increasing the hydroxyl radicals, which means increasing the superoxide anion (O<sub>2</sub><sup>-</sup>) or the SOV. There achieves the latter by increasing the ZnAc content of the catalyst, as demonstrated in Figure 4.21 for both 3% and 6% TIP, respectively, in the precursor solution.

The removal of NO at a relative humidity level of 20% under different residence times was investigated with result depicted in Figure 4.24. It can be seen that NO removal increases with increasing residence time. The longer was the residence time (i.e. lower is the throughflow rate of NO), the longer was the contact time between NO and the photogenerated hydroxyl radicals. At sufficiently long residence time of 9 min, the removal rate was over 80%. In contrast, at residence time of 1.5 min the

removal rate dropped to only 52%. The entire process of photocatalytic oxidation can be thought of as diffusion of reactant gases from the bulk flow to the nanofibers, adsorption of reactant gas molecules onto the active sites of the catalyst, and finally a chemical reaction. The first two (diffusion and adsorption) are physical processes while the last is a chemical process governed by reaction kinetics. Assuming the two physical processes are relatively fast, the rate limiting step is essentially the kinetics of the chemical reaction, Eq. 4.6, for which NO reacts with the hydroxyl radicals to form NO<sub>2</sub>. If the required time for the reaction is of order of several minutes, the retention or residence time has to be at least several minutes in order to provide adequate time for the reaction.

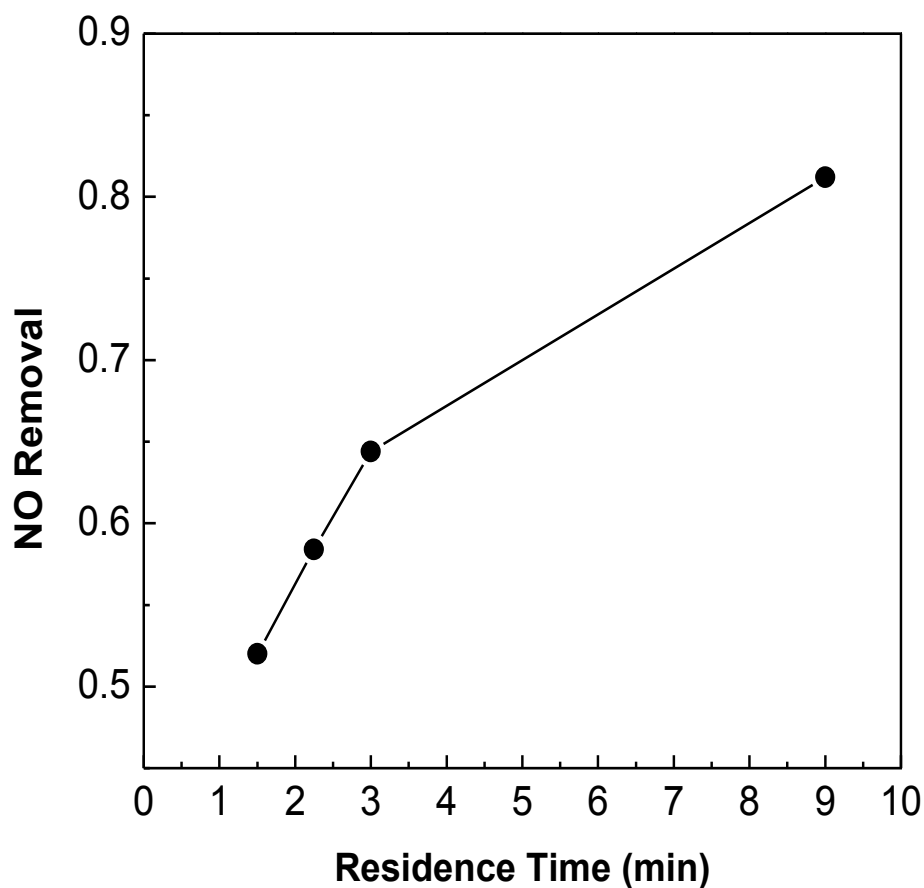


Figure 4.24 Nitrogen oxide removal by nanofiber catalyst for different residence times

(weight of nanofibers 0.150g, irradiation area  $5.08 \times 1.27 \text{ cm}^2$ , and relative humidity 20%).

The nanofibers catalysts can be prepared in mats and attached on the surface of the container to treat the wastewater or contaminated water in batch or semi-batch unit. Due to the nanofibers mats have more contact points than nanoparticles; the problem caused by detaching would be less. Even if the nanofibers mats is detached or broken, because of the high specific gravity of the composite nanofiber, it is easy to recovery by centrifugation. Thus, it is promising for the nanofiber catalysts used in actual applications.

#### **4.4 Summary**

In summary,  $\text{TiO}_2/\text{ZnO}$  nanofibers have been successfully prepared via a nozzle-less electrospinning process and used for photodegradation of RhB dye in suspension. The amount of Zn content is found to play an important role on the photocatalytic activity of the  $\text{TiO}_2/\text{ZnO}$  composite nanofiber. The optimal concentration of ZnAc in the precursor solution is determined to be 0.30 wt. %. This optimum can be interpreted by the dynamics of the competing effects between the specific surface areas and the surface oxygen vacancies. Also, an optimal catalyst loading of  $2 \text{ g L}^{-1}$   $\text{TiO}_2/\text{ZnO}$  has been determined for efficiently removal of the RhB. This balances the increasing active sites in the solution versus increasing opacity and agglomeration with higher catalyst loading. Despite  $\text{TiO}_2$  nanoparticles have larger specific surface area than that of  $\text{TiO}_2/\text{ZnO}$  nanofibers;  $\text{TiO}_2/\text{ZnO}$  nanofibers can achieve a higher photocatalytic reaction rate than that of the former because of the high utilization ratio of light together with the low recombination rate of electron-hole pairs. The present study

demonstrates that the TiO<sub>2</sub>/ZnO composite nanofiber with optimal Zn content is a potential viable photocatalyst in degrading dyes. Nanofibers show much higher photocatalytic oxidation efficiency in the removal of NO than nanoparticles despite they have comparable specific surface areas. Likewise, an optimal relative humidity of 50 % had been found for efficiently removal of the NO as water vapor is needed in the photocatalytic oxidation to generate free radicals for triggering the reaction yet excessive water molecules can occupy and block the active sites preventing NO molecules to be adsorbed onto the catalyst surface. All-in-all, the experimental results in the present study demonstrated that the TiO<sub>2</sub>/ZnO composite nanofiber is a viable photocatalyst in the purification of gas pollutants.

## **Chapter 5**

# **Enhanced Photocatalytic Activity of Electrospun TiO<sub>2</sub>/ZnO Nanofibers with Optimal Anatase/Rutile Ratio**

### **5.1 Overview**

Titanium dioxide is the best known and mostly used photocatalyst due to its relatively low cost, high stability, low toxicity and high photocatalytic efficiency (Carp et al. 2004). Among the three crystal forms of titanium dioxide (anatase, rutile, and brookite), anatase is generally considered to have the highest photocatalytic activity because of its comparatively high density of surface oxygen and low recombination of photogenerated electron-hole pairs (Chorfi et al. 2012). Zinc oxide is another attractive semiconductor oxide having similar photocatalytic property (Lai et al. 2011, Wan et al. 2005). However, both of these two semiconductors can only be excited under UV light as they have a relatively high band-gap energy level (3.2 eV at room temperature). This drawback precludes them in efficiently harvesting solar energy. As such, improving photocatalytic activity by modifying the catalyst has been an active

research area in the past decade. Many investigators have explored various methods, such as doping transition metals (Peill et al. 1997) and non-metals (Livraghi et al. 2009, Martínez-Arias et al. 2012), and forming composite photocatalysts from different semiconductors (Liu et al. 2006), etc., to enhance the photocatalytic activity of TiO<sub>2</sub> and to improve the utilization of visible light. The results reveal that nearly all composite semiconductors have higher photocatalytic activity than a single semiconductor. As seen in Chapter 4 and 5, TiO<sub>2</sub> and ZnO have been combined in a photocatalyst producing synergistic effect in reducing the band gap and improving charge separation. The photocatalytic reaction on degradation of organic dye and oxidation of NO in Chapter 4 and 5 are just some examples demonstrating the benefit. Despite of this, it is possible to further optimize the anatase/rutile crystals fraction in relation to ZnO to reap the most benefit. It would be of great interest to increase the photocatalytic activity by a synthesized photocatalyst composed of zinc oxide, anatase, and rutile, and to study the synergistic role of these three composites in the photocatalyst and performance of the catalyst.

As with previous study, the nanofiber platform will be used to investigate the effect.

Based on the foregoing consideration, a multi-semiconductor (ZnO, anatase and rutile) photocatalyst in form of one-dimensional (1D) nanofibers with enhanced surface area for catalytic activity will be developed in this study. With various characterizations, the synergistic role of these three semiconductors of the catalyst in the photocatalytic reaction will be investigated. The ratio of anatase/rutile in the new catalyst will be optimized for best performance of the photocatalyst by balancing the trade-off of the band-gap energy, the electron/hole recombination rate, and the surface area. Specifically in the present study, a series of TiO<sub>2</sub>/ZnO nanofibers with different

anatase/rutile ratios were successfully synthesized using a sol-gel based nozzle-less electrospinning process followed by calcination treatment at respective different temperatures. All the samples were characterized by X-ray diffraction (XRD), transmission electron microscopy (TEM), UV–Vis diffuse reflectance spectroscopy (DRS), and photoluminescence (PL) spectroscopy. It was found that changing calcination temperature during preparation influenced not only the morphology but also the charge transfer process of TiO<sub>2</sub>/ZnO nanofibers. The photocatalytic activities of the as-prepared samples were investigated by the degradation of Rhodamine B (RhB) and conversion of nitric oxide (NO), respectively. The removal of the dye and pollutant was significant with TiO<sub>2</sub>/ZnO nanofibers calcined at 650 °C. This is due to the relatively smaller grain size and lower electron-hole recombination rate of the nanofibers at 650 °C. Based on the photocatalytic activity on both dye in liquid phase and gaseous pollutant together with a comprehensive characterization of the catalyst, the photocatalytic mechanism of the TiO<sub>2</sub>/ZnO nanofibers was quantified.

## **5.2 Characterizations**

### **5.2.1 XRD analysis**

Figure 5.1 shows the XRD patterns of the as-prepared TiO<sub>2</sub>/ZnO composite nanofibers. TiO<sub>2</sub> exists in two main crystallographic forms, anatase (A) and rutile (R). The XRD intensities of the anatase (A101) and rutile (R110) characteristic peaks have been analyzed. The fraction of anatase-to-rutile transformation in the samples calcined at different temperatures can be calculated from the following equation (Spurr and Myers 1957):

$$x = 1/(1 + 0.8 I_A/I_R) \quad (5.1)$$

$I_A$  and  $I_R$  are respectively the X-ray integrated intensities of the reflection of the anatase (101) and rutile (110).  $x$  is the fraction of rutile in the nanofibers, which for the experiments was calculated to be 0.256, 0.524, 0.716, and 0.926 for samples calcined at 550, 650, 750 and 850 °C, respectively.

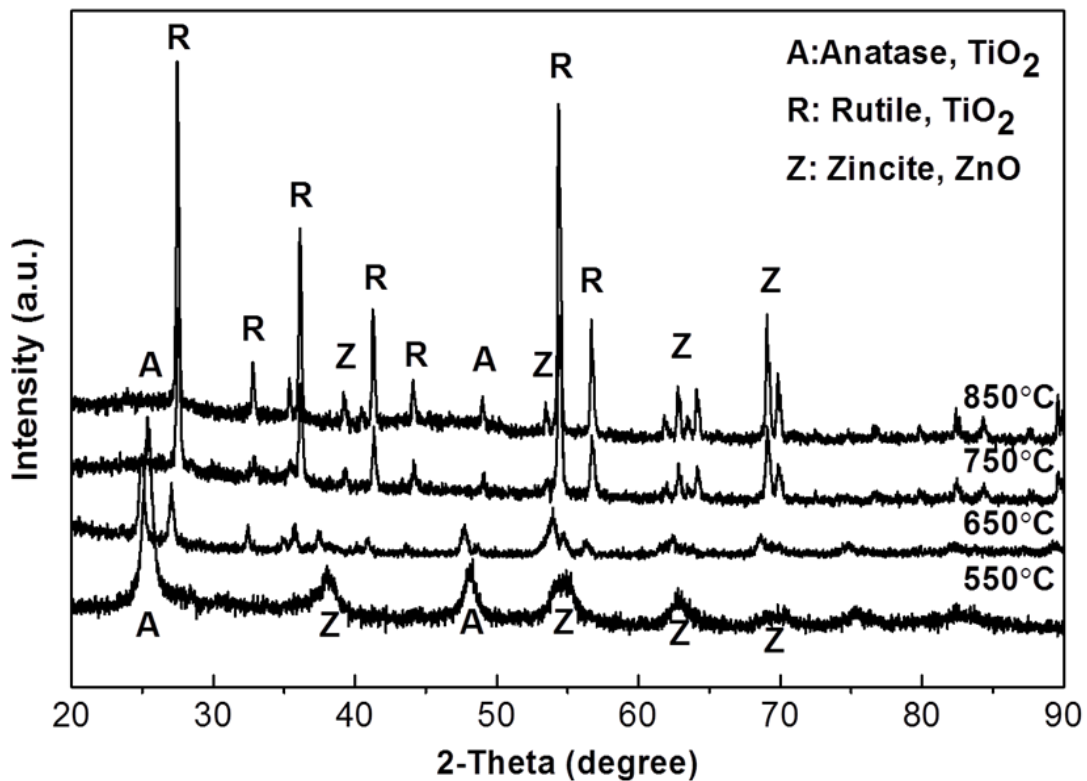


Figure 5.1 XRD patterns of TiO<sub>2</sub>/ZnO composite nanofibers calcined at 550, 650, 750 and 850 °C, respectively.

### 5.2.2 TEM images

The morphology and crystal structure of TiO<sub>2</sub>/ZnO nanofibers were analyzed by TEM and HRTEM. As shown in the TEM images in Figure 5.2 (a-d), the nanofibers were composed of compactly packed nanocrystallites. Given the nanofibers have the

poly-nanocrystal structure, they have large surface-to-volume ratio that favors the photocatalytic reaction when compared with nanoparticles. When the calcination temperatures was raised, the grain size of the nanocrystallites also increased from less than 10 nm to about 150 nm together with the diameters of nanofibers, resulting in a drop in the specific surface area (Vu et al. 2012, Li et al. 2010). Furthermore, the lattice spacing was determined from the HRTEM images (Figure 5.2e and 5.2f representing calcination at 550 °C and 650 °C, respectively) to be 0.35, 0.32 nm and 0.26 nm between adjacent lattice planes of the nanofibers corresponding to the distance between (101) crystal planes of the anatase phase, the distance between (110) crystal planes of the rutile phase, and the distance between (0002) crystal planes of ZnO, respectively.

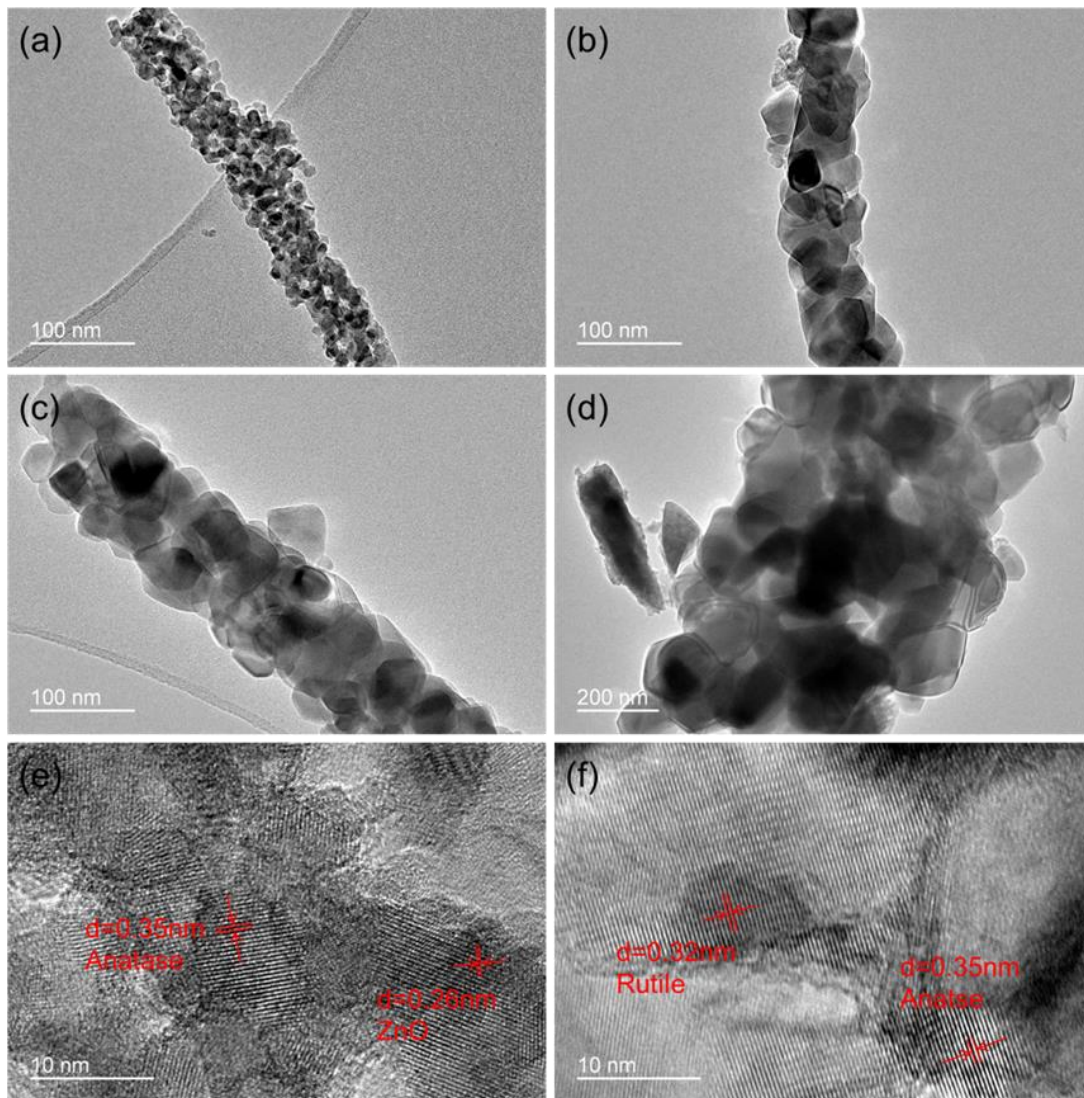


Figure 5.2 TEM images of  $\text{TiO}_2/\text{ZnO}$  nanofibers. (a-d) TEM of  $\text{TiO}_2/\text{ZnO}$  nanofibers calcined at 550 °C, 650 °C, 750 °C and 850 °C, respectively; (e) HRTEM of  $\text{TiO}_2/\text{ZnO}$  nanofibers treated at 550 °C; (f) HRTEM of  $\text{TiO}_2/\text{ZnO}$  nanofibers treated at 650 °C.

### 5.2.3 UV-Vis diffuse reflectance spectra

The UV-Vis diffuse reflectance spectra (DRS) of  $\text{TiO}_2/\text{ZnO}$  nanofibers and  $\text{TiO}_2$  nanofibers were compared in Figure 5.3a. From the absorption spectra between 200 and 800 nm, the absorption edge of  $\text{TiO}_2/\text{ZnO}$  nanofibers was shifted to the visible

spectrum (see insert of Figure 5.3a). The band-gap energies of TiO<sub>2</sub>/ZnO nanofibers calcined at 550, 650, 750 and 850 °C and TiO<sub>2</sub> nanofibers at 550 °C as calculated by the Kubelka-Munk equation were 2.97, 2.96, 2.96, 2.96 and 3.13 eV, respectively. There was very little change in the band-gap energies among the TiO<sub>2</sub>/ZnO as prepared at different calcinations temperatures. However, a decrease in band-gap energy of TiO<sub>2</sub>/ZnO nanofibers as compared to TiO<sub>2</sub> nanofibers can be attributed to the synergistic effect among anatase, rutile, and ZnO. As seen in Fig 5.2(e,f), ZnO dispersed on the surface of TiO<sub>2</sub> involved charge transfer between anatase and rutile due to the difference in their energy-band positions during illumination. Because of the synergetic effect among the conduction bands of these three composites, some sub-bands were formed introducing both impurity and defect levels to the forbidden band of TiO<sub>2</sub> thereby reducing the band-gap energy (Yu et al. 2003, Zhao et al. 2007, Sakthivel et al. 2003).

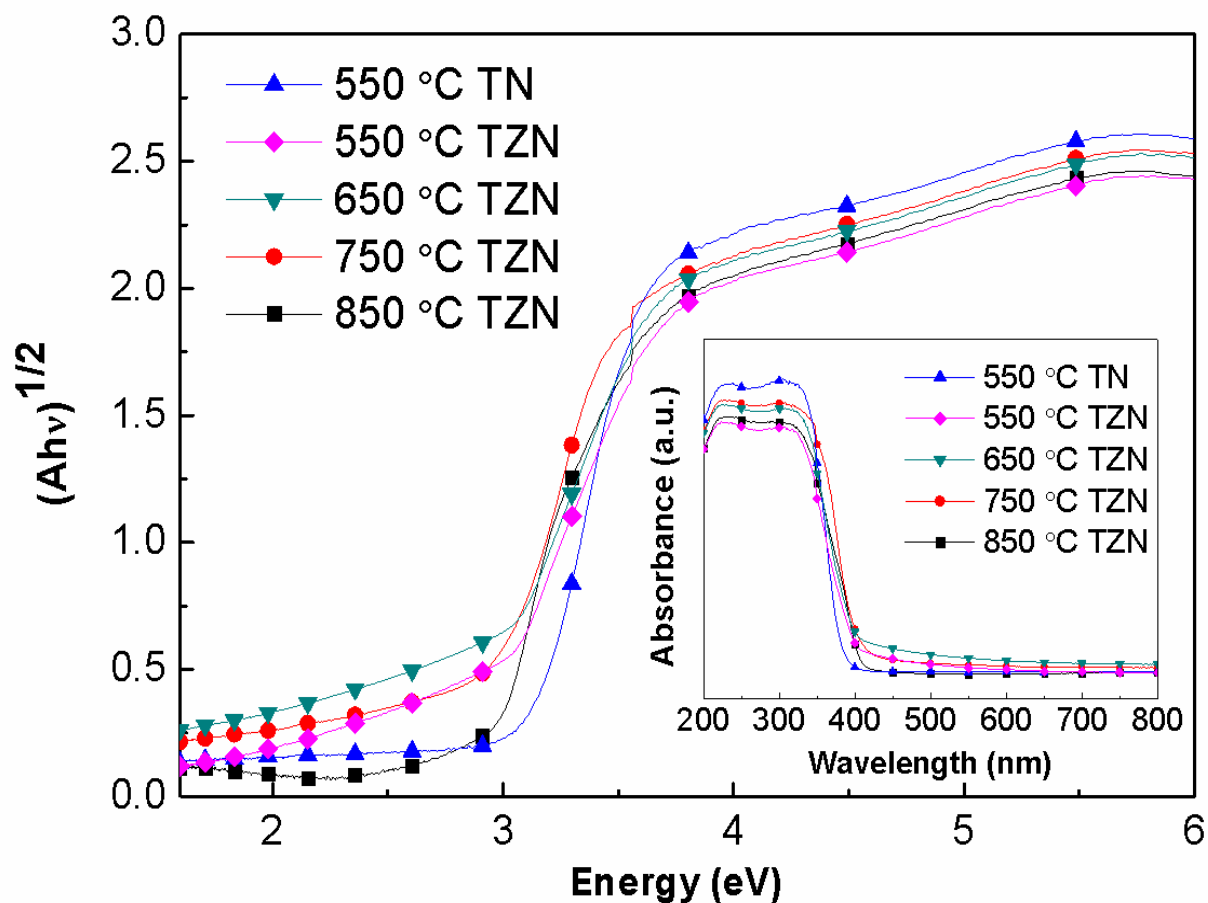


Figure 5.3 The UV-Vis diffuse reflectance spectra of  $\text{TiO}_2/\text{ZnO}$  nanofibers and  $\text{TiO}_2$  nanofibers. The inset shows the absorption spectra between 200 and 800 nm from the transformed Kubelka-Munk function versus the energy of light. (TN:  $\text{TiO}_2$  nanofibers, TZN:  $\text{TiO}_2/\text{ZnO}$  nanofibers).

## 5.2.4 Photoluminescence spectra

Figure 5.4 displays the PL spectra of TiO<sub>2</sub> nanofibers and TiO<sub>2</sub>/ZnO nanofibers under excitation wavelength of 260 nm all measured under room temperature. After ZnO was introduced into the TiO<sub>2</sub> nanofibers, the PL emission peak shifted from 396 nm to approximately 420 nm. The equation for band-gap energy via the PL spectra measurement is given by:

$$E_g = 1240/\lambda \quad (5.2)$$

where  $E_g$  is the band-gap energy (eV) and  $\lambda$  is the wavelength (nm). According to Eq. 5.2, the band-gap energies of the as-prepared nanofibers matched the reported values from the DRS measurement (i.e.  $E_g=3.13$  eV for  $\lambda=395$  nm for TiO<sub>2</sub> nanofiber,  $E_g=2.95$  eV for  $\lambda=420$  nm for TiO<sub>2</sub>/ZnO nanofiber calcined at temperature between 650-850°C). When the calcination temperature was increased, the PL emission intensities first decreased and subsequently increased. Since PL emission intensity was the result of the recombination of photo-excited electrons and holes, lower PL intensity indicated a lower electron-hole recombination rate (Lai et al. 2011). As shown in Figure 5.4, the TiO<sub>2</sub>/ZnO nanofibers heat treated at 650 °C had the lowest PL intensity, thus also the lowest recombination rate of electrons and holes among the four samples prepared at different calcination temperatures, and consequently the highest photocatalytic activity.

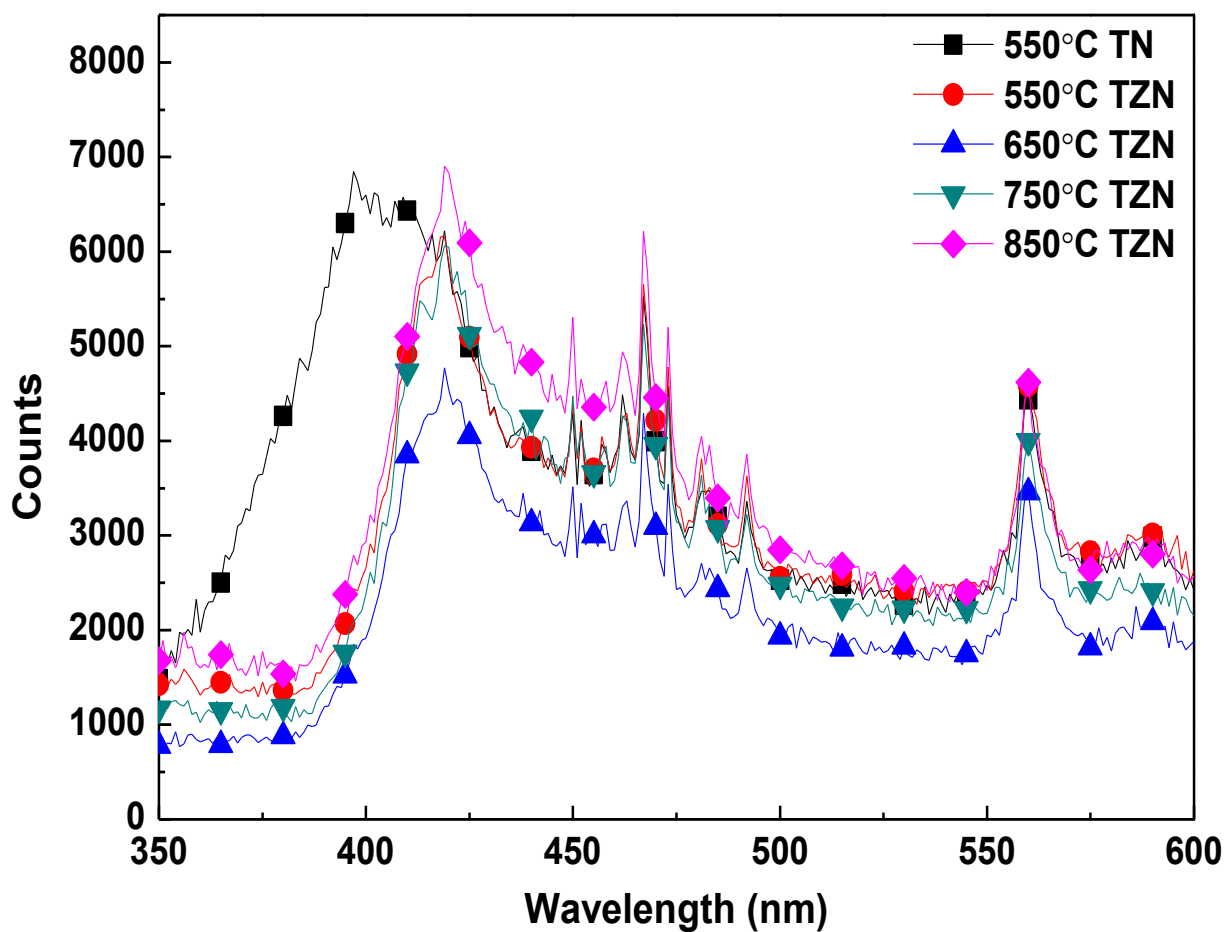


Figure 5.4 The room temperature PL spectra of TiO<sub>2</sub> nanofibers and TiO<sub>2</sub>/ZnO nanofibers under excitation wavelength 260 nm. (TN: TiO<sub>2</sub> nanofibers, TZN: TiO<sub>2</sub>/ZnO nanofibers) (Peaks around 475 nm are generated by the machine noise.)

## 5.3 The photocatalytic activity of TiO<sub>2</sub>/ZnO nanofibers

### 5.3.1 Photocatalytic degradation of RhB in water

The photocatalytic activity of the nanofibers was tested by the decomposition of the Rhodamine B (RhB) dye, which can be considered as a pseudo-first-order reaction (Wan et al. 2005). The time evolution of the concentration of RhB (with absorption peak at 556 nm) under visible-light irradiation (420 nm) as photo-catalytically degraded by TiO<sub>2</sub>/ZnO nanofibers is depicted in Figure 5.5. The drop on the specific surface areas as mentioned in Section 5.2.2 can also be confirmed in the dark condition data ( $t = -30 \sim 0$  min). Nanofibers treated at 500 °C had the best adsorption. When the calcination temperature increased, the adsorption capacities of nanofibers were reduced. The photocatalytic activity of the TiO<sub>2</sub>/ZnO nanofibers has been improved when the calcination temperature of the as-prepared composite nanofibers was increased from 550 to 650 °C. For the case with nanofibers heat treated at 650 °C, RhB was nearly fully degraded after 75 min under visible irradiation. However, further increase in calcination temperature beyond 650 °C on the as-prepared nanofibers lead to deterioration in the photocatalytic activity. The degradation rate constant  $k$  can be calculated from the first-order reaction formula. The relationship between the reaction rate constant and the calcination temperature is shown in the insert of Figure 5.5. The photocatalytic efficiency of the TiO<sub>2</sub>/ZnO nanofibers increased first and decreased subsequently with increasing calcination temperature, and an optimal calcination temperature of 650 °C for preparing the TiO<sub>2</sub>/ZnO nanofibers in the photocatalytic degradation of RhB was confirmed. In general, nanofibers had higher photocatalytic efficiency when compared with commercial P25 nanoparticles.

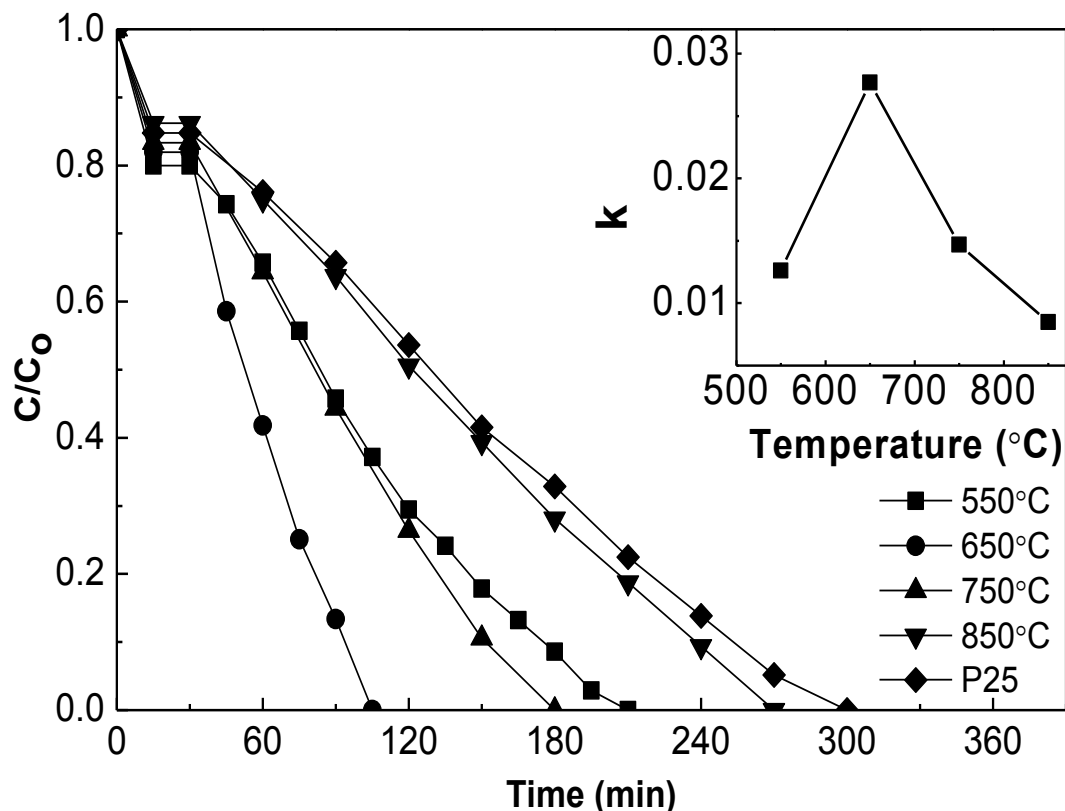


Figure 5.5 The evolution of the concentration of RhB photocatalytic degraded by  $\text{TiO}_2/\text{ZnO}$  nanofibers and P25 nanoparticles under visible light irradiation (420 nm) as a function of time. The insert shows the relationship between the reaction rate constants of photocatalytic degradation of RhB at different calcination temperatures.

### 5.3.2 Photocatalytic oxidation of NO

Figure 5.6 shows the NO removal rate against irradiation time in the presence of different  $\text{TiO}_2/\text{ZnO}$  nanofibers (prepared under different calcination temperatures) and P25 nanoparticles under simulated solar-light irradiation with single-pass flow through the reactor. After 30 min simulated solar-light irradiation, 23%, 34%, 24% and 19% of NO gas was oxidized by the  $\text{TiO}_2/\text{ZnO}$  nanofibers prepared with calcinations temperature at 550, 650, 750 and 850 °C, respectively; and 5 % of NO by

the P25 nanoparticles. Moreover, the NO removal rate increased rapidly in the first 5 min and ultimately reached the highest value of about 20.5% with single-pass for the TiO<sub>2</sub>/ZnO nanofibers calcined at 850 °C. Subsequently, the NO removal rate decreased slowly with the irradiation time, which was ascribed to the accumulation of HNO<sub>3</sub> on the catalyst surface resulting in deactivation of photocatalysts, which was more evident on the performance of the P25 nanoparticles (Nagaveni et al. 2004). In contrast, for the TiO<sub>2</sub>/ZnO nanofibers calcined at 650 °C, the removal rate reached the maximum value after being irradiated for 10 min. Comparing to the TiO<sub>2</sub>/ZnO nanofibers calcined at 850 °C, the TiO<sub>2</sub>/ZnO nanofibers calcined at 650 °C showed superior photocatalytic activity on the degradation of NO at parts per billion levels, which can be explained by the improved surface properties, lower band-gap energy, as well as the reduced electron-hole recombination rate.

As reported, ZnO has the same band-gap energy of the anatase (3.2 eV) of TiO<sub>2</sub>, but the conduction band of ZnO is situated at higher energy than that of the anatase (Chorfi et al. 2012, Ding et al. 2011). As shown in Figure 5.7, the photogenerated electron in the conduction band of ZnO may jump to the conduction band of TiO<sub>2</sub>. Likewise, the valence band of anatase is of lower energy than that of ZnO. This may lead to the hole-transfer from the valence band of anatase to the valence band of ZnO. Similarly, the rutile structure of TiO<sub>2</sub> has lower conduction band (0.2 eV) energy than that of the anatase structure (Karunakaran et al. 2011, Tsukamoto et al. 2012). The electron-hole pair transfer also occurs between anatase and rutile. Meanwhile, due to the difference in the energy band positions, there exists a synergetic relationship between ZnO, anatase and rutile to reduce the overall band-gap energy. Under irradiation, the electrons and holes are generated on the anatase surface. The generated electrons can jump from anatase to rutile, while the holes transfer from anatase to

ZnO. These coupled mechanisms among the three semiconductors can decrease the recombination rate of electrons and holes, thereby increasing the lifetime of the electron-hole pairs for the photocatalytic reaction. Thus, the photocatalytic activity of TiO<sub>2</sub>/ZnO nanofibers was improved in these tests. Also, high calcination temperature was found not to be beneficial to the photocatalytic activity because at high rutile-to-anatase ratio the abundant rutile became the new center of recombination (Carp et al. 2004). Concurrently, the surface area and thus the photocatalytic activity were reduced due to the increase in grain sizes. Thus, a balance between reducing recombination versus reducing surface area from the increasing grain size by increasing the rutile ratio lead to an optimal anatase/rutile ratio (48:52) with nanofibers calcined at 650 °C for which photocatalytic activity of TiO<sub>2</sub>/ZnO nanofibers was maximized.

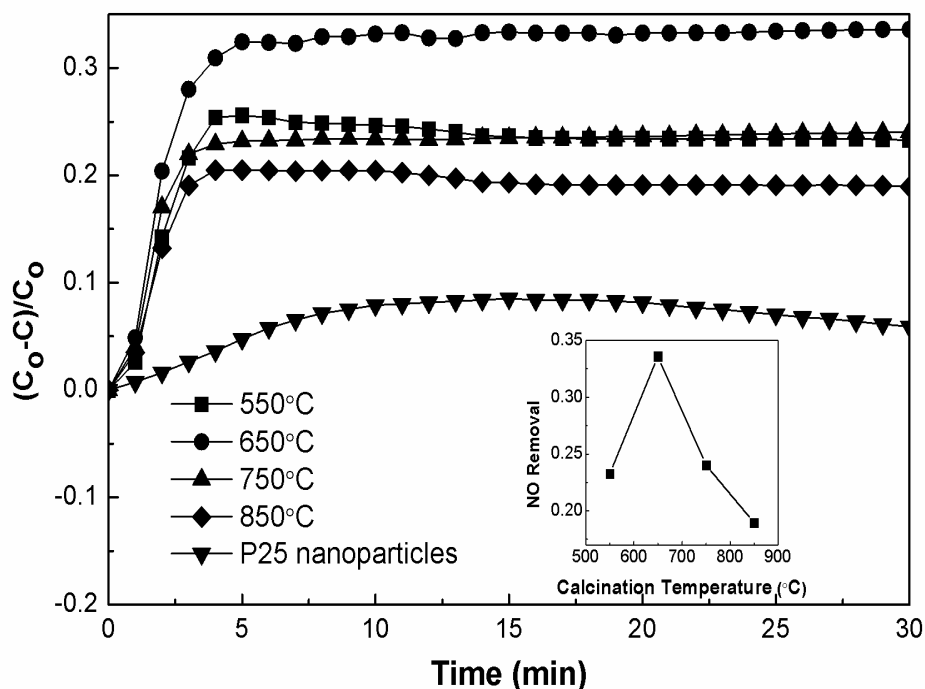


Figure 5.6 The relative variations of the NO removal against irradiation time in the presence of TiO<sub>2</sub>/ZnO nanofibers calcined at different temperatures together with P25

nanoparticles. Inset shows the relationship between the reaction rate constants of photocatalytic oxidation of NO and the calcination temperatures.

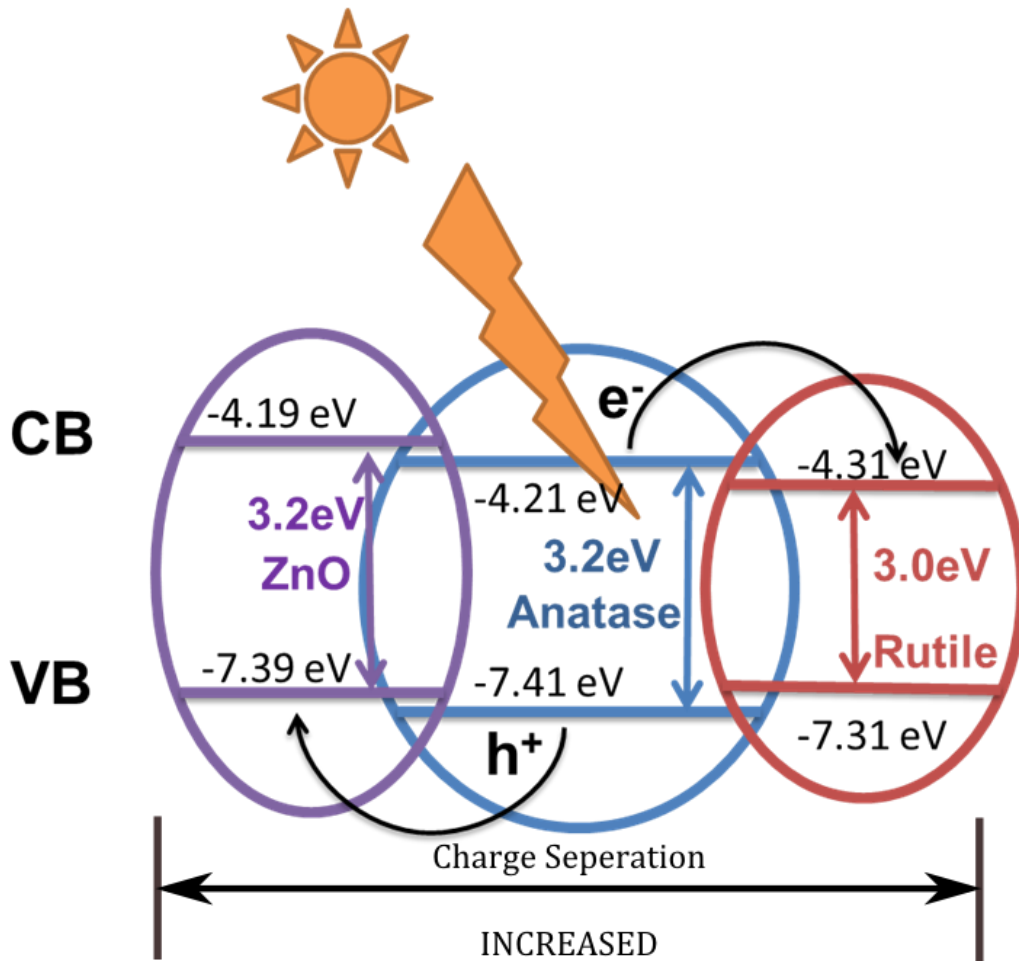


Figure 5.7 Proposed schematic illustration of the photocatalytic mechanism of TiO<sub>2</sub>/ZnO nanofibers.

## 5.4 Summary

The TiO<sub>2</sub>/ZnO nanofibers have been fabricated via nozzle-less electrospinning followed by calcination at various temperatures. XRD analysis reveals that the nanofibers are composed of ZnO, anatase and rutile with different anatase/rutile ratio when treated at different calcinating temperatures. The optimal combination of these three semiconductors can (a) reduce the band-gap energy when compared with TiO<sub>2</sub> nanofibers alone and (b) enhance charge separation on photo-excitation, thus reducing electron-hole recombination, thereby increase photocatalytic activity. Meanwhile, the grain size of the nanocrystallites making up the nanofibers also increases as the temperature is increased resulting in less surface area for photocatalytic reaction. Balancing these trade-off effects lead to the highest photocatalytic efficiency for the optimal TiO<sub>2</sub>/ZnO nanofibers prepared with calcination temperature of 650 °C.

## Chapter 6

# Fabrication and Photocatalytic Activity of TiO<sub>2</sub>/ZnO/Bi<sub>2</sub>O<sub>3</sub> Nanofibers:

### 6.1 Overview

Numerous efforts have been made to develop highly effective photocatalysts for pollutant treatment. As the most studied photocatalyst, titanium dioxide suffers the low sunlight responsive which retards its widely usage in industry. Thus, designing, fabricating, and tailoring the physicochemical and optical properties of titanium dioxide is indispensable to utilize a large fraction of the solar spectrum.

In the number of approaches, formation of semiconductor heterojunction structures is an effective way to enhance the photogenerated electron/hole separation efficiency and the photocatalytic performance. The vectorial charge transfer from one semiconductor to another with suitable band edge positions that is thermodynamically favorable can increase the lifetime of the charge carriers thus promoting the interfacial charge transfer and catalytic efficiency. To further increase the photocatalytic performance of the previous TiO<sub>2</sub>/ZnO composite nanofibers, to fabricate TiO<sub>2</sub> composite with narrow band gap semiconductors is valid to produce visible light responsive photocatalysts.

Among various narrow band gap semiconductors such as CdS, WO<sub>3</sub> and Fe<sub>2</sub>O<sub>3</sub>, Bi<sub>2</sub>O<sub>3</sub> has been widely investigated for its small band gap (2.8 eV). Bi<sub>2</sub>O<sub>3</sub> has proved to be an efficient photocatalyst under visible light irradiation. The intrinsic polarizability induced by the Bi 6s<sup>2</sup> lone pairs of electron is helpful for the separation of the photogenerated electron–hole pairs and the transfer of the charge carriers. Previously there are some results on the heterostructured photocatalysts, such as TiO<sub>2</sub>/Bi<sub>2</sub>O<sub>3</sub>(Bian et al. 2008, Zhao et al. 2012) and ZnO/Bi<sub>2</sub>O<sub>3</sub>(Balachandran and Swaminathan 2012). Bi<sub>2</sub>O<sub>3</sub>/TiO<sub>2</sub> composite photocatalyst can be easily activated by visible light owing to the photosensitization by Bi<sub>2</sub>O<sub>3</sub>. Since the valence band of Bi<sub>2</sub>O<sub>3</sub> is lower than that of TiO<sub>2</sub>, the Bi<sub>2</sub>O<sub>3</sub>/TiO<sub>2</sub> heterojunctions are formed in the composite, which promote the photo-generated holes in Bi<sub>2</sub>O<sub>3</sub> to be transferred to the upper lying valence bands of TiO<sub>2</sub>. Consequently, the valence band holes and hydroxyl radicals produced via oxidation of adsorbed H<sub>2</sub>O or HO<sup>-</sup> can degrade organic dyes with Bi<sub>2</sub>O<sub>3</sub>/ TiO<sub>2</sub> composite nanoparticles under visible light irradiation (Bian et al. 2008). Swaminathan et al. (Balachandran and Swaminathan 2012) have also studied the heterostructured Bi<sub>2</sub>O<sub>3</sub>/ZnO, which has increased UV absorption when compared with ZnO. The enhanced photocatalytic activity of Bi<sub>2</sub>O<sub>3</sub>/ZnO is attributed to the low recombination rates of photoinduced electron–hole pairs, caused by the transfer of electrons and holes between ZnO and Bi<sub>2</sub>O<sub>3</sub>.

Therefore, in this study, TiO<sub>2</sub>/ZnO/Bi<sub>2</sub>O<sub>3</sub> composite nanofibers are fabricated through electrospinning and the photocatalytic efficiency is tested on the oxidation of nitrogen monoxide. In addition, a novel kinetic model using fluid mechanics approach is applied to illustrate the behavior of the photocatalytic reaction.

## 6.2 Characterization of TiO<sub>2</sub>/ZnO/Bi<sub>2</sub>O<sub>3</sub> composite nanofibers

### 6.2.1 Thermal Behavior of the as-spun fibers

The TGA-DSC curve is shown in Figure 6.1. It shows that both the TGA and DSC are stable after 600 °C, which indicates all the organic compounds are gone after 600 °C. Thus, the calcination temperature of these composite nanofibers was determined to be 650 °C.

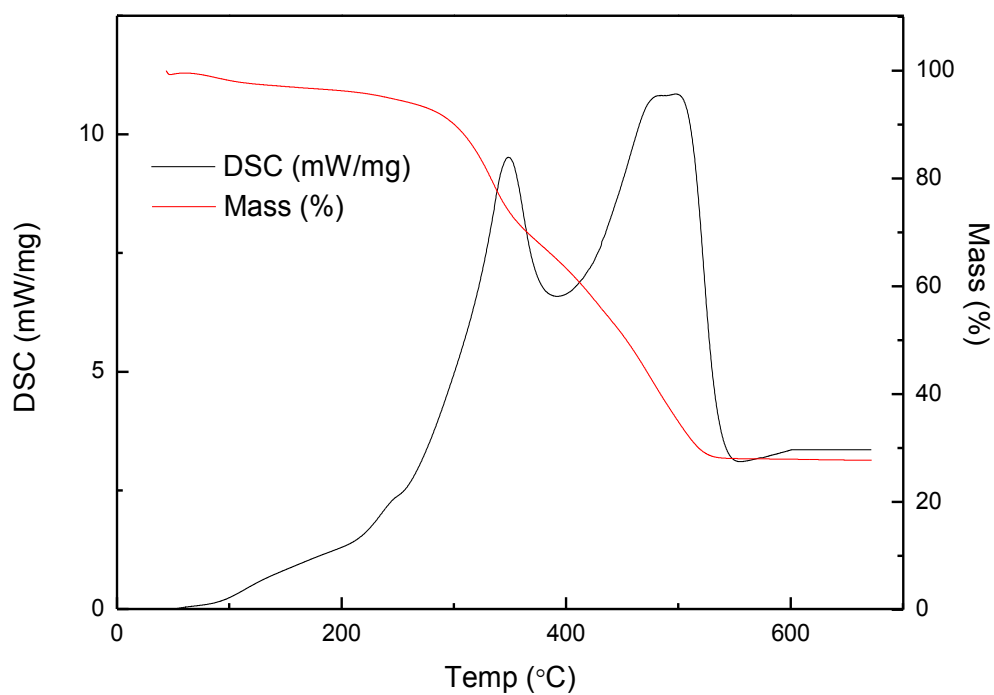


Figure 6.1 TGA-DSC curve of the as spun fibers.

## 6.2.2 Morphology of the fibers

The morphology of the nanofibers is analyzed by SEM and TEM. The SEM picture shown in Figure 6.2 presented the fiber with different Bi concentration (0.1%, 0.2%, 0.3% and 0.4% in a, b, c d, respectively) in the precursor solution after calcination. Fine fibers are distributed in layers randomly. When the Bi concentrations are 0.1% and 0.2%, the fibers are smooth and even. When raise the Bi concentration to 0.3% and 0.4%, there form some branch-like nanofibers, which is due to the differences in the coefficients of thermal expansion among these three semiconductors. The coefficients of thermal expansion of  $\text{TiO}_2$ ,  $\text{ZnO}$ , and  $\text{Bi}_2\text{O}_3$  are  $9 \times 10^{-6} \text{ K}^{-1}$ ,  $4.75 \times 10^{-6} \text{ K}^{-1}$ , and  $18 \times 10^{-6} \text{ K}^{-1}$ , respectively (Yashima et al. 2005, Madhavan et al. 2013). Under a higher bismuth concentration, the composite fibers are broken up into short rods because of sharp thermal shock and shrinkage in the initial stage. When the temperature exceeds the softening point of PVP, these short rods will shrink. At higher temperature, all rods begin to melt partly or fully and then bond mutually to form branch-like fibers (Lommens et al. 2005, Du et al. 2013). The average diameter of the fibers is around 90 nm, which agrees with the TEM picture shown in Figure 6.3c. The TEM pictures also reveal the internal structure of the composite nanofibers, which are piled up of the nanocrystals. This kind of structure will provide some nanoholes in between, thus is favorable for the photocatalytic reaction. The EDS test points out the existence of Ti, Zn and Bi, and the HRTEM displays the lattice spacing of 3.52 Å, 2.81 Å, and 3.31 Å, which are corresponding to the crystal structure of anatase, zincite and bismuth oxide, respectively.

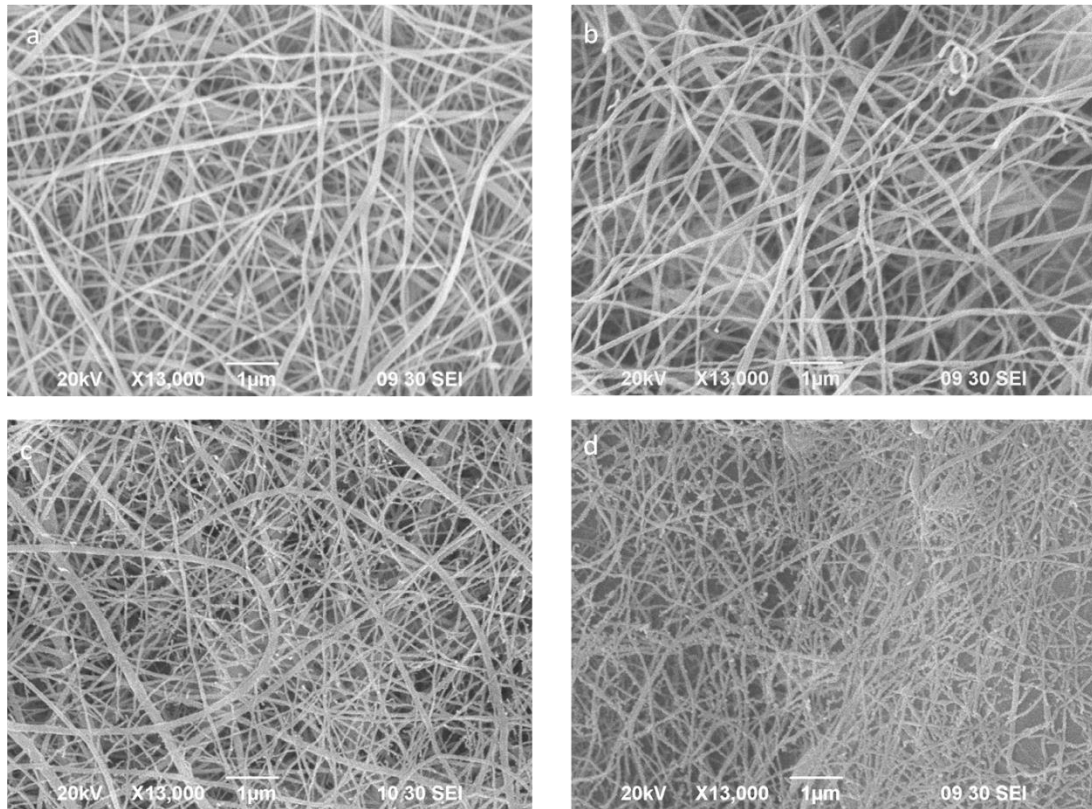


Figure 6.2 SEM images of TZB nanofibers after calcination with different bismuth (III) nitrate pentahydrate concentrations in precursor solutions: a. 0.1%; b. 0.2%; c. 0.3%; d. 0.4%.

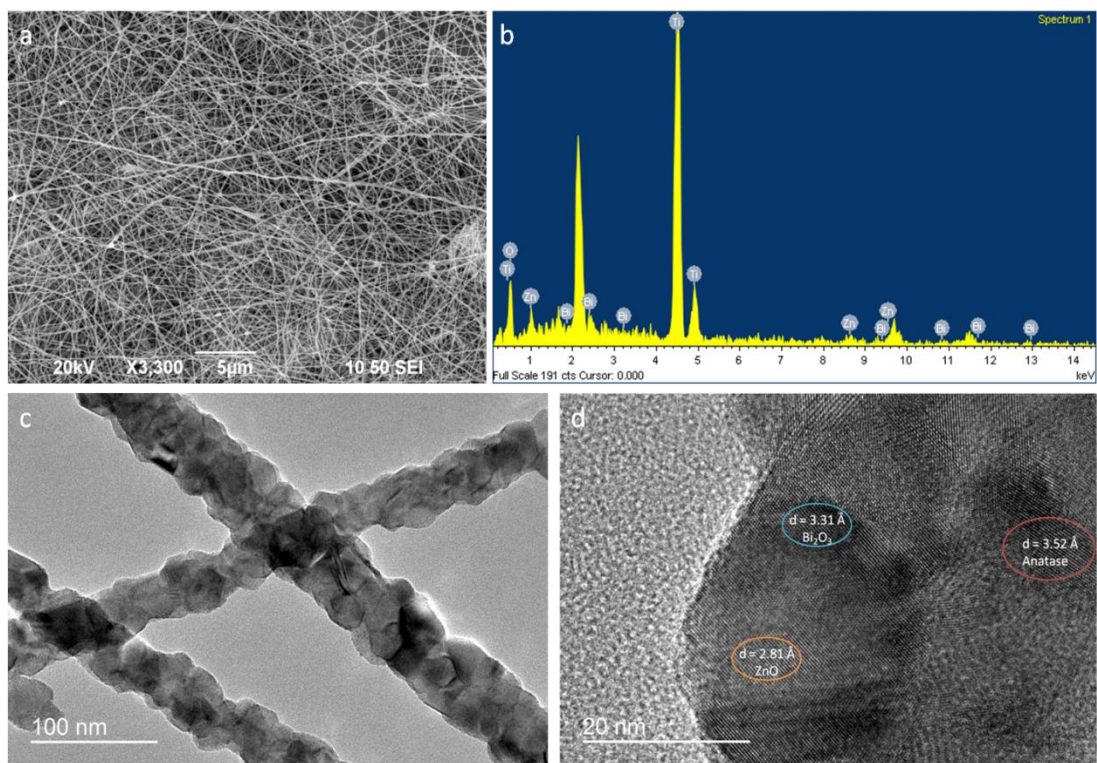


Figure 6.3 a SEM picture of the fibers after calcination; b EDS test result of the location shown in a; c TEM image of the prepared nanofibers; d HRTEM image of the fibers.



#### 6.2.4 UV-visible absorption and reflectance spectra

The diffuse reflectance UV-Vis spectra of both TZB nanofibers and commercial TiO<sub>2</sub> nanoparticles were compared in Figure 6.5. From the absorption spectra between 200 and 700 nm, the absorption edge of TZB nanofibers has been shifted to the visible region. The result shows that the absorbance in the UV range can be significantly improved, and part of the visible range can be also utilized. The steep shape of the spectra is characteristic of a band gap transition and cannot be attributed to the transition from the impurity level.

Using the Kubelka-Munk equation, the band gap of TZB nanofibers with Bi concentration 0.1%, 0.2%, 0.3% and 0.4% together with TiO<sub>2</sub> nanoparticles were determined to be 2.74 eV, 2.51 eV, 2.81 eV, 2.85 eV and 3.12 eV, respectively. The decrease in band gap energy of TZB nanofibers as compared to TiO<sub>2</sub> nanoparticles can be attributed to the synergistic effect among anatase, rutile, ZnO, and Bi<sub>2</sub>O<sub>3</sub>. As seen in Fig 6.3d, ZnO and Bi<sub>2</sub>O<sub>3</sub> dispersed on the surface of TiO<sub>2</sub> involved charge transfer between anatase and rutile due to the difference in their energy band positions during illumination (see Figure 6.6). The TZB has an interesting energy diagram as shown which favors movement of electron and holes which facilitate generation of radicals with the vapor in air producing both oxygen and hydroxyl radicals.

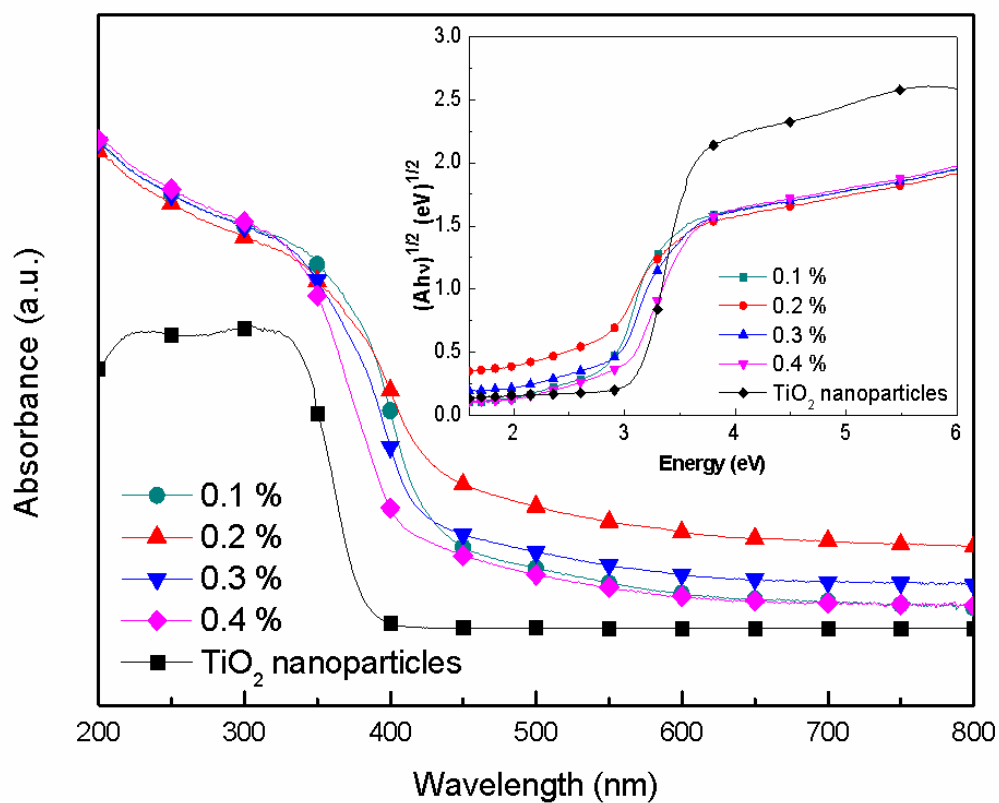


Figure 6.5 The UV-Vis absorption spectra of TZB and commercial  $\text{TiO}_2$  nanoparticles between 200 and 800 nm. The insert shows the UV-Vis diffuse reflectance spectra of from the Kubelka-Munk function versus the energy of light.

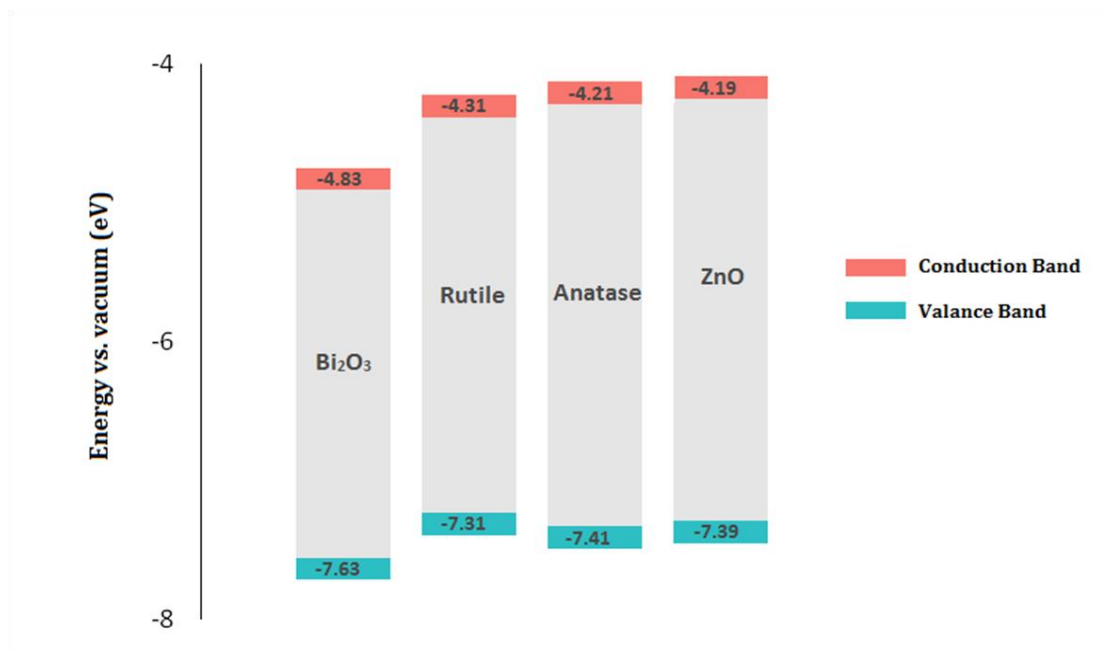


Figure 6.6 Energy diagram of the composite TZB photocatalyst.

## 6.2.5 Electrochemical impedance spectra

As shown in Figure 6.7, the typical electrochemical impedance spectra are present as Nyquist plots, and it is observed that, under dark condition, electrons transfer from conductive substrates (FTO glass) to the TZB film, and then diffuse through the film to the counter electrode. During the process of transmission, the electrons will be recombined in the electrolyte. The recombination process is the main reaction of the interface under the dark state, which is detrimental for the photocatalytic process, thus the impedance is the bigger the better in dark condition. While in the illumination case, the semicircle in the plot varies with different Bi concentrations. The 0.2% has the shortest semicircle, which indicated the lowest in the solid state interface layer resistance and the charge transfer resistance on the surface (Adachi et al. 2011, Hao et al. 2011, Tsao et al. 2011). Overall, both the electron accepting and transporting

properties of 0.2% Bi nanofibers in the composite can contribute to the suppression of charge recombination, and thereby a higher rate in the photocatalysis would be achieved.

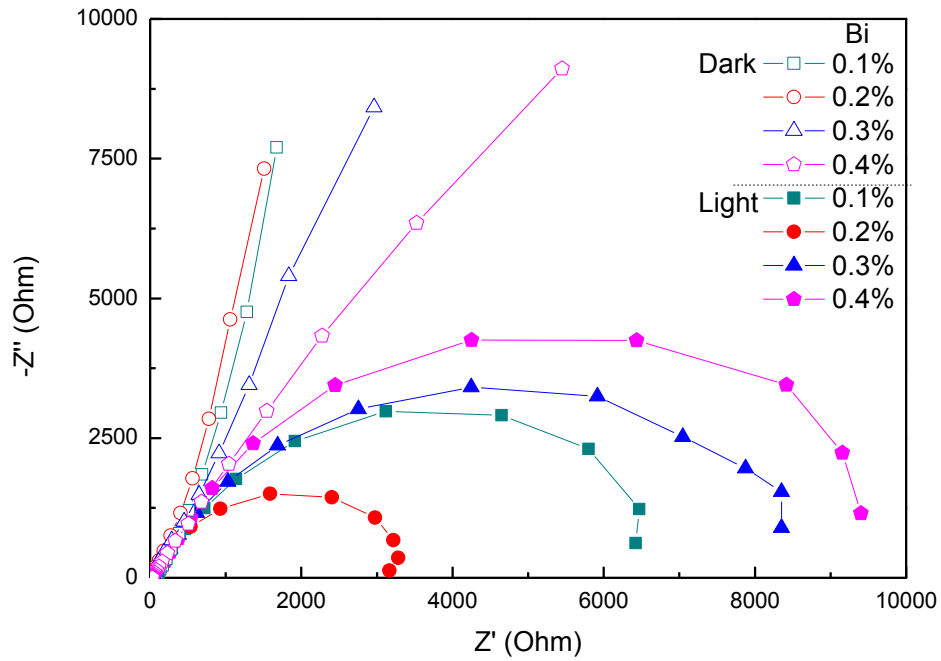


Figure 6.7 EIS changes of TZB nanofibers films with different bismuth (III) nitrate pentahydrate concentrations in dark/light conditions.

## 6.3 Photocatalytic efficiency on the conversion of nitrogen monoxide

Figure 6.8 shows the NO removal rate against irradiation time in the presence of different TZB nanofibers (prepared under different bismuth (III) nitrate pentahydrate) and P25 TiO<sub>2</sub> nanoparticles under simulated solar-light irradiation with single-pass flow through the reactor. After 30 min simulated solar-light irradiation, 37.5%, 67.2%, 20.5% and 17.1% of NO gas was oxidized by the TZB nanofibers prepared with Bi concentration of 0.1%, 0.2%, 0.3% and 0.4%, respectively; and 8.5% of P25 nanoparticles. Moreover, the NO removal rate increased rapidly in the first 5 min and ultimately reached the highest value and maintain for at least 30 min of TZB nanofibers. For the TiO<sub>2</sub> nanoparticles, however, the highest NO conversion 8.5% was achieved at around 15 min and then decreased slowly with the irradiation time to 6% at 30 min, which was ascribed to the accumulation of HNO<sub>3</sub> on the particles surface resulting in deactivation of photocatalysts. In general, the 0.2% TZB composite nanofibers held the highest photocatalytic efficiency on the conversion of NO which can be explained by the highest solar light utilization, lowest band-gap energy, as well as the lowest electron–hole recombination rate.

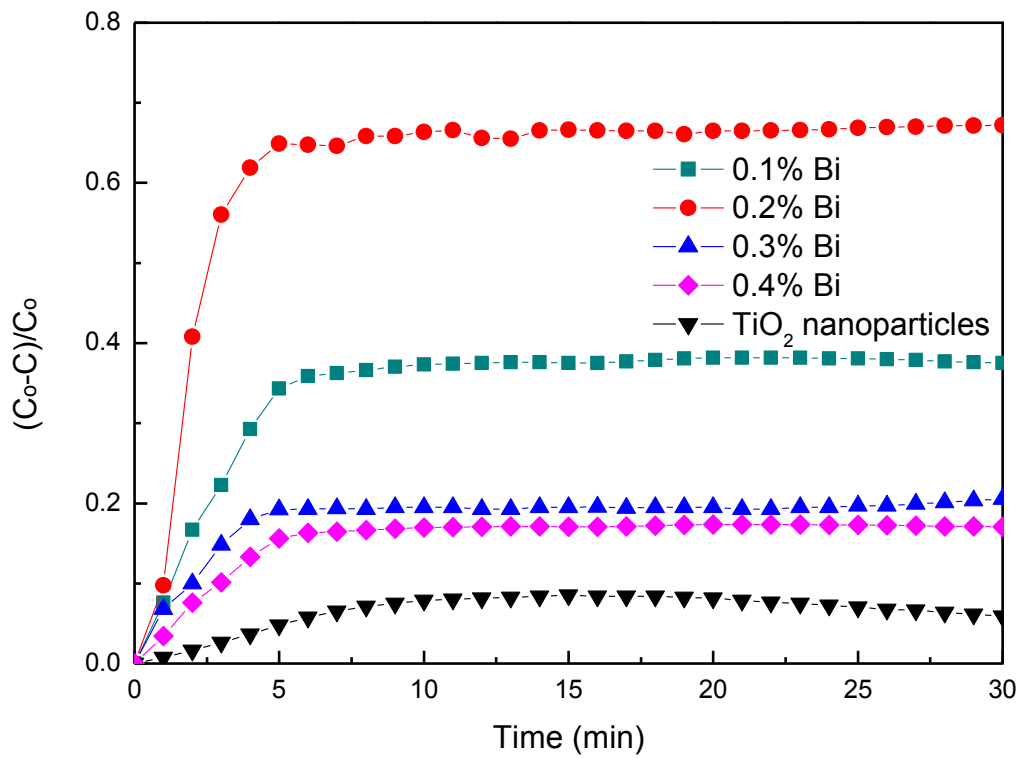


Figure 6.8 The relative variations of the NO removal against irradiation time in the presence of TZB nanofibers prepared with different Bi concentrations together with P25 nanoparticles.

## 6.4 Kinetic model

In this part, a new kinetic model is proposed by Prof. Leung to explain the behavior of experimental data. In essence there are two time scales, one corresponding to the flow retention time  $t_R$ , i.e. time for which the pollutant gas stays on average in the "box reactor"; and the other time scale corresponding to the time frame for which physical/chemical process(es) take place in the reactor. For the latter, it is assumed that some time  $\tau$  is required to realize the maximum pollutants conversion, or maximum sink capacity of pollutants. The typical time of the limiting process (physical/chemical) is assumed to be of order of this time scale  $\tau$ . These two time-scales  $t_R$  and  $\tau$  interact in a complicated way dictating the final outcome.

Kinetic time constant:

The time-limiting kinetics (or time to realize the maximum photo-oxidation capacity, i.e. sink capacity) can be attributed to:

- (a) Physical diffusion of pollutant gas and water vapor into the pores of the catalyst,
- (b) Adsorption of pollutant gas and water vapor onto the reactive site of the catalyst,  
and
- (c) The chemical reaction due to generation of the oxygen and hydroxyl radicals, valence band holes, and the chain of chemical reactions of these radicals and holes with the pollutant gas converting it ultimately to harmless substances.

It is possible that the above three mechanisms may be limiting at various times during the reaction for which multiple time constants apply at various stages rather than

having only one time constant being the dominant (i.e. longest time) for the entire process. This will be apparent later as  $\tau$  is an assumed value in the model and it is determined from matching the experimental result with the model based on an assumed  $\tau$ .

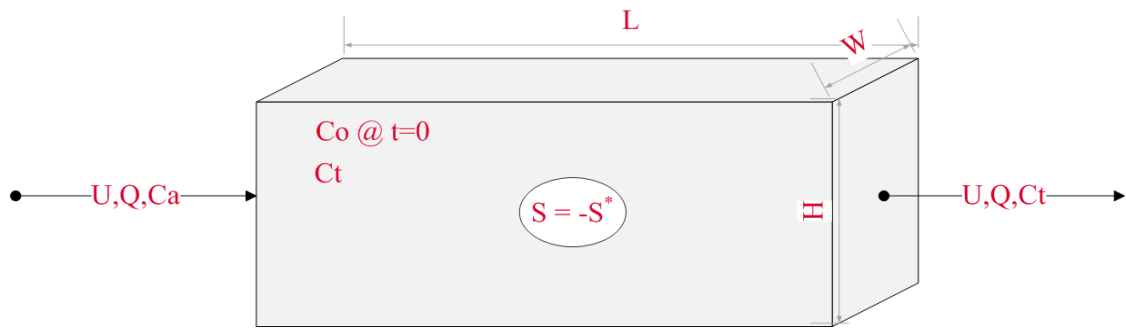


Figure 6.9 Box model with physical/chemical process controlling the kinetics.

From Figure 6.9, it can be written

$$LA \frac{dC}{dt} = AU(C_a - C) - S^* \tanh(t/\tau)$$

where

$$\tanh(t/\tau) = \frac{1 - \exp(-2t/\tau)}{1 + \exp(-2t/\tau)} \quad (6.1a, b)$$

Eq. 6.1 b is an assumed form of the sink behavior and has a property such that at large  $t \gg \tau$ ,  $\tanh(t/\tau)$  approaches unity realizing the full oxidation capacity for pollutants.

Dividing both sides of Eq. 6.1 a by  $C_o AU$ , where  $C_o$  is the initial concentration of pollutant in the box,  $A$  is the cross sectional area of the box, and  $U$  is the through-flow velocity as determined from  $U=Q/A$  with  $Q$  being the volumetric feed rate. With the definition of the following dimensionless variables:

$$\begin{aligned}
C' &= C/C_o \\
t' &= Ut/L = t/t_R \\
\tau' &= \tau/t_R \\
S' &= S^*/C_o AU
\end{aligned}
\tag{6.2a-d}$$

Note  $\tau'$  is the ratio of kinetic to retention time. When this ratio is much larger than unity, kinetics time is longer compared to the flow retention time in the reactor.

Based on Eqs. 6.2 a-d, Eq. 6.1 a can be rewritten as,

$$\frac{dC'}{dt'} = (C_a' - C') - S' \tanh(t'/\tau')
\tag{6.3a}$$

Initial Condition:

$$t' = 0, \quad C' \equiv \frac{C}{C_o} = 1
\tag{6.4a}$$

At "large" time:

$$\begin{aligned}
t'/\tau' &\gg 1 \\
\frac{dC'}{dt'} &\rightarrow 0 \quad \text{and} \quad \tanh(t'/\tau') = 1 \\
C_a' - C_s' - S' &= 0 \\
S' = C_a' - C_s' &= 1 - C_s'
\end{aligned}
\tag{6.5b}$$

$C_s'$  is the steady-state concentration. The first order differential equation Eq. 6.3 a can be integrated by the 4th-order Runge-Kutta algorithm. First, rewrite Eq. 6.3 a as

$$\frac{dC'}{dt'} = f(t', C') = (C_a' - C') - S' \tanh(t'/\tau')
\tag{6.3b}$$

Using the Runge-Kutta algorithm,

$$\begin{aligned}
k_1 &= f(t_i', C_i') = 1 - C' - S' \left[ \frac{1 - \exp(-2t'/\tau')}{1 + \exp(-2t'/\tau')} \right] \\
k_2 &= f(t_i' + \Delta t/2, C_i' + k_1 \Delta t/2) = 1 - (C' + k_1 \Delta t/2) - S' \left[ \frac{1 - \exp(-2[t' + \Delta t/2]/\tau')}{1 + \exp(-2[t' + \Delta t/2]/\tau')} \right] \\
k_3 &= f(t_i' + \Delta t/2, C_i' + k_2 \Delta t/2) = 1 - (C' + k_2 \Delta t/2) - S' \left[ \frac{1 - \exp(-2[t' + \Delta t/2]/\tau')}{1 + \exp(-2[t' + \Delta t/2]/\tau')} \right] \\
k_4 &= f(t_i' + \Delta t, C_i' + k_3 \Delta t) = 1 - (C' + k_3 \Delta t) - S' \left[ \frac{1 - \exp(-2[t' + \Delta t]/\tau')}{1 + \exp(-2[t' + \Delta t]/\tau')} \right] \\
C_{i+1} &= C_i + \frac{1}{6} \Delta t [k_1 + k_4 + 2k_2 + 2k_3] \tag{6.5a-e}
\end{aligned}$$

The subscript "i" means the  $i^{\text{th}}$  time step. The integration over time becomes a marching process starting from the initial condition at  $i=0$ .

#### Instantaneous Zero Kinetic Model

At times, the physical and chemical process governing the kinetics may happen so fast when compared to the flow retention time that

$$\tau \ll t_R = L/U \text{ or } \tau' = \tau U/L \ll 1$$

In this case,  $\tau' \rightarrow 0$  for which  $\tanh(t'/\tau') \rightarrow 1$ , and Eq. 7.3 a reduces to

$$\frac{dC'}{dt'} \approx (C_a' - C') - S' \tag{6.3c}$$

Integrating Eq. 6.3 c with the initial condition Eq. 6.4 a,

$$\begin{aligned}
\tau' &\ll 1 \\
C' &= C_s' + (1 - C_s') \exp(-t') \tag{6.6}
\end{aligned}$$

Note that Eq. 6.6 does not have the kinetic time  $\tau$  as it becomes redundant. Surely, as  $t' \gg 1$ ,  $C' \rightarrow C_s'$  as it should in Eq. 6.6. It turns out that as  $\tau' \leq 0.1$ , the "full-blown"

kinetic model, Eq. 6.3 b, falls back to the instantaneous kinetic model. As such, Eq. 6.6 is also referred as the zero kinetic model, with  $\tau'=0$ .

When comparing the zero kinetic models with some test data showing slow kinetics, it is evident that the zero kinetic models, based on strictly flow retention time, cannot explain the slow kinetics of the test measurements, see Figure 6.10 (compare the dotted curve with the test data). In other words, the flow retention time is not controlling the conversion of NO gas, but the kinetics of physical/chemical process is. Figure 6.10 shows a better match between the kinetic model, using appropriate  $\tau$  values, with experimental measurements at various Bi concentrations. The kinetic time  $\tau$  is determined to be, respectively,  $1.5t_R$ ,  $0.6t_R$ ,  $1.2t_R$ , and  $1.4t_R$  for Bi concentration of 0.1%, 0.2%, 0.3%, and 0.4%. In dimensional term,  $\tau$  varies from 54s to 135s (given  $t_R=L/U=V/Q=1.5 \text{ min}=90\text{s}$ ). This is the time scale to fully realize the maximum rate of photocatalytic oxidation. In Figure 6.11, the NO removal and kinetic time constants are plotted for different bismuth (III) nitrate pentahydrate concentrations. The 0.2% Bi not only has the maximum NO removal amount, but also possesses the fastest kinetics for the maximum removal; and these two parameters are inversely related. In addition, these results are also consistent with the highest light absorbance (Figure 6.5), highest electron-hole separation efficiency (i.e. least electron-hole recombination and highest impedance, see ordinate-scale in Figure 6.6), and highest charge carrier transport properties (see abscissa-scale in Figure 6.6) for Bi=0.2, 0.1, 0.3 and 0.4%, respectively.

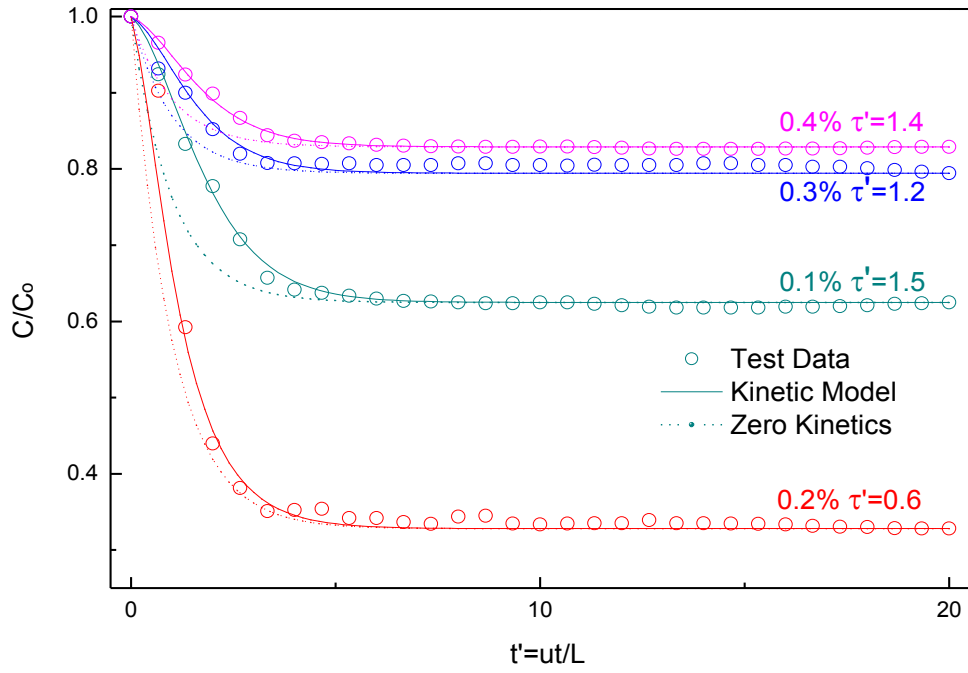


Figure 6.9 Kinetic model for the performance of TZB photocatalysts.

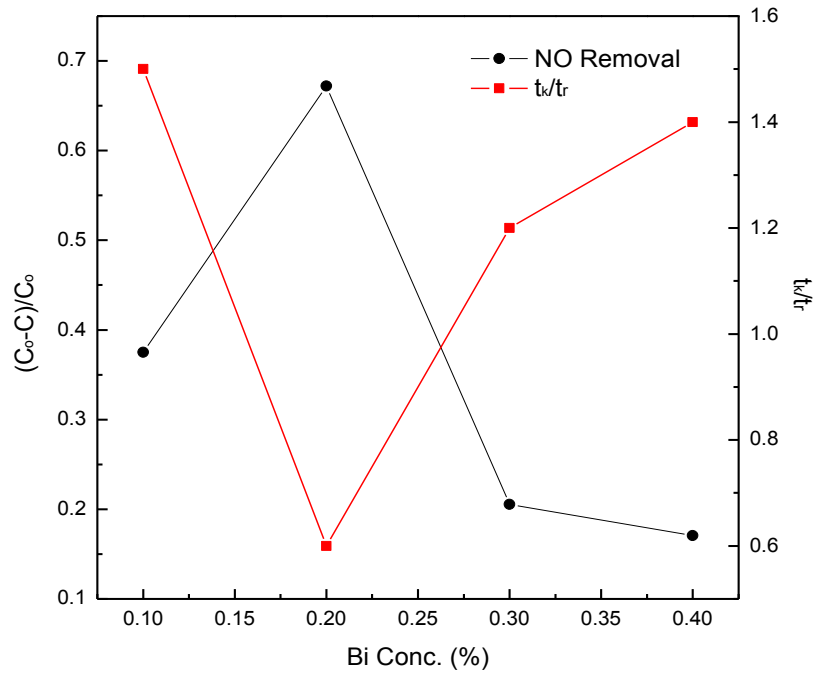


Figure 6.10 Plot of NO removal and kinetic time constants with different bismuth (III) nitrate pentahydrate concentrations.

## 6.5 Photocatalytic oxidation on the degradation of o-xylene

Taking into account photocatalytic theory and the synergistic effect among the four semiconductors, o-xylene was chosen as a representative volatile organic compounds (VOCs) pollutant to investigate the photocatalytic degradation process by TZB nanofibers and P25 TiO<sub>2</sub> nanoparticles (50 mg in each set of test) on full spectrum illumination. For 10 min illumination, the removal of o-xylene by commercial TiO<sub>2</sub> nanoparticles is very low (5.25%). In contrast, the removal by TZB nanofibers is up to 100%, which can be seen from Figure 6.12.

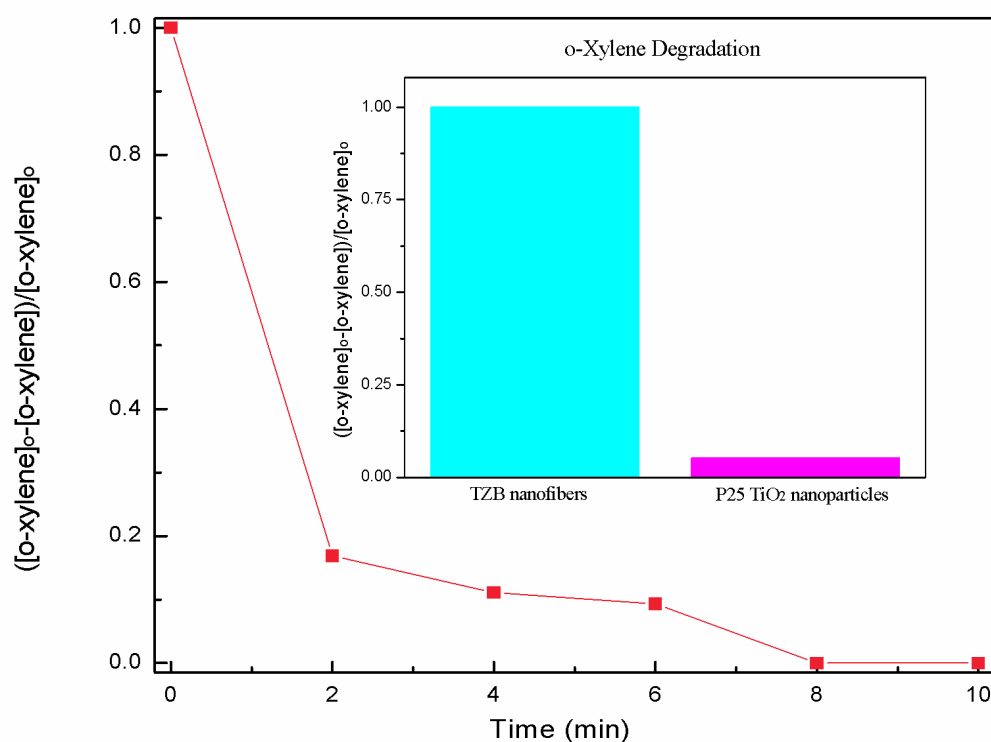


Figure 6.11 The relative variations of the o-xylene concentration against irradiation time in the presence of TZB nanofibers. Inset shows the benchmark test between TZB nanofibers and P25 nanoparticles with 10-min illumination.

In order to gain a deep insight into the o-xylene degradation by TZB nanofibers, the intermediates were identified and the evolution of major intermediates was investigated in each process. Nine intermediates (Compound 2 to 10) were identified according to different retention times in the GC spectrum during o-xylene degradation. The evolution profiles of o-xylene intermediates in the photocatalytic degradation process of TZB nanofibers are plotted in Figure 6.13.

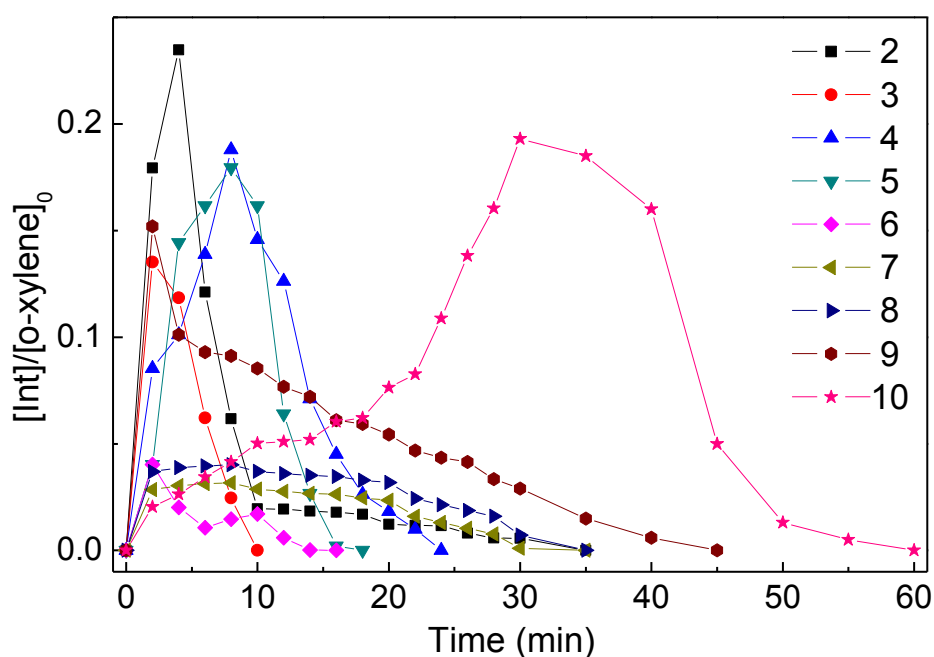
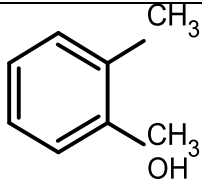
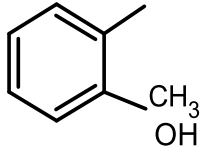
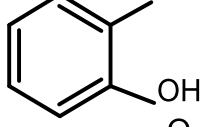
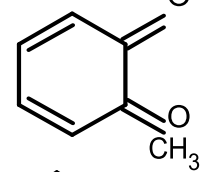
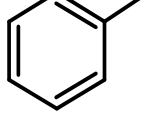
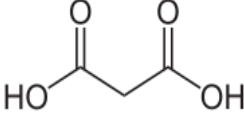
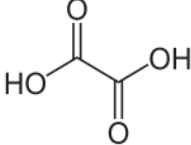
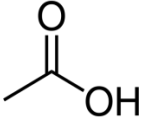
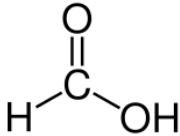


Figure 6.12 The evolution profiles of o-xylene intermediates in the photocatalytic degradation process of TZB nanofibers.

The information on the intermediates including the mass of deprotonated ion ( $[M-H]^+$ ) of the daughter compounds, the proposed molecular structure, and the proposed fragments are summarized in Table 6.1.

Table 6.1 Identified degradation products and their main fragments determined by GC-MS.

Compound	Retention time (min)	Molecular weight	Molecular ion and main fragments	Structural formula
o-xylene	26.818	106	106, 105, 91, 77, 51, 39	
2	29.016	108	108, 90, 77, 63, 51, 39, 27	
3	23.925	110	110, 92, 81, 63, 53, 39, 27	
4	21.142	108	108, 80, 73, 59, 54, 41	
5	22.764	92	91, 85, 73, 65, 51, 44, 39, 32	
6	19.184	78	78, 77, 63, 52, 39, 26, 15	
7	13.542	104	103, 57, 45, 33	
8	10.239	90	89, 61	
9	5.031	60	60, 45, 43, 29, 15,	

10	3.963	46	46, 45, 29,17, 12	
----	-------	----	----------------------	---

Based on the intermediate products identified in the present system, the possible pathway for the photocatalytic degradation of o-xylene can be described as indicated in Figure 6.14. The decomposition of o-xylene was initiated by the attack of  $\bullet\text{OH}$  on the methyl group of the benzene ring, leading to the generation of compounds 2 and 3 at the first step. When the  $\bullet\text{OH}$  further oxidizes the methyl group and the hydroxyl group on the benzene ring, compounds 4, 5 and 6 are formed, respectively. The emergence of compound 10 was accompanied by the oxidation of methyl group at the beginning of the reaction. Compounds 7, 8, 9 and 10 are generated from the open-ring reaction. The final mineralization of these compounds lead to the formation of  $\text{CO}_2$  and  $\text{H}_2\text{O}$ , which are too small in size to be detected in this set of experiment.

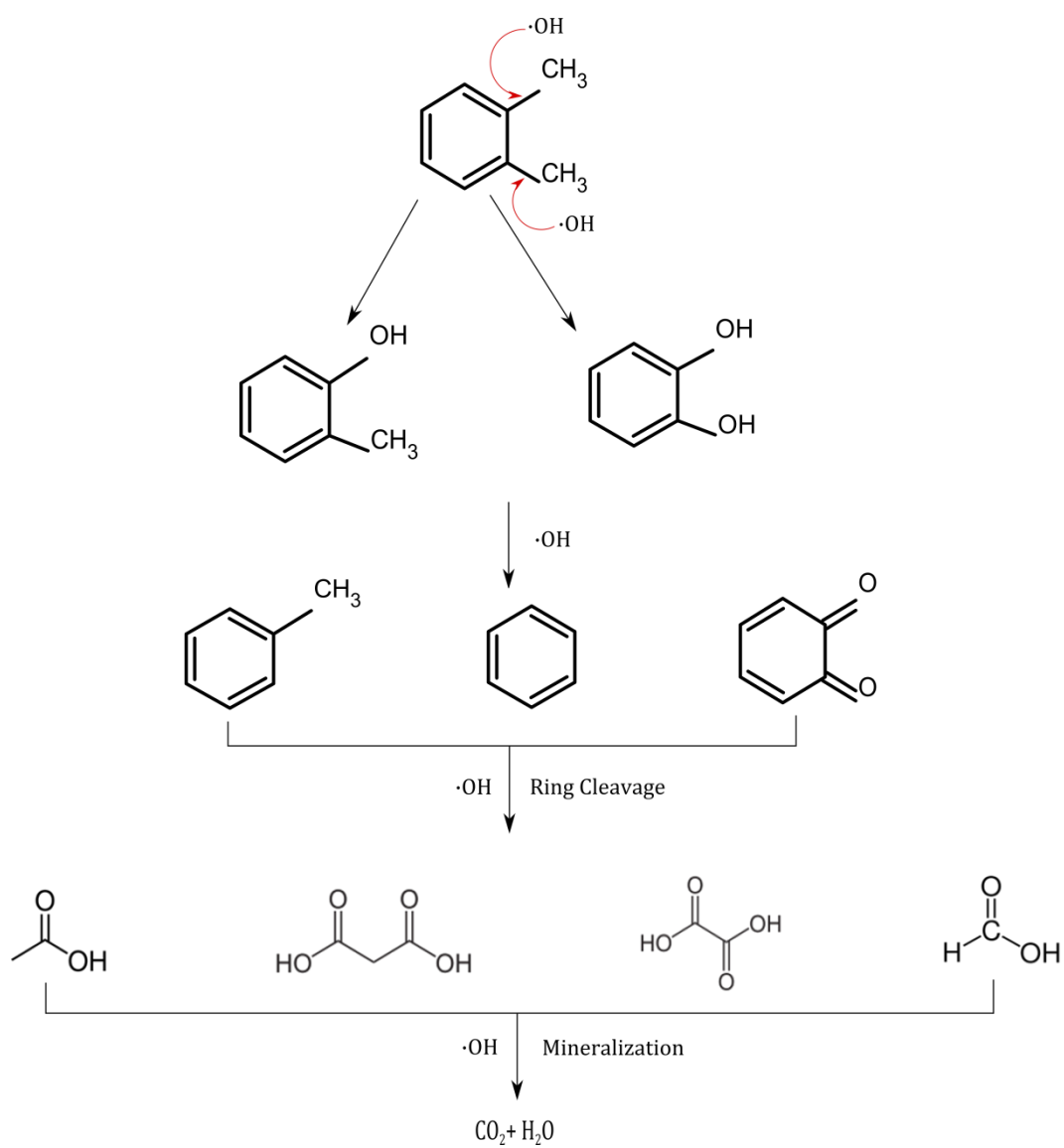


Figure 6.13 Proposed photocatalytic degradation pathway of o-xylene in the present system.

## 6.6 Summary

TiO<sub>2</sub>/ZnO/Bi<sub>2</sub>O<sub>3</sub> composite nanofibers containing various Bi concentrations were synthesized by a sol-gel assist electrospinning method, followed by a heat treatment procedure at 650 °C. The detailed morphology was characterized by SEM and TEM measurements. The as-synthesized composite nanofibers exhibited much higher photocatalytic activity for the oxidation of NO under simulated solar irradiation than commercial TiO<sub>2</sub> nanoparticles. The interlayers among these semiconductors were found to effectively separate photogenerated electron/hole pairs, as confirmed by the DRS and EIS measurements. The enhanced photocatalytic activity of TZB is attributed to the difference in the energy band positions of anatase, rutile, zincite and bismuth oxide. The particular energy diagram results in the lower band gap energy level and recombination rate due to greater charge separation. These composite nanofibers have increased absorption in both UV and visible range when compared with TiO<sub>2</sub> nanoparticles. Moreover, the photocatalytic performances are more stable of TZB nanofibers than that of TiO<sub>2</sub> nanoparticles, which get deactivated easily. The degradation of o-xylene is also studied by GC/MS and a possible pathway is proposed arising from the intermediates information.

The effective TiO<sub>2</sub>/ZnO/Bi<sub>2</sub>O<sub>3</sub> nanofibers can offer the perspective of developing a new generation of efficient photocatalytic material, which benefit environmental remediation and purification processes.

# Chapter 7

## Conclusions and Recommendations for Future Research

### 7.1 Conclusions

In this study, inorganic nanofibers have been successfully prepared via a sol-gel assisted nozzle-less electrospinning process followed by heat treatment. Nanofibers made from titanium dioxide have proven to perform better in photocatalytic oxidation than its counterpart taking form of nanoparticles. Furthermore, composite nanofibers from several specific semiconductors, such as titanium, zinc and bismuth oxides can further boost the photocatalytic performance to a much higher level due to synergistic effects. Finally, the composite nanofibers have been applied to photocatalytic degradation of RhB dye in liquid suspension, NO gas conversion, and degradation of o-xylene in air.

Nanofibers with fiber diameter 80-120 nm show much higher photocatalytic efficiency than those of the smaller size commercial nanoparticles (such as P25, size 25-38 nm) despite they have comparable specific surface areas. This is due to the nanofibers being packed with much smaller crystallites with size of 10 nm. The nanopores between the crystallites enhance physical contact between the target molecules and the surface of the catalyst, and the improved adsorption further favors photocatalytic reactions.

The performance of composite nanofibers is much better when compared to pure TiO<sub>2</sub> nanofibers. In TiO<sub>2</sub>/ZnO nanofibers, the amount of Zn content is found to play an important role on the photocatalytic activity. The optimal concentration of ZnAc in the precursor solution is determined to be 0.30 wt.% (6.0 wt.% TIP) and 0.10 wt.% (3.0 wt.% TIP). This optimum is obtained by balancing the competing effects between the unfavorable increased in specific surface areas due to addition of zinc and the favorable increase in surface oxygen vacancies.

We have studied the effect of photocatalyst dosage and the light intensity in the degradation of RhB in aqueous suspension. An optimal catalyst loading of 2 g L<sup>-1</sup> TiO<sub>2</sub>/ZnO has been determined to yield the most efficient degradation. This catalyst loading balances the favorable increased active sites of the catalyst in suspension versus the unfavorable increasing opacity from agglomeration of catalyst under higher catalyst loading. The degradation rate of RhB due to photocatalytic oxidation increase with increasing light intensity, which is due to the addition of photon dosage that induces more electron-hole pairs generation.

The role of illumination area, humidity and the residence time in the photocatalytic oxidation (PCO) of TiO<sub>2</sub>/ZnO nanofibers on the conversion of NO has been investigated. With increasing irradiation area of the photocatalyst, the NO removal increases due to enhance light harvesting and permeability. With increasing humidity PCO also increases due to generating of free radicals for triggering the reaction. However, excessive water molecules can occupy and block the active sites of the catalyst. Balancing these two factors, an optimal relative humidity of 50% has been found for efficient removal of NO. NO removal increases with increasing residence time as there is longer contact time between NO and the photogenerated hydroxyl

radicals.

The effect of anatase/rutile ratio on photocatalytic activity has been investigated. TiO<sub>2</sub>/ZnO nanofibers have been fabricated by calcination at different temperatures changing the anatase/rutile ratio. XRD analysis reveals that the nanofibers are composed of ZnO, anatase and rutile with different anatase/rutile ratio when calcinated at different temperatures. The grain size of the nanocrystallites making up the nanofibers is found to increase with temperature resulting in less surface area for photocatalytic reaction. Upon balancing these trade-off, it has been determined that the optimal calcination temperature for preparation of TiO<sub>2</sub>/ZnO nanofibers leading to the highest photocatalytic efficiency is 650 °C. The optimal combination of these three semiconductors anatase/rutile/zinc oxide can (a) reduce the band gap energy when compared with pure TiO<sub>2</sub> nanofibers facilitating more electron-hole pair for generating radicals for PCO activities and (b) enhance charge separation upon photoexcitation reducing electron-hole recombination. Thus, the optimal concentration results in much enhanced photocatalytic activity.

One additional semiconductor, Bi<sub>2</sub>O<sub>3</sub>, is incorporated in the composite nanofibers to demonstrate the possible synergistic effect in composite photocatalysts. TiO<sub>2</sub>/ZnO/Bi<sub>2</sub>O<sub>3</sub> (TZB) nanofibers containing various Bi concentrations are synthesized. The as-synthesized composite nanofibers exhibit much higher photocatalytic activity for the oxidation of NO under simulated solar irradiation than commercial TiO<sub>2</sub> nanoparticles. The interlayers among these semiconductors are found to effectively separate photogenerated electron/hole pairs, as confirmed by the DRS and EIS measurements. The enhanced photocatalytic activity of TZB is attributed to the difference in the energy band positions of anatase, rutile, zincite and

bismuth oxide. The composite nanofibers have increased absorption in both UV and visible range when compared with TiO<sub>2</sub> nanoparticles. Moreover, the photocatalytic performance is more stable for TZB nanofibers than that of TiO<sub>2</sub> nanoparticles, which can be easily deactivated. The optimal bismuth concentration in the composite nanofibers corresponds to the case with best electron/hole pair separation, maximum absorption in UV and visible wavelength, fastest kinetics, and maximum photocatalytic activities. The degradation of o-xylene is also studied by GC/MS. Similar conclusion on PCO of o-xylene can be drawn when comparing TZB nanofibers with TiO<sub>2</sub> nanoparticles. Furthermore, a possible pathway is proposed arising from the intermediate products being formed before the final degradation of o-xylene to carbon dioxide and water vapor.

To conclude, the experimental results in the present study demonstrate that the composite nanofibers can offer a promising prospect of developing a novel, efficient photocatalyst that would greatly benefit environmental remediation and purification process.

## **7.2 Recommendations for future research**

### **7.2.1 p-n semiconductors composite nanofibers**

Semiconductors can be divided into two categories, n-type semiconductors, in which there is an excess of electrons, and p-type semiconductors, in which there is a deficiency of electrons.

While titanium dioxide, zinc oxide, and bismuth oxide are all n-type semiconductors,

it has been known that p-n heterojunction-type photocatalysts not only can expand semiconductor responding wavelength range through sensitization effect, but also restrain charge carrier recombination through the built-in electric field effect, thus greatly improve the photocatalytic performance of the material.

P-type semiconductor, such as CuO (1.2 eV), Cu<sub>2</sub>O (2.0 eV), and CdTe (1.4eV) can also be used in the above mentioned principle where a p-type semiconductor say P1 can be used with energy level higher than zinc oxide so that it can trigger transfer of electron to zinc and zinc to Ti, and from Ti to Bi. Vice versa, the holes are readily transferred from the n-type Zn to the p-type P1, which kicks off a series of hole transfer from Bi to Ti, and from Ti to Zn, and Zn to P1. Similar logic applies for having a second p-type semiconductor P2, with energy level even higher than P1. The energy cascade is shown in Figure 7.1.

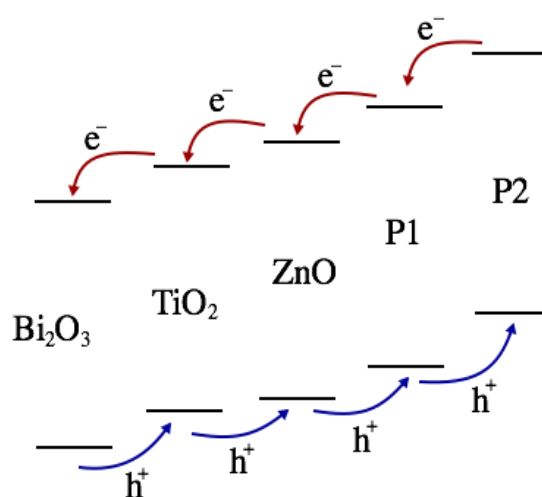


Figure 7.1 Energy cascade of TZB-P1-P2 photocatalyst.

The additional of p-type semiconductor, with proper energy level, can further improve the catalyst capability.

## **7.2.2 Carbon nanotube (CNT)/ TiO<sub>2</sub> composite nanofibers**

### **7.2.2.1 Overview**

The photocatalytic activity of wide band gap semiconductors has been the subject of numerous studies due to their ability to simultaneously harvest solar energy and drive chemical reactions via photoexcited charge carriers and activated electronic states. Among these materials, TiO<sub>2</sub> is particularly noteworthy because of its robust performance, nontoxicity and chemical stability. Numerous photocatalytic applications for TiO<sub>2</sub> have been proposed including liquid and gas phase organic contaminant degradation and water photolysis. A popular pathway for enhancing photocatalytic activity is to form carbon nanotube (CNT)–TiO<sub>2</sub> composite photocatalysts (Zhang et al. 2010, Woan et al. 2009, Lee et al. 2012). CNT has been used as template or scaffold for the hybrid assembly of nanoparticles by keeping their morphology and structure even at high nanoparticle loadings. Thus, composites containing CNT are believed to provide many applications and exhibit cooperative or synergetic effects between TiO<sub>2</sub> and carbon phases.

### **7.2.2.2 Preliminary results**

#### **7.2.2.2.1 CNT/TiO<sub>2</sub> nanotubes**

TiO<sub>2</sub> nanofibers with multi-wall carbon nanotube (MWCNT) are fabricated through electrospinning. Figure 7.2 represents the SEM picture of the nanostructure before and after heat treatment. It shows that before calcination, there are continuous, smooth and uniform nanofibers. However, after calcination, there are truncated nanofibers, in

other words, nanorods. This is due to the differences in the thermal expansion coefficient between  $\text{TiO}_2$  and MWCNT. During heating, the thermal expansion differs between  $\text{TiO}_2$  and CNT; leading to the difference in the fiber elongation, thus cause the truncation in fibers when cooling down, resulting in nanotubes. The TEM images of pure CNT and CNT/ $\text{TiO}_2$  are shown in Figure 7.3. In the latter, it is noted that the CNT diameters are around 7 nm, and they are buried inside the  $\text{TiO}_2$  nanocrystals. As such, the CNT can function as an electron/hole transfer ‘highway’, thereby increasing the photocatalytic efficiency.

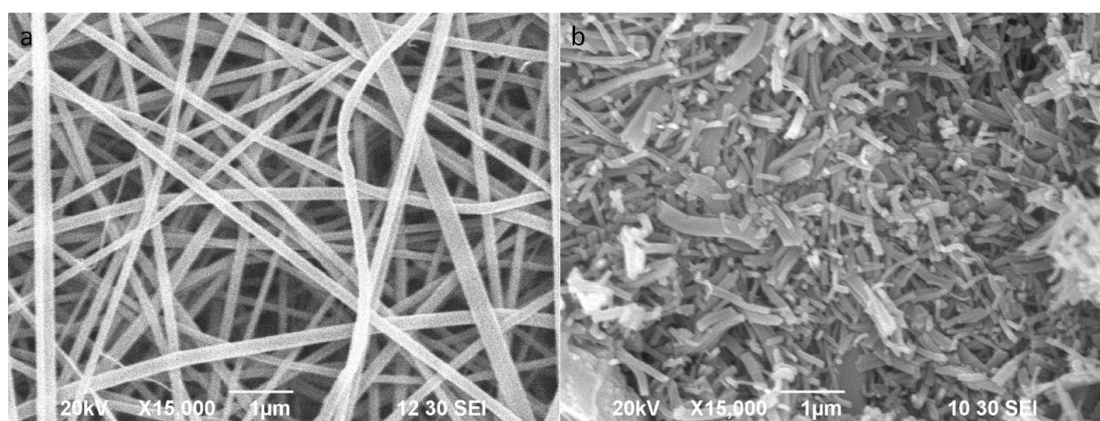


Figure 7.2 The SEM picture of CNT/ $\text{TiO}_2$  nanofibers before (a) and after (b) calcination.

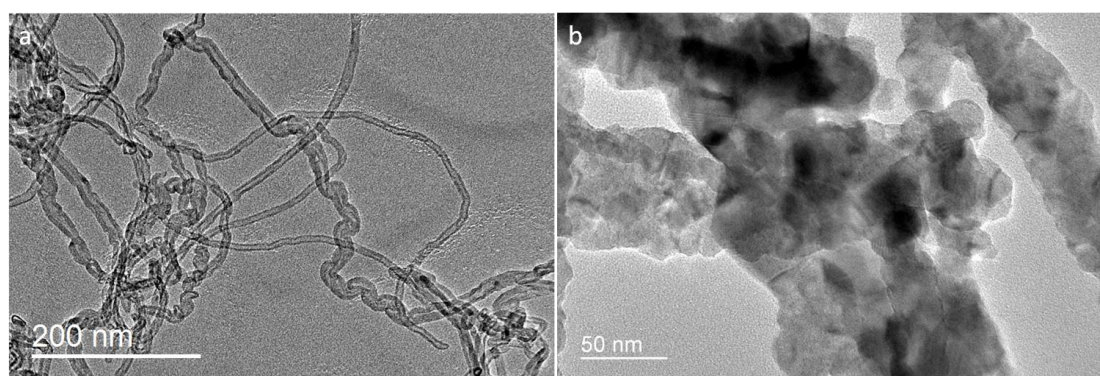


Figure 7.3 The TEM picture of MWCNT (a) and CNT/ $\text{TiO}_2$  nanotubes (b).

Figure 7.4 shows the NO removal rate against irradiation time in the present of

different CNT/TiO<sub>2</sub> nanotubes (prepared under different CNT concentration) and P25 TiO<sub>2</sub> nanoparticles under simulated solar-light irradiation with single-pass flow through the reactor. After 30 min irradiation, 15.0%, 13.2%, 15.1% and 16.2% of NO was oxidized by the CNT/TiO<sub>2</sub> prepared with CNT concentration of 0, 0.1%, 0.2% and 0.4%, respectively; and 6% of P25 nanoparticles. Moreover, the removal of NO by TiO<sub>2</sub> nanofibers increase ultimately to a stable value at around 10 min, but the removals of NO by CNT/TiO<sub>2</sub> increase rapidly to a highest value around 30% and then decrease to around 15%. Similar performance also can be noticed on TiO<sub>2</sub> nanoparticles. The performances vary from morphology, and the detail mechanism needs to be investigated in the future.

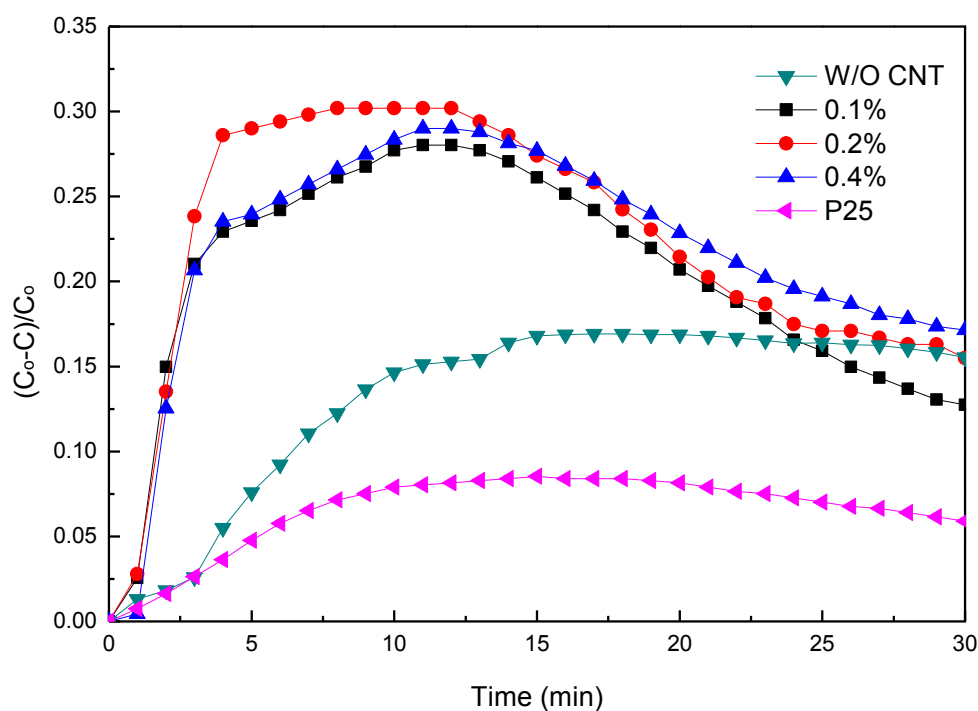


Figure 7.4 The NO removal rate against irradiation time in the present of different CNT/TiO<sub>2</sub> nanotubes and P25 TiO<sub>2</sub> nanoparticles under simulated solar-light irradiation with single-pass flow through the reactor.

#### 7.2.2.2.2 CNT/TZB nanofibers

The SEM picture and TEM picture of CNT/TZB nanofibers are shown in Figure 7.5. After calcination, the precursor nanofibers remain as nanofibers. This is because the thermal expansions for these four materials do not vary greatly as compared to pure TiO<sub>2</sub> and CNT, so that the nanofibers morphology remains unchanged. CNT is also inside the TZB nanofibers, similar as the structure of CNT/TiO<sub>2</sub> nanotubes.

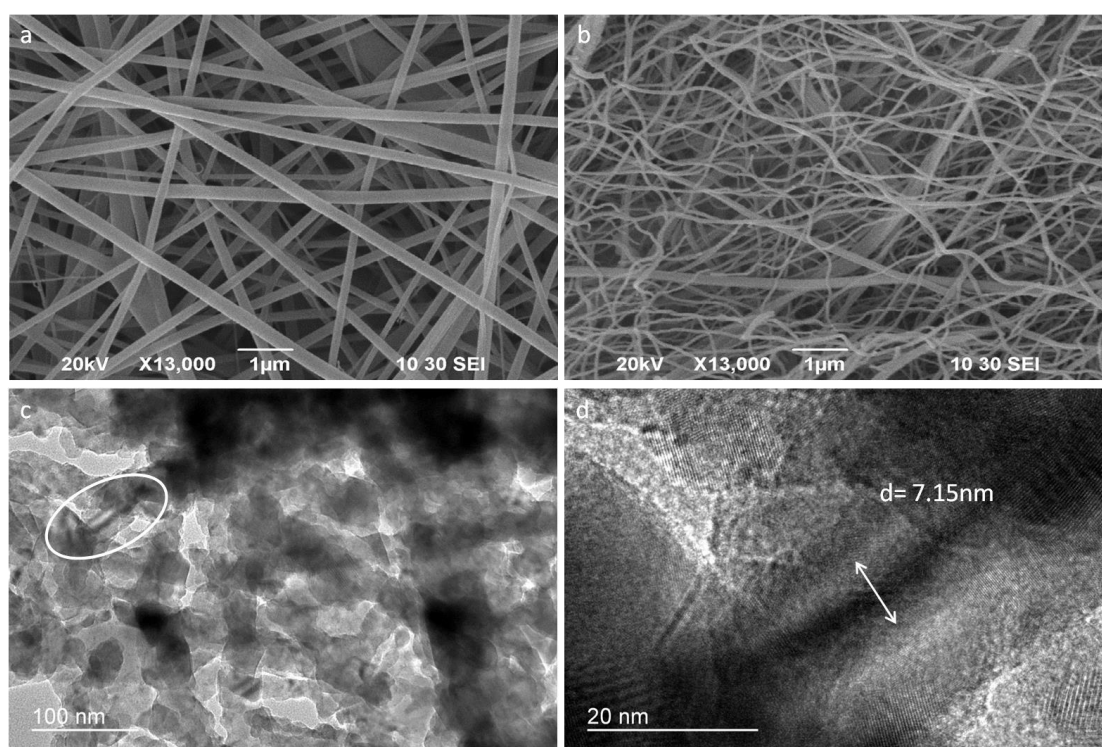


Figure 7.5 The SEM picture of CNT/TZB nanofibers before and after calcination (a and b), and the TEM images in different magnifications (c and d).

Figure 7.6 shows the NO removal rate against irradiation time in the present of TZB nanofibers, CNT/TZB nanofibers and P25 TiO<sub>2</sub> nanoparticles under simulated solar-light irradiation with single-pass flow through the reactor. It reveals that the TZB has the higher NO removal, but need longer time to reach to the highest removal rate than that of the CNT/TZB nanofibers. Figure 7.7 shows fast kinetics with the

CNT/TZB nanofibers. Despite the ultimate conversion is not that high, the kinetics for the CNT/TZB nanofibers are much more superior. This phenomenon needs to be deliberated in the future research.

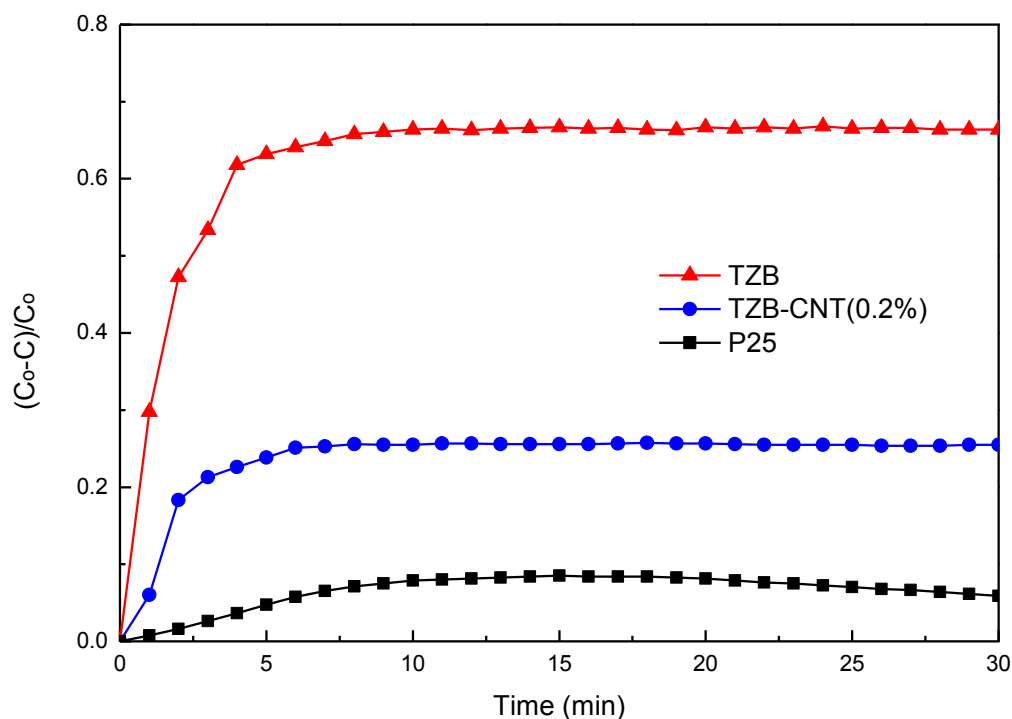


Figure 7.6 The NO removal rate against irradiation time in the present of TZB nanofibers, CNT/TZB nanofibers, and P25 TiO<sub>2</sub> nanoparticles under simulated solar-light irradiation with single-pass flow through the reactor.

Up to now, the successful applications of TiO<sub>2</sub> composite nanofibers under solar light for water treatment and air purification have been carried out. Future research should be focused on further increase the photocatalytic activity and the mechanism and kinetics behind the photocatalytic performance.

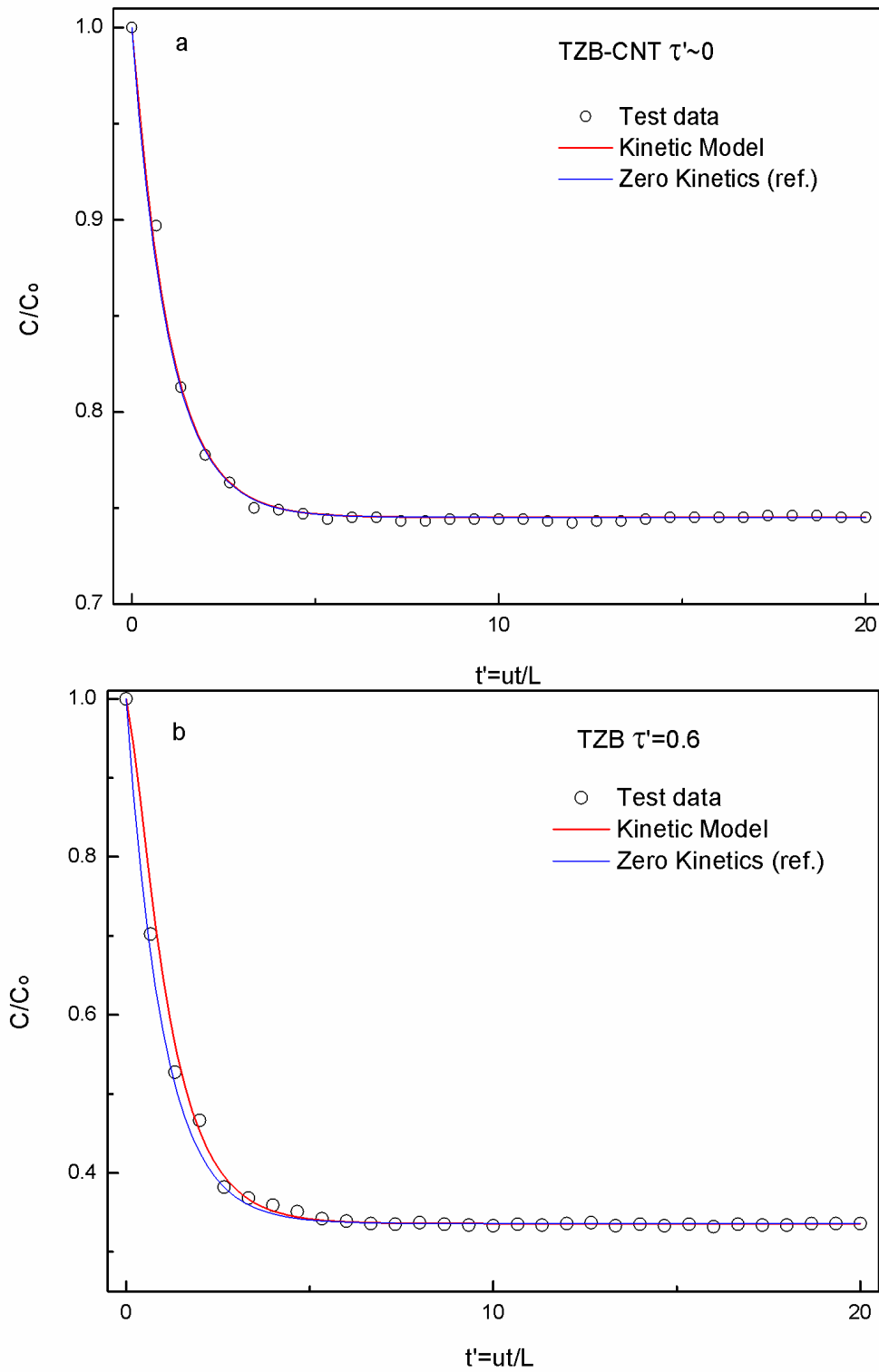


Figure 7.7 The plot of test data and box model data of CNT/TZB nanofibers and TZB nanofibers.

**Appendix** The absolute energy positions of conduction and valence bands of selected semiconductors (Xu and Schoonen 2000).

Semiconductor	E <sub>g</sub> (eV)	ECB (VS. NHE)	EVB (VS. NHE)	Semiconductor	E <sub>g</sub> (eV)	ECB (VS. NHE)	EVB (VS. NHE)
Ag <sub>2</sub> O	1.2eV	0.19	1.39	AlTiO <sub>3</sub>	3.6eV	-0.86	2.74
BaTiO <sub>3</sub>	3.3eV	0.08	3.38	Bi <sub>2</sub> O <sub>3</sub>	2.8eV	0.33	3.13
CdO	2.2eV	0.11	2.31	CdFe <sub>2</sub> O <sub>4</sub>	2.3eV	0.18	2.48
Ce <sub>2</sub> O <sub>3</sub>	2.4eV	-0.5	1.9	CoO	2.6eV	-0.11	2.49
CoTiO <sub>3</sub>	2.25eV	0.14	2.39	Cr <sub>2</sub> O <sub>3</sub>	3.5eV	-0.57	2.93
CuO	1.7e V	0.46	2.16	Cu <sub>2</sub> O	2.2eV	-0.28	1.92
CuTiO <sub>3</sub>	2.99eV	-0.18	2.81	FeO	2.4eV	-0.17	2.23
Fe <sub>2</sub> O <sub>3</sub>	2.2eV	0.28	2.48	Fe <sub>3</sub> O <sub>4</sub>	0.1eV	1.23	1.33
FeOOH	2.6eV	0.58	3.18	FeTiO <sub>3</sub>	2.8eV	-0.21	2.59
Ga <sub>2</sub> O <sub>3</sub>	4.8eV	-1.55	3.25	HgO	1.9eV	0.63	2.53
Hg <sub>2</sub> Nb <sub>2</sub> O <sub>7</sub>	1.8eV	0.81	2.61	Hg <sub>2</sub> Ta <sub>2</sub> O <sub>7</sub>	1.8eV	0.84	2.64
In <sub>2</sub> O <sub>3</sub>	2.8eV	-0.62	2.18	KNbO <sub>3</sub>	3.3eV	-0.86	2.44
KTaO <sub>3</sub>	3.5eV	-0.93	2.57	La <sub>2</sub> O <sub>3</sub>	5.5eV	-1.97	3.53
LaTi <sub>2</sub> O <sub>7</sub>	4eV	-0.6	3.4	LiNbO <sub>3</sub>	3.5eV	-0.73	2.77
LiTaO <sub>3</sub>	4eV	-0.95	3.05	MgTiO <sub>3</sub>	3.7eV	-0.75	2.95
MnO	3.6eV	-1.01	2.59	MnO <sub>2</sub>	0.25eV	1.33	1.58
MnTiO <sub>3</sub>	3.1eV	-0.46	2.64	Nb <sub>2</sub> O <sub>5</sub>	3.4eV	0.09	3.49
Nd <sub>2</sub> O <sub>3</sub>	4.7eV	-1.63	3.07	NiO	3.5eV	-0.5	3
NiTiO <sub>3</sub>	2.18eV	0.2	2.38	PbO	2.8eV	-0.48	2.32
PbFe <sub>12</sub> O <sub>19</sub>	2.3eV	0.2	2.5	PdO	1eV	0.79	1.79

<b>Semiconductor</b>	<b>E<sub>g</sub>(eV)</b>	<b>ECB (VS. NHE)</b>	<b>EVB (VS. NHE)</b>	<b>Semiconductor</b>	<b>E<sub>g</sub>(eV)</b>	<b>ECB (VS. NHE)</b>	<b>EVB (VS. NHE)</b>
Pr <sub>2</sub> O <sub>3</sub>	3.9eV	-1.26	2.64	Sb <sub>2</sub> O <sub>3</sub>	3eV	0.32	3.32
Sm <sub>2</sub> O <sub>3</sub>	4.4eV	-1.43	2.97	SnO	4.2eV	-0.91	3.29
SnO <sub>2</sub>	3.5eV	0	3.5	SrTiO <sub>3</sub>	3.4eV	-1.26	2.14
Ta <sub>2</sub> O <sub>5</sub>	4eV	-0.17	3.83	Tb <sub>2</sub> O <sub>3</sub>	3.8eV	-1.06	2.74
TiO <sub>2</sub>	3.2eV	-0.29	2.91	Tl <sub>2</sub> O <sub>3</sub>	1.6eV	0.05	1.65
V <sub>2</sub> O <sub>5</sub>	2.8eV	0.2	3	WO <sub>3</sub>	2.7eV	0.74	3.44
Yb <sub>2</sub> O <sub>3</sub>	4.9eV	-1.48	3.42	YFeO <sub>3</sub>	2.6eV	-0.2	2.4
ZnO	3.2eV	-0.31	2.89	ZnTiO <sub>3</sub>	3.06eV	-0.23	2.83
ZrO <sub>2</sub>	5eV	-1.09	3.91	Ag <sub>2</sub> S	0.92eV	0	0.92
AgAsS <sub>2</sub>	1.95eV	0.01	1.96	AgSbS <sub>2</sub>	1.72eV	0.01	1.73
As <sub>2</sub> S <sub>3</sub>	2.5eV	0.08	2.58	CdS	2.4eV	-0.52	1.88
Ce <sub>2</sub> S <sub>3</sub>	2.1eV	-0.91	1.19	CoS	0eV	0.67	0.67
CoS <sub>2</sub>	0eV	0.99	0.99	CoAsS	0.5eV	0.46	0.96
CuS	0eV	0.77	0.77	Cu <sub>2</sub> S	1.1eV	-0.06	1.04
CuS <sub>2</sub>	0eV	1.07	1.07	Cu <sub>3</sub> AsS <sub>4</sub>	1.28eV	0.25	1.53
CuFeS <sub>2</sub>	0.35eV	0.47	0.82	Cu <sub>5</sub> FeS <sub>4</sub>	1eV	0.05	1.05
CuInS <sub>2</sub>	1.5eV	-0.44	1.06	CuIn <sub>5</sub> S <sub>8</sub>	1.26eV	-0.41	0.85
Dy <sub>2</sub> S <sub>3</sub>	2.85eV	-1.14	1.71	FeS	0.1eV	0.47	0.57
FeS <sub>2</sub>	0.95eV	0.42	1.37	Fe <sub>3</sub> S <sub>4</sub>	0eV	0.68	0.68
RuS <sub>2</sub>	1.38eV	0.39	1.77	Sb <sub>2</sub> S <sub>3</sub>	1.72eV	0.22	1.94
Sm <sub>2</sub> S <sub>3</sub>	2.6eV	-1.11	1.49	SnS	1.01eV	0.16	1.17
SnS <sub>2</sub>	2.1eV	-0.06	2.04	Tb <sub>2</sub> S <sub>3</sub>	2.5eV	-0.99	1.51

<b>Semiconductor</b>	<b>E<sub>g</sub>(eV)</b>	<b>ECB (VS. NHE)</b>	<b>EVB (VS. NHE)</b>	<b>Semiconductor</b>	<b>E<sub>g</sub>(eV)</b>	<b>ECB (VS. NHE)</b>	<b>EVB (VS. NHE)</b>
TiS <sub>2</sub>	0.7eV	0.26	0.96	TlAsS <sub>2</sub>	1.8eV	-0.34	1.46
WS <sub>2</sub>	1.35eV	0.36	1.71	ZnS	3.6eV	-1.04	2.56
ZnS <sub>2</sub>	2.7eV	-0.29	2.41	Zn <sub>3</sub> In <sub>2</sub> S <sub>6</sub>	2.81eV	-0.91	1.9
ZrS <sub>2</sub>	1.82eV	-0.21	1.61				

## References

Adachi, M., Noda, K., Tanino, R., Adachi, J., Tsuchiya, K., Mori, Y. and Uchida, F. (2011) Comparison of Electrochemical Impedance Spectroscopy between Illumination and Dark Conditions. *Chemistry Letters* 40(8), 890-892.

Ardizzone, S., Bianchi, C.L., Cappelletti, G., Gialanella, S., Pirola, C. and Ragaini, V. (2007) Tailored Anatase/Brookite Nanocrystalline TiO<sub>2</sub>. The Optimal Particle Features for Liquid- and Gas-Phase Photocatalytic Reactions. *The Journal of Physical Chemistry C* 111(35), 13222-13231.

Arnal, P., Corriu, R.J.P., Leclercq, D., Mutin, P.H. and Vioux, A. (1996) Preparation of anatase, brookite and rutile at low temperature by non-hydrolytic sol-gel methods. *Journal of Materials Chemistry* 6(12), 1925-1932.

Asahi, R. and Morikawa, T. (2007) Nitrogen complex species and its chemical nature in TiO<sub>2</sub> for visible-light sensitized photocatalysis. *Chemical Physics* 339(1), 57-63.

Azouani, R., Michau, A., Hassouni, K., Chhor, K., Bocquet, J.F., Vignes, J.L. and Kanaev, A. (2010) Elaboration of pure and doped TiO<sub>2</sub> nanoparticles in sol-gel reactor with turbulent micromixing: Application to nanocoatings and photocatalysis. *Chemical Engineering Research and Design* 88(9), 1123-1130.

Bakardjieva, S., Šubrt, J., Štengl, V., Dianez, M.J. and Sayagues, M.J. (2005) Photoactivity of anatase–rutile TiO<sub>2</sub> nanocrystalline mixtures obtained by heat treatment of homogeneously precipitated anatase. *Applied Catalysis B: Environmental* 58(3–4), 193-202.

Baker, D.R. and Kamat, P.V. (2009) Photosensitization of TiO<sub>2</sub> Nanostructures with CdS Quantum Dots: Particulate versus Tubular Support Architectures. *Advanced Functional Materials* 19(5), 805-811.

Bakhtari, K., Guldiken, R.O., Makaram, P., Busnaina, A.A. and Park, J.-G. (2006) Experimental and Numerical Investigation of Nanoparticle Removal Using Acoustic Streaming and the Effect of Time. *Journal of The Electrochemical Society* 153(9), 846-850.

Balachandran, S. and Swaminathan, M. (2012) Facile Fabrication of Heterostructured Bi<sub>2</sub>O<sub>3</sub>-ZnO Photocatalyst and Its Enhanced Photocatalytic Activity. *The Journal of Physical Chemistry C* 116(50), 26306-26312.

Bashouti, M., Salalha, W., Brumer, M., Zussman, E. and Lifshitz, E. (2006) Alignment of Colloidal CdS Nanowires Embedded in Polymer Nanofibers by Electrospinning. *Chemical Physical Chemistry* 7(1), 102-106.

Bessekhouad, Y., Chaoui, N., Trzpit, M., Ghazzal, N., Robert, D. and Weber, J.V. (2006) UV-vis versus visible degradation of Acid Orange II in a coupled CdS/TiO<sub>2</sub> semiconductors suspension. *Journal of Photochemistry and Photobiology A: Chemistry* 183(1), 218-224.

Bessekhouad, Y., Robert, D. and Weber, J.V. (2005) Photocatalytic activity of Cu<sub>2</sub>O/TiO<sub>2</sub>, Bi<sub>2</sub>O<sub>3</sub>/TiO<sub>2</sub> and ZnMn<sub>2</sub>O<sub>4</sub>/TiO<sub>2</sub> heterojunctions. *Catalysis Today* 101(3), 315-321.

Bian, Z., Zhu, J., Wang, S., Cao, Y., Qian, X. and Li, H. (2008) Self-Assembly of Active Bi<sub>2</sub>O<sub>3</sub>/TiO<sub>2</sub> Visible Photocatalyst with Ordered Mesoporous Structure and

Highly Crystallized Anatase. The Journal of Physical Chemistry C 112(16), 6258-6262.

C. Martín, G.S., V. Rives, G. Marcì L. Palmisano, A. Sclafani (1997) Physico-chemical properties of WO<sub>3</sub>/TiO<sub>2</sub> systems employed for 4-nitrophenol photodegradation in aqueous medium. Catalysis Letters 49(3-4), 235-243.

Cai, Z., Li, J. and Wang, Y. (2010) Fabrication of zinc titanate nanofibers by electrospinning technique. Journal of Alloys and Compounds 489(1), 167-169.

Carp, O., Huisman, C.L. and Reller, A. (2004) Photoinduced reactivity of titanium dioxide. Progress in Solid State Chemistry 32(1-2), 33-177.

Cassaignon, S., Koelsch, M. and Jolivet, J.-P. (2007) Selective synthesis of brookite, anatase and rutile nanoparticles: thermolysis of TiCl<sub>4</sub> in aqueous nitric acid. Journal of Materials Science 42(16), 6689-6695.

Chai, S., Kim, Y. and Lee, W. (2006) Photocatalytic WO<sub>3</sub>/TiO<sub>2</sub> nanoparticles working under visible light. Journal of Electroceramics 17(2-4), 909-912.

Chen, D., Jiang, Z., Geng, J., Wang, Q. and Yang, D. (2007) Carbon and Nitrogen Co-doped TiO<sub>2</sub> with Enhanced Visible-Light Photocatalytic Activity. Industrial & Engineering Chemistry Research 46(9), 2741-2746.

Chen, X. and Burda, C. (2008) The Electronic Origin of the Visible-Light Absorption Properties of C-, N- and S-Doped TiO<sub>2</sub> Nanomaterials. Journal of the American Chemical Society 130(15), 5018-5019.

Choi, Y.J., Seeley, Z., Bandyopadhyay, A., Bose, S. and Akbar, S.A. (2007)

Aluminum-doped TiO<sub>2</sub> nano-powders for gas sensors. *Sensors and Actuators B: Chemical* 124(1), 111-117.

Chorfi, H., Saadoun, M., Bousselmi, L. and Bessais, B. (2012) TiO<sub>2</sub>-ITO and TiO<sub>2</sub>-ZnO nanocomposites: application on water treatment. *EPJ Web of Conferences* 29, 00015.

Cong, Y., Zhang, J., Chen, F. and Anpo, M. (2007) Synthesis and Characterization of Nitrogen-Doped TiO<sub>2</sub> Nanophotocatalyst with High Visible Light Activity. *The Journal of Physical Chemistry C* 111(19), 6976-6982.

Darwin Castillo, J.O., Arvids Stashans (2014) Geometry of dopamine adsorption on rutile (110) surface. *International Journal of Modern Physics B* doi: 10.1142/S0217979214500714.

Daskalaki, V.M., Antoniadou, M., Li Puma, G., Kondarides, D.I. and Lianos, P. (2010) Solar Light-Responsive Pt/CdS/TiO<sub>2</sub> Photocatalysts for Hydrogen Production and Simultaneous Degradation of Inorganic or Organic Sacrificial Agents in Wastewater. *Environmental Science & Technology* 44(19), 7200-7205.

Ding, X., Song, X., Li, P., Ai, Z. and Zhang, L. (2011) Efficient visible light driven photocatalytic removal of NO with aerosol flow synthesized B, N-codoped TiO<sub>2</sub> hollow spheres. *Journal of Hazardous Materials* 190(1-3), 604-612.

Dreher, K.L. (2004) Health and Environmental Impact of Nanotechnology: Toxicological Assessment of Manufactured Nanoparticles. *Toxicological Sciences* 77(1), 3-5.

Du, P., Song, L., Xiong, J. and Cui, C. (2013) Optimization of electrospun TiO<sub>2</sub>

nanofibers photoanode film for dye-sensitized solar cells through interfacial pre-treatment, controllable calcination, and surface post-treatment. *Surface and Interface Analysis* 45(13), 1878-1883.

Dunnill, C.W., Kafizas, A. and Parkin, I.P. (2012) CVD Production of Doped Titanium Dioxide Thin Films. *Chemical Vapor Deposition* 18(4-6), 89-101.

El-Bahy, Z.M., Ismail, A.A. and Mohamed, R.M. (2009) Enhancement of titania by doping rare earth for photodegradation of organic dye (Direct Blue). *Journal of Hazardous Materials* 166(1), 138-143.

Evans, J.E., Springer, K.W. and Zhang, J.Z. (1994) Femtosecond studies of interparticle electron transfer in a coupled CdS-TiO<sub>2</sub> colloidal system. *The Journal of Chemical Physics* 101(7), 6222-6225.

Evgenidou, E., Fytianos, K. and Poullos, I. (2005) Semiconductor-sensitized photodegradation of dichlorvos in water using TiO<sub>2</sub> and ZnO as catalysts. *Applied Catalysis B: Environmental* 59(1-2), 81-89.

Fujishima, A. and Honda, K. (1972) Electrochemical Photolysis of Water at a Semiconductor Electrode. *Nature* 238(5358), 37-38.

Gao, X.-F., Sun, W.-T., Hu, Z.-D., Ai, G., Zhang, Y.-L., Feng, S., Li, F. and Peng, L.-M. (2009) An Efficient Method To Form Heterojunction CdS/TiO<sub>2</sub> Photoelectrodes Using Highly Ordered TiO<sub>2</sub> Nanotube Array Films. *The Journal of Physical Chemistry C* 113(47), 20481-20485.

Gerloff, K., Fenoglio, I., Carella, E., Kolling, J., Albrecht, C., Boots, A.W., Förster, I. and Schins, R.P.F. (2012) Distinctive Toxicity of TiO<sub>2</sub> Rutile/Anatase Mixed Phase

Nanoparticles on Caco-2 Cells. *Chemical Research in Toxicology* 25(3), 646-655.

Hamadani, M., Reisi Vanani, A. and Majedi, A. (2009) Preparation and characterization of S-doped TiO<sub>2</sub> nanoparticles, effect of calcination temperature and evaluation of photocatalytic activity. *Materials Chemistry and Physics* 116(2 欵?), 376-382.

Hao, Y., Yang, X., Zhou, M., Cong, J., Wang, X., Hagfeldt, A. and Sun, L. (2011) Molecular Design to Improve the Performance of Donor- $\pi$  Acceptor Near-IR Organic Dye-Sensitized Solar Cells. *ChemSusChem* 4(11), 1601-1605.

He, Y., Wu, Z., Fu, L., Li, C., Miao, Y., Cao, L., Fan, H. and Zou, B. (2003) Photochromism and Size Effect of WO<sub>3</sub> and WO<sub>3</sub>-TiO<sub>2</sub> Aqueous Sol. *Chemistry of Materials* 15(21), 4039-4045.

Hu, A., Griesing, S., Rybachuk, M., Lu, Q.-B. and Duley, W.W. (2007) Nanobuckling and x-ray photoelectron spectra of carbyne-rich tetrahedral carbon films deposited by femtosecond laser ablation at cryogenic temperatures. *Journal of Applied Physics* 102(7), 074311.

Hu, C., Hu, X., Wang, L., Qu, J. and Wang, A. (2006) Visible-Light-Induced Photocatalytic Degradation of Azodyes in Aqueous AgI/TiO<sub>2</sub> Dispersion. *Environmental Science & Technology* 40(24), 7903-7907.

Hu, W., Chen, S. and Xia, Q. (2014) IrO<sub>2</sub>/Nb-TiO<sub>2</sub> electrocatalyst for oxygen evolution reaction in acidic medium. *International Journal of Hydrogen Energy* 39(13), 6967-6976.

Hu, Y., Tsai, H.L. and Huang, C.L. (2003) Effect of brookite phase on the anatase-rutile transition in titania nanoparticles. *Journal of the European Ceramic Society* 23(5), 691-696.

Huang, D.-G., Liao, S.-J., Liu, J.-M., Dang, Z. and Petrik, L. (2006) Preparation of visible-light responsive N-F-codoped TiO<sub>2</sub> photocatalyst by a sol-gel-solvothermal method. *Journal of Photochemistry and Photobiology A: Chemistry* 184(3), 282-288.

Huang, K., Chen, L., Xiong, J. and Liao, M. (2012) Preparation and Characterization of Visible-Light-Activated Fe-N Co-Doped TiO<sub>2</sub> and Its Photocatalytic Inactivation Effect on Leukemia Tumors. *International Journal of Photoenergy* 2012, 9.

Huang, Y., Ho, W., Ai, Z., Song, X., Zhang, L. and Lee, S. (2009) Aerosol-assisted flow synthesis of B-doped, Ni-doped and B-Ni-codoped TiO<sub>2</sub> solid and hollow microspheres for photocatalytic removal of NO. *Applied Catalysis B: Environmental* 89(3-4), 398-405.

Huang, Y., Ho, W., Lee, S., Zhang, L., Li, G. and Yu, J.C. (2008) Effect of Carbon Doping on the Mesoporous Structure of Nanocrystalline Titanium Dioxide and Its Solar-Light-Driven Photocatalytic Degradation of NO<sub>x</sub>. *Langmuir* 24(7), 3510-3516.

huo, Y., jin, Y., zhu, J. and li, H. (2009) Highly active TiO<sub>2-x-y</sub>N<sub>x</sub>F<sub>y</sub> visible photocatalyst prepared under supercritical conditions in NH<sub>4</sub>F/EtOH fluid. *Applied Catalysis B: Environmental* 89(3), 543-550.

*International Journal of Modern Physics B*, 1450071.

Jang, J.S., Choi, S.H., Kim, H.G. and Lee, J.S. (2008) Location and State of Pt in

Platinized CdS/TiO<sub>2</sub> Photocatalysts for Hydrogen Production from Water under Visible Light. *The Journal of Physical Chemistry C* 112(44), 17200-17205.

Jang, J.S., Gyu Kim, H., Borse, P.H. and Lee, J.S. (2007) Simultaneous hydrogen production and decomposition of dissolved in alkaline water over composite photocatalysts under visible light irradiation. *International Journal of Hydrogen Energy* 32(18), 4786-4791.

Ji, T., Yang, F., Lv, Y., Zhou, J. and Sun, J. (2009) Synthesis and visible-light photocatalytic activity of Bi-doped TiO<sub>2</sub> nanobelts. *Materials Letters* 63(23), 2044-2046.

Kandiel, T.A., Robben, L., Alkaim, A. and Bahnemann, D. (2013) Brookite versus anatase TiO<sub>2</sub> photocatalysts: phase transformations and photocatalytic activities. *Photochemical & Photobiological Sciences*.

Karakitsou, K. and Verykios, X.E. (1995) Definition of the Intrinsic Rate of Photocatalytic Cleavage of Water over Pt-RuO<sub>2</sub>/TiO<sub>2</sub> Catalysts. *Journal of Catalysis* 152(2), 360-367.

Karunakaran, C., Abiramasundari, G., Gomathisankar, P., Manikandan, G. and Anandi, V. (2011) Preparation and characterization of ZnO–TiO<sub>2</sub> nanocomposite for photocatalytic disinfection of bacteria and detoxification of cyanide under visible light. *Materials Research Bulletin* 46(10), 1586-1592.

Kim, D.-W., Enomoto, N., Nakagawa, Z. and Kawamura, K. (1996) Molecular Dynamic Simulation in Titanium Dioxide Polymorphs: Rutile, Brookite, and Anatase. *Journal of the American Ceramic Society* 79(4), 1095-1099.

Kim, T.W., Hwang, S.J., Jhung, S.H., Chang, J.S., Park, H., Choi, W. and Choy, J.H. (2008) Bifunctional Heterogeneous Catalysts for Selective Epoxidation and Visible Light Driven Photolysis: Nickel Oxide-Containing Porous Nanocomposite. *Advanced Materials* 20(3), 539-542.

Kisch, H., Zang, L., Lange, C., Maier, W.F., Antonius, C. and Meissner, D. (1998) Modified, Amorphous Titania-A Hybrid Semiconductor for Detoxification and Current Generation by Visible Light. *Angewandte Chemie International Edition* 37(21), 3034-3036.

Koelsch, M., Cassaignon, S., Ta Thanh Minh, C., Guillemoles, J.F. and Jolivet, J.P. (2004) Electrochemical comparative study of titania (anatase, brookite and rutile) nanoparticles synthesized in aqueous medium. *Thin Solid Films* 451-452(0), 86-92.

Lai, Y., Meng, M., Yu, Y., Wang, X. and Ding, T. (2011) Photoluminescence and photocatalysis of the flower-like nano-ZnO photocatalysts prepared by a facile hydrothermal method with or without ultrasonic assistance. *Applied Catalysis B: Environmental* 105(3-4), 335-345.

Laufs, S., Burgeth, G., Duttlinger, W., Kurtenbach, R., Maban, M., Thomas, C., Wiesen, P. and Kleffmann, J. (2010) Conversion of nitrogen oxides on commercial photocatalytic dispersion paints. *Atmospheric Environment* 44(19), 2341-2349.

Lee, W., Lee, J., Lee, S., Yi, W., Han, S.-H. and Cho, B.W. (2008) Enhanced charge collection and reduced recombination of CdS-TiO<sub>2</sub> quantum-dots sensitized solar cells in the presence of single-walled carbon nanotubes. *Applied Physics Letters* 92(15), -.

Lee, W.J., Lee, J.M., Kochuveedu, S.T., Han, T.H., Jeong, H.Y., Park, M., Yun, J.M.,

Kwon, J., No, K., Kim, D.H. and Kim, S.O. (2012) Biomaterialized N-Doped CNT/TiO<sub>2</sub> Core/Shell Nanowires for Visible Light Photocatalysis. ACS Nano 6(1), 935-943.

Li, D. and Xia, Y. (2004) Electrospinning of Nanofibers: Reinventing the Wheel? Advanced Materials 16(14), 1151-1170.

Li, D., Haneda, H., Hishita, S. and Ohashi, N. (2005a) Visible-Light-Driven NF-codoped TiO<sub>2</sub> Photocatalysts. 2. Optical Characterization, Photocatalysis, and Potential Application to Air Purification. Chemistry of Materials 17(10), 2596-2602.

Li, D., Ohashi, N., Hishita, S., Kolodiazny, T. and Haneda, H. (2005b) Origin of visible-light-driven photocatalysis: A comparative study on N/F-doped and N-F-codoped TiO<sub>2</sub> powders by means of experimental characterizations and theoretical calculations. Journal of Solid State Chemistry 178(11), 3293-3302.

Li, H., Zhang, W., Li, B. and Pan, W. (2010) Diameter-Dependent Photocatalytic Activity of Electrospun TiO<sub>2</sub> Nanofiber. Journal of the American Ceramic Society 93(9), 2503-2506.

Li, J.-G., Ishigaki, T. and Sun, X. (2007) Anatase, Brookite, and Rutile Nanocrystals via Redox Reactions under Mild Hydrothermal Conditions: Phase-Selective Synthesis and Physicochemical Properties. The Journal of Physical Chemistry C 111(13), 4969-4976.

Linsebigler, A.L., Lu, G. and Yates, J.T. (1995) Photocatalysis on TiO<sub>2</sub> Surfaces: Principles, Mechanisms, and Selected Results. Chemical Reviews 95(3), 735-758.

Liu, G., Li, G., Qiu, X. and Li, L. (2009) Synthesis of ZnO/titanate nanocomposites

with highly photocatalytic activity under visible light irradiation. *Journal of Alloys and Compounds* 481(1), 492-497.

Liu, S., Liu, G. and Feng, Q. (2010) Al-doped TiO<sub>2</sub> mesoporous materials: synthesis and photodegradation properties. *Journal of Porous Materials* 17(2), 197-206.

Liu, Z., Sun, D.D., Guo, P. and Leckie, J.O. (2006) An Efficient Bicomponent TiO<sub>2</sub>/SnO<sub>2</sub> Nanofiber Photocatalyst Fabricated by Electrospinning with a Side-by-Side Dual Spinneret Method. *Nano Letters* 7(4), 1081-1085.

Liu, Z., Zhang, X., Nishimoto, S., Jin, M., Tryk, D.A., Murakami, T. and Fujishima, A. (2007) Anatase TiO<sub>2</sub> Nanoparticles on Rutile TiO<sub>2</sub> Nanorods: A Heterogeneous Nanostructure via Layer-by-Layer Assembly. *Langmuir* 23(22), 10916-10919.

Livraghi, S., Elghniji, K., Czoska, A.M., Paganini, M.C., Giamello, E. and Ksibi, M. (2009) Nitrogen-doped and nitrogen-fluorine-codoped titanium dioxide. Nature and concentration of the photoactive species and their role in determining the photocatalytic activity under visible light. *Journal of Photochemistry and Photobiology A: Chemistry* 205(2), 93-97.

Lommens, P., De Meyer, C., Bruneel, E., De Buysser, K., Van Driessche, I. and Hoste, S. (2005) Synthesis and thermal expansion of ZrO<sub>2</sub>/ZrW<sub>2</sub>O<sub>8</sub> composites. *Journal of the European Ceramic Society* 25(16), 3605-3610.

Long, M., Cai, W., Wang, Z. and Liu, G. (2006) Correlation of electronic structures and crystal structures with photocatalytic properties of undoped, N-doped and I-doped TiO<sub>2</sub>. *Chemical Physics Letters* 420(1), 71-76.

Lotus, A.F., Tacastacas, S.N., Pinti, M.J., Britton, L.A., Stojilovic, N., Ramsier, R.D.

and Chase, G.G. (2011) Fabrication and characterization of TiO<sub>2</sub>-ZnO composite nanofibers. *Physica E: Low-dimensional Systems and Nanostructures* 43(4), 857-861.

Lu, Y.M., Liu, C.K. and Huang, C.M. (2007) The Visible Photocatalysis Properties of Nitrogen-doped TiO<sub>2</sub> Thin Film. *ECS Transactions* 2(20), 101-107.

M Ferroni, M.C.C., V Guidi, G Martinelli, F Ronconi, O Richard, D Van Dyck, J Van Landuyt (2000) Structural characterization of Nb-TiO<sub>2</sub> nanosized thick-films for gas sensing application. *Sensors and Actuators B Chemical* 68(1-3), 140.

Madhavan, A.A., Mohandas, A., Licciulli, A., Sanosh, K.P., Praveen, P., Jayakumar, R., Nair, S.V., Nair, A.S. and Balakrishnan, A. (2013) Electrospun continuous nanofibers based on a TiO<sub>2</sub>-ZnO-graphene composite. *RSC Advances* 3(47), 25312-25316.

Martínez-Arias, Hungráb, A.B., Iglesias-Juez, A., Fernández-García, M., Anderson, J.A., Conesa, J.C., Munuera, G. and Soria, J. (2012) Redox and catalytic properties of CuO/CeO<sub>2</sub> under CO + O<sub>2</sub> + NO: Promoting effect of NO on CO oxidation. *Catalysis Today* 180(1), 81-87.

Matos, J., Laine, J., Herrmann, J.M., Uzcategui, D. and Brito, J.L. (2007) Influence of activated carbon upon titania on aqueous photocatalytic consecutive runs of phenol photodegradation. *Applied Catalysis B: Environmental* 70(1), 461-469.

Matsui, M. and Akaogi, M. (1991) Molecular Dynamics Simulation of the Structural and Physical Properties of the Four Polymorphs of TiO<sub>2</sub>. *Molecular Simulation* 6(4-6), 239-244.

Moon, J., Park, J.-A., Lee, S.-J., Zyung, T. and Kim, I.-D. (2010) Pd-doped TiO<sub>2</sub>

nanofiber networks for gas sensor applications. *Sensors and Actuators B: Chemical* 149(1), 301-305.

Nagaveni, K., Sivalingam, G., Hegde, M.S. and Madras, G. (2004) Solar photocatalytic degradation of dyes: high activity of combustion synthesized nano TiO<sub>2</sub>. *Applied Catalysis B: Environmental* 48(2), 83-93.

Nah, Y.C., Paramasivam, I. and Schmuki, P. (2010) Doped TiO<sub>2</sub> and TiO<sub>2</sub> Nanotubes: Synthesis and Applications. *ChemPhysChem* 11(13), 2698-2713.

Nakamura, R., Tanaka, T. and Nakato, Y. (2004) Mechanism for Visible Light Responses in Anodic Photocurrents at N-Doped TiO<sub>2</sub> Film Electrodes. *The Journal of Physical Chemistry B* 108(30), 10617-10620.

Nanayakkara, C.E., Pettibone, J. and Grassian, V.H. (2012) Sulfur dioxide adsorption and photooxidation on isotopically-labeled titanium dioxide nanoparticle surfaces: roles of surface hydroxyl groups and adsorbed water in the formation and stability of adsorbed sulfite and sulfate. *Physical Chemistry Chemical Physics* 14(19), 6957-6966.

Ozawa, K., Emori, M., Yamamoto, S., Yukawa, R., Yamamoto, S., Hobara, R., Fujikawa, K., Sakama, H. and Matsuda, I. (2014) Electron-Hole Recombination Time at TiO<sub>2</sub> Single-Crystal Surfaces: Influence of Surface Band Bending. *The Journal of Physical Chemistry Letters* 5(11), 1953-1957.

Ozawa, T., Iwasaki, M., Tada, H., Akita, T., Tanaka, K. and Ito, S. (2005) Low-temperature synthesis of anatase-brookite composite nanocrystals: the junction effect on photocatalytic activity. *Journal of Colloid and Interface Science* 281(2),

510-513.

Pan, J.H. and Lee, W.I. (2006) Preparation of Highly Ordered Cubic Mesoporous WO<sub>3</sub>/TiO<sub>2</sub> Films and Their Photocatalytic Properties. *Chemistry of Materials* 18(3), 847-853.

Paola, A.D., Ikeda, S., Marcì G., Ohtani, B. and Palmisano, L. (2001) Transition metal doped TiO<sub>2</sub>: physical properties and photocatalytic behaviour. *International Journal of Photoenergy* 3(4), 171-176.

Papp, J., Soled, S., Dwight, K. and Wold, A. (1994) Surface Acidity and Photocatalytic Activity of TiO<sub>2</sub>, WO<sub>3</sub>/TiO<sub>2</sub>, and MoO<sub>3</sub>/TiO<sub>2</sub> Photocatalysts. *Chemistry of Materials* 6(4), 496-500.

Park, H., Park, Y., Kim, W. and Choi, W. (2013) Surface modification of TiO<sub>2</sub> photocatalyst for environmental applications. *Journal of Photochemistry and Photobiology C: Photochemistry Reviews* 15(0), 1-20.

Park, J.H., Kim, S. and Bard, A.J. (2005) Novel Carbon-Doped TiO<sub>2</sub> Nanotube Arrays with High Aspect Ratios for Efficient Solar Water Splitting. *Nano Letters* 6(1), 24-28.

Park, M.S., Kwon, S.K. and Min, B.I. (2002) Electronic structures of doped anatase TiO<sub>2</sub>: Ti<sub>1-x</sub>M<sub>x</sub>O<sub>2</sub> (M=Co, Mn, Fe, Ni). *Physical Review B* 65(16), 161201.

Pei, C.C. and Leung, W.W.-F. (2013a) Enhanced photocatalytic activity of electrospun TiO<sub>2</sub>/ZnO nanofibers with optimal anatase/rutile ratio. *Catalysis Communications* 37(0), 100-104.

Pei, C.C. and Leung, W.W.-F. (2013b) Photocatalytic degradation of Rhodamine B by

TiO<sub>2</sub>/ZnO nanofibers under visible-light irradiation. *Separation and Purification Technology* 114(0), 108-116.

Peill, N.J., Bourne, L. and Hoffmann, M.R. (1997) Iron(III)-doped Q-sized TiO<sub>2</sub> coatings in a fiber-optic cable photochemical reactor. *Journal of Photochemistry and Photobiology A: Chemistry* 108(2), 221-228.

Perkgoz, N.K., Toru, R.S., Unal, E., Sefunc, M.A., Tek, S., Mutlugun, E., Soganci, I.M., Celiker, H., Celiker, G. and Demir, H.V. (2011) Photocatalytic hybrid nanocomposites of metal oxide nanoparticles enhanced towards the visible spectral range. *Applied Catalysis B: Environmental* 105(1–2), 77-85.

Qiu, X. and Burda, C. (2007) Chemically synthesized nitrogen-doped metal oxide nanoparticles. *Chemical Physics* 339(1), 1-10.

Ranade, M.R., Navrotsky, A., Zhang, H.Z., Banfield, J.F., Elder, S.H., Zaban, A., Borse, P.H., Kulkarni, S.K., Doran, G.S. and Whitfield, H.J. (2002) Energetics of nanocrystalline TiO<sub>2</sub>. *Proceedings of the National Academy of Sciences* 99(2), 6476-6481.

Rothenberger, G., Moser, J., Graetzel, M., Serpone, N. and Sharma, D.K. (1985) Charge carrier trapping and recombination dynamics in small semiconductor particles. *Journal of the American Chemical Society* 107(26), 8054-8059.

Sakai, E., Amemiya, K., Chikamatsu, A., Hirose, Y., Shimada, T. and Hasegawa, T. (2013) X-ray absorption and magnetic circular dichroism characterization of Fe-doped thin films. *Journal of Magnetism and Magnetic Materials* 333(0), 130-133.

Sakthivel, S., Neppolian, B., Shankar, M.V., Arabindoo, B., Palanichamy, M. and

Murugesan, V. (2003) Solar photocatalytic degradation of azo dye: comparison of photocatalytic efficiency of ZnO and TiO<sub>2</sub>. *Solar Energy Materials and Solar Cells* 77(1), 65-82.

Sathish, M., Viswanathan, B., Viswanath, R.P. and Gopinath, C.S. (2005) Synthesis, Characterization, Electronic Structure, and Photocatalytic Activity of Nitrogen-Doped TiO<sub>2</sub> Nanocatalyst. *Chemistry of Materials* 17(25), 6349-6353.

Scuderi, V., Scalese, S., Bagiante, S., Compagnini, G., Durso, L. and Privitera, V. (2009) Direct observation of the formation of linear C chain/carbon nanotube hybrid systems. *Carbon* 47(8), 2134-2137.

Seery, M.K., George, R., Floris, P. and Pillai, S.C. (2007) Silver doped titanium dioxide nanomaterials for enhanced visible light photocatalysis. *Journal of Photochemistry and Photobiology A: Chemistry* 189(2), 258-263.

Shi, J.-w., Zheng, J.-t. and Wu, P. (2009) Preparation, characterization and photocatalytic activities of holmium-doped titanium dioxide nanoparticles. *Journal of Hazardous Materials* 161(1), 416-422.

Singh, D., Yadav, P., Singh, N., Kant, C., Kumar, M., Sharma, S.D. and Saini, K.K. (2011) Dielectric properties of Fe-doped TiO<sub>2</sub> nanoparticles synthesised by sol-gel route. *Journal of Experimental Nanoscience* 8(2), 171-183.

Smith, W. and Zhao, Y. (2008) Enhanced Photocatalytic Activity by Aligned WO<sub>3</sub>/TiO<sub>2</sub> Two-Layer Nanorod Arrays. *The Journal of Physical Chemistry C* 112(49), 19635-19641.

Sobana, N. and Swaminathan, M. (2007) Combination effect of ZnO and activated

carbon for solar assisted photocatalytic degradation of Direct Blue 53. *Solar Energy Materials and Solar Cells* 91(8), 727-734.

Sobana, N., Muruganadham, M. and Swaminathan, M. (2006) Nano-Ag particles doped TiO<sub>2</sub> for efficient photodegradation of Direct azo dyes. *Journal of Molecular Catalysis A: Chemical* 258(1), 124-132.

Song, K.Y., Park, M.K., Kwon, Y.T., Lee, H.W., Chung, W.J. and Lee, W.I. (2001) Preparation of Transparent Particulate MoO<sub>3</sub>/TiO<sub>2</sub> and WO<sub>3</sub>/TiO<sub>2</sub> Films and Their Photocatalytic Properties. *Chemistry of Materials* 13(7), 2349-2355.

Spurr, R.A. and Myers, H. (1957) Quantitative Analysis of Anatase-Rutile Mixtures with an X-Ray Diffractometer. *Analytical Chemistry* 29(5), 760-762.

Štengl, V., Bakardjieva, S. and Murafa, N. (2009) Preparation and photocatalytic activity of rare earth doped TiO<sub>2</sub> nanoparticles. *Materials Chemistry and Physics* 114(1), 217-226.

Sui, R., Young, J.L. and Berlinguette, C.P. (2010) Sol-gel synthesis of linear Sn-doped TiO<sub>2</sub> nanostructures. *Journal of Materials Chemistry* 20(3), 498-503.

Sun, Y., Mayers, B. and Xia, Y. (2003) Metal Nanostructures with Hollow Interiors. *Advanced Materials* 15(7-8), 641-646.

Suzuki, M., Ito, T. and Taga, Y. (2001) Photocatalysis of sculptured thin films of TiO<sub>2</sub>. *Applied Physics Letters* 78(25), 3968-3970.

Tada, H., Kokubu, A., Iwasaki, M. and Ito, S. (2004) Deactivation of the TiO<sub>2</sub> Photocatalyst by Coupling with WO<sub>3</sub> and the Electrochemically Assisted High

Photocatalytic Activity of  $\text{WO}_3$ . *Langmuir* 20(11), 4665-4670.

Teh, C.M. and Mohamed, A.R. (2011) Roles of titanium dioxide and ion-doped titanium dioxide on photocatalytic degradation of organic pollutants (phenolic compounds and dyes) in aqueous solutions: A review. *Journal of Alloys and Compounds* 509(5), 1648-1660.

Tojo, S., Tachikawa, T., Fujitsuka, M. and Majima, T. (2008) Iodine-Doped  $\text{TiO}_2$  Photocatalysts: Correlation between Band Structure and Mechanism. *The Journal of Physical Chemistry C* 112(38), 14948-14954.

Tristao, J.C., Magalhaes, F., Corio, P. and Sansiviero, M.T.C. (2006) Electronic characterization and photocatalytic properties of  $\text{CdS}/\text{TiO}_2$  semiconductor composite. *Journal of Photochemistry and Photobiology A: Chemistry* 181(2), 152-157.

Tsao, H.N., Burschka, J., Yi, C., Kessler, F., Nazeeruddin, M.K. and Gratzel, M. (2011) Influence of the interfacial charge-transfer resistance at the counter electrode in dye-sensitized solar cells employing cobalt redox shuttles. *Energy & Environmental Science* 4(12), 4921-4924.

Tsukamoto, D., Shiraishi, Y., Sugano, Y., Ichikawa, S., Tanaka, S. and Hirai, T. (2012) Gold Nanoparticles Located at the Interface of Anatase/Rutile  $\text{TiO}_2$  Particles as Active Plasmonic Photocatalysts for Aerobic Oxidation. *Journal of the American Chemical Society* 134(14), 6309-6315.

Tu, Y.-F., Huang, S.-Y., Sang, J.-P. and Zou, X.-W. (2009) Synthesis and photocatalytic properties of Sn-doped  $\text{TiO}_2$  nanotube arrays. *Journal of Alloys and Compounds* 482(1), 382-387.

Umebayashi, T., Yamaki, T., Itoh, H. and Asai, K. (2002) Band gap narrowing of titanium dioxide by sulfur doping. *Applied Physics Letters* 81(3), 454-456.

Vu, D., Li, X., Li, Z. and Wang, C. (2012) Phase-Structure Effects of Electrospun TiO<sub>2</sub> Nanofiber Membranes on As(III) Adsorption. *Journal of Chemical & Engineering Data* 58(1), 71-77.

Wan, Q., Wang, T.H. and Zhao, J.C. (2005) Enhanced photocatalytic activity of ZnO nanotetrapods. *Applied Physics Letters* 87(8), 083105-083103.

Wang, C.-y., Bottcher, C., Bahnemann, D.W. and Dohrmann, J.K. (2003a) A comparative study of nanometer sized Fe(III)-doped TiO<sub>2</sub> photocatalysts: synthesis, characterization and activity. *Journal of Materials Chemistry* 13(9), 2322-2329.

Wang, F., Chen, X., Hu, X., Wong, K.S. and Yu, J.C. (2012) WO<sub>3</sub>/TiO<sub>2</sub> microstructures for enhanced photocatalytic oxidation. *Separation and Purification Technology* 91(0), 67-72.

Wang, H., Wu, Z., Liu, Y. and Sheng, Z. (2008) The characterization of ZnO-anatase-rutile three-component semiconductor and enhanced photocatalytic activity of nitrogen oxides. *Journal of Molecular Catalysis A: Chemical* 287(1), 176-181.

Wang, X., Zhao, J., Kang, Y., Li, L. and Xu, X. (2014) Photoelectrochemical properties of Fe-doped TiO<sub>2</sub> nanotube arrays fabricated by anodization. *Journal of Applied Electrochemistry* 44(1), 1-4.

Wang, Y., Cheng, H., Hao, Y., Ma, J., Li, W. and Cai, S. (1999) Preparation, characterization and photoelectrochemical behaviors of Fe(III)-doped TiO<sub>2</sub>

nanoparticles. *Journal of Materials Science* 34(15), 3721-3729.

Wang, Y., Hang, K., Anderson, N.A. and Lian, T. (2003c) Comparison of Electron Transfer Dynamics in Molecule-to-Nanoparticle and Intramolecular Charge Transfer Complexes. *The Journal of Physical Chemistry B* 107(35), 9434-9440.

Wang, Z., Wang, W., Tang, J., Tung, L.D., Spinu, L. and Zhou, W. (2003b) Extraordinary Hall effect and ferromagnetism in Fe-doped reduced rutile. *Applied Physics Letters* 83(3), 518-520.

Wang, Z.-S., Huang, C.-H., Huang, Y.-Y., Hou, Y.-J., Xie, P.-H., Zhang, B.-W. and Cheng, H.-M. (2001) A Highly Efficient Solar Cell Made from a Dye-Modified ZnO-Covered TiO<sub>2</sub> Nanoporous Electrode. *Chemistry of Materials* 13(2), 678-682.

Watt, J.F. (2003) *An introduction to surface analysis by XPS and AES*, Wiley.

Weiss, B.M., Artioli, N. and Iglesia, E. (2012) Catalytic NO Oxidation Pathways and Redox Cycles on Dispersed Oxides of Rhodium and Cobalt. *ChemCatChem* 4(9), 1397-1404.

Woan, K., Pyrgiotakis, G. and Sigmund, W. (2009) Photocatalytic Carbon-Nanotube-TiO<sub>2</sub> Composites. *Advanced Materials* 21(21), 2233-2239.

Wong, M.-S., Hsu, S.-W., Rao, K.K. and Kumar, C.P. (2008) Influence of crystallinity and carbon content on visible light photocatalysis of carbon doped titania thin films. *Journal of Molecular Catalysis A: Chemical* 279(1), 20-26.

Wu, C.-H. (2004) Comparison of azo dye degradation efficiency using UV/single semiconductor and UV/coupled semiconductor systems. *Chemosphere* 57(7),

601-608.

Wu, C.-M., Baltrusaitis, J., Gillan, E.G. and Grassian, V.H. (2011) Sulfur Dioxide Adsorption on ZnO Nanoparticles and Nanorods. *The Journal of Physical Chemistry C* 115(20), 10164-10172.

Wu, T., Liu, G., Zhao, J., Hidaka, H. and Serpone, N. (1998) Photoassisted Degradation of Dye Pollutants. V. Self-Photosensitized Oxidative Transformation of Rhodamine B under Visible Light Irradiation in Aqueous TiO<sub>2</sub> Dispersions. *The Journal of Physical Chemistry B* 102(30), 5845-5851.

Xiang, Q., Yu, J. and Jaroniec, M. (2012) Synergetic Effect of MoS<sub>2</sub> and Graphene as Cocatalysts for Enhanced Photocatalytic H<sub>2</sub> Production Activity of TiO<sub>2</sub> Nanoparticles. *Journal of the American Chemical Society* 134(15), 6575-6578.

Xie, Y. and Zhao, X. (2008) The effects of synthesis temperature on the structure and visible-light-induced catalytic activity of F-N-codoped and S-N-codoped titania. *Journal of Molecular Catalysis A: Chemical* 285(1), 142-149.

Xu, D., Feng, L. and Lei, A. (2009) Characterizations of lanthanum trivalent ions/TiO<sub>2</sub> nanopowders catalysis prepared by plasma spray. *Journal of Colloid and Interface Science* 329(2), 395-403.

Xu, Y. and Schoonen, M.A. (2000) The absolute energy positions of conduction and valence bands of selected semiconducting minerals. *American Mineralogist* 85(3-4), 543-556.

Yang, K., Dai, Y., Huang, B. and Whangbo, M.-H. (2009) Density Functional Characterization of the Visible-Light Absorption in Substitutional C-Anion- and

C-Cation-Doped TiO<sub>2</sub>. The Journal of Physical Chemistry C 113(6), 2624-2629.

Yang, L. and Leung, W.W.-F. (2011) Application of a Bilayer TiO<sub>2</sub> Nanofiber Photoanode for Optimization of Dye-Sensitized Solar Cells. Advanced Materials 23(39), 4559-4562.

Yashima, M., Ishimura, D. and Ohoyama, K. (2005) Temperature Dependence of Lattice Parameters and Anisotropic Thermal Expansion of Bismuth Oxide. Journal of the American Ceramic Society 88(8), 2332-2335.

Yin, H., Wada, Y., Kitamura, T., Sakata, T., Mori, H. and Yanagida, S. (2001) Enhanced Photocatalytic Dechlorination of 1,2,3,4-Tetrachlorobenzene Using Nanosized CdS/TiO<sub>2</sub> Hybrid Photocatalyst under Visible Light Irradiation. Chemistry Letters 30(4), 334-335.

Yoon, J.-W., Sasaki, T. and Koshizaki, N. (2005) Dispersion of nanosized noble metals in TiO<sub>2</sub> matrix and their photoelectrode properties. Thin Solid Films 483(1 鈥?), 276-282.

Yu, J., Xiang, Q. and Zhou, M. (2009) Preparation, characterization and visible-light-driven photocatalytic activity of Fe-doped titania nanorods and first-principles study for electronic structures. Applied Catalysis B: Environmental 90(3), 595-602.

Yu, J.C., Yu, Ho, Jiang and Zhang (2002) Effects of F- Doping on the Photocatalytic Activity and Microstructures of Nanocrystalline TiO<sub>2</sub> Powders. Chemistry of Materials 14(9), 3808-3816.

Yu, J.-G., Yu, H.-G., Cheng, B., Zhao, X.-J., Yu, J.C. and Ho, W.-K. (2003) The Effect of Calcination Temperature on the Surface Microstructure and Photocatalytic Activity of TiO<sub>2</sub> Thin Films Prepared by Liquid Phase Deposition. *The Journal of Physical Chemistry B* 107(50), 13871-13879.

Zhang, H., Chen, G. and Bahnemann, D.W. (2009) Photoelectrocatalytic materials for environmental applications. *Journal of Materials Chemistry* 19(29), 5089-5121.

Zhang, Y., Tang, Z.-R., Fu, X. and Xu, Y.-J. (2010) TiO<sub>2</sub>-Graphene Nanocomposites for Gas-Phase Photocatalytic Degradation of Volatile Aromatic Pollutant: Is TiO<sub>2</sub>-Graphene Truly Different from Other TiO<sub>2</sub>-Carbon Composite Materials? *ACS Nano* 4(12), 7303-7314.

Zhao, X., Ando, Y., Liu, Y., Jinno, M. and Suzuki, T. (2003) Carbon Nanowire Made of a Long Linear Carbon Chain Inserted Inside a Multiwalled Carbon Nanotube. *Physical Review Letters* 90(18), 187401.

Zhao, Y., Li, C., Liu, X. and Gu, F. (2007) Highly enhanced degradation of dye with well-dispersed TiO<sub>2</sub> nanoparticles under visible irradiation. *Journal of Alloys and Compounds* 440(1), 281-286.

Zhao, Y., Li, C., Liu, X., Gu, F., Du, H.L. and Shi, L. (2008) Zn-doped TiO<sub>2</sub> nanoparticles with high photocatalytic activity synthesized by hydrogen-oxygen diffusion flame. *Applied Catalysis B: Environmental* 79(3), 208-215.

Zhao, Z., Tian, J., Wang, D., Kang, X., Sang, Y., Liu, H., Wang, J., Chen, S., Boughton, R.I. and Jiang, H. (2012) UV-visible-light-activated photocatalysts based on Bi<sub>2</sub>O<sub>3</sub>/Bi<sub>4</sub>Ti<sub>3</sub>O<sub>12</sub>/TiO<sub>2</sub> double-heterostructured TiO<sub>2</sub> nanobelts. *Journal of*

Materials Chemistry 22(44), 23395-23403.

Zhu, J., Yang, D., Geng, J., Chen, D. and Jiang, Z. (2008) Synthesis and characterization of bamboo-like CdS/TiO<sub>2</sub> nanotubes composites with enhanced visible-light photocatalytic activity. Journal of Nanoparticle Research 10(5), 729-736.

Zhu, Y.-F., Xu, L., Zhang, J., Qi, H.-Q., Du, R.-G., Shao, Y.-Z. and Lin, C.-J. (2013) Fe-Doped TiO<sub>2</sub> Nanotube Array Films for Photocathodic Protection of Stainless Steel. ECS Transactions 53(33), 31-39.